ONBOARD SENSING, FLIGHT CONTROL, AND NAVIGATION OF A DUAL-MOTOR HUMMINGBIRD-SCALE FLAPPING WING ROBOT

A Dissertation

Submitted to the Faculty

of

Purdue University

by

Zhan Tu

In Partial Fulfillment of the

Requirements for the Degree

of

Doctor of Philosophy

December 2019

Purdue University

West Lafayette, Indiana

THE PURDUE UNIVERSITY GRADUATE SCHOOL
STATEMENT OF DISSERTATION APPROVAL

Dr. Xinyan Deng, Chair
School of Mechanical Engineering
Dr. David J. Cappelleri
School of Mechanical Engineering
Dr. Gregory M. Shaver
School of Mechanical Engineering
Dr. Jianghai Hu
School of Electrical and Computer Engineering

Approved by:

Dr. Jay P. Gore
Head of the School Graduate Program

To my beloved family.

ACKNOWLEDGMENTS

First and foremost, I would like to express my thankfulness to my advisor, Dr.Xinyan Deng, for giving me the encouragement, support, and guidance to study on this fascinating research field of the bio-inspired flapping-wing micro aerial robots. It has been a privilege to work with Dr.Deng and be her student.

It is my sincere honor to have Dr.Gregory M. Shaver, Dr.David Cappelleri, and Dr.Jianghai Hu being my academic advisory committee members.

Special thanks to my fellow lab mate, Fan Fei and Jian Zhang, for their fruitful brainstorm and collaborations on this work. I would also like to thank Jesse Roll, Yun Liu, Yilun Yang, Matthew Eagon, Jianwen Li, Charlie Chu, and Limeng Liu, at Purdue Bio-Robotics Lab, for their help and support along the way.

To my parents, my wife, and my son, thank you for your always unconditional support and love. Without you, it is impossible to finish this dissertation.

TABLE OF CONTENTS

Page

LIST OF TABLES . . . vii

LIST OF FIGURES . . . viii

ABSTRACT . . . xii

1. INTRODUCTION . . . 1
   - 1.1 Motivation . . . 1
   - 1.2 Related Work and Research Challenges . . . 2
     - 1.2.1 Actuation . . . 3
     - 1.2.2 Onboard Attitude Sensing . . . 7
     - 1.2.3 Onboard Control . . . 9
     - 1.2.4 Navigating Confined Spaces . . . 12
   - 1.3 Thesis Contribution and Organization . . . 13
2. ROBOT DESCRIPTION AND MODELING . . . 15
   - 2.1 System Overview . . . 15
   - 2.2 Wing-actuation System Dynamics . . . 18
     - 2.2.1 Dynamics of Wing Rotation . . . 18
     - 2.2.2 Dynamics of Wing-actuation System . . . 20
     - 2.2.3 System Efficiency . . . 22
   - 2.3 Wing Kinematics Modulation . . . 22
   - 2.4 Body Dynamics . . . 27
3. ONBOARD ATTITUDE SENSING . . . 30
   - 3.1 Introduction . . . 31
   - 3.2 Sensor Fusion Design . . . 31
     - 3.2.1 Modeling of Sensor Readings . . . 32
     - 3.2.2 External Acceleration Compensation . . . 33
     - 3.2.3 Magnetometer Calibration . . . 35
     - 3.2.4 Adaptive Orientation Update . . . 37
   - 3.3 Experimental Result and Discussion . . . 40
   - 3.4 Conclusion . . . 45
4. ONBOARD FLIGHT CONTROL . . . 47
   - 4.1 Introduction . . . 48
   - 4.2 Model-based Control . . . 50
     - 4.2.1 System Trimming . . . 50
     - 4.2.2 Control Law Design . . . 52

Page
4.3 RL-enabled Acrobatic Maneuvering . . . 55
4.3.1 Problem Formulation . . . 55
4.3.2 Reward Design . . . 56
4.3.3 Training . . . 59
4.4 Experimental Result and Discussion . . . 60
4.4.1 Stable Flight: Hovering and Waypoint Tracking . . . 60
4.4.2 Extreme Maneuver: Drift-free Flip . . . 61
4.5 Conclusion . . . 64
5. NAVIGATING CONFINED SPACE USING FLAPPING WINGS . . . 65
5.1 Introduction . . . 65
5.2 Environment Sensing Principle . . . 67
5.2.1 Terrain Sensing . . . 67
5.2.2 Wall Sensing . . . 69
5.3 Motion Plan . . . 72
5.4 Experimental Result and Discussion . . . 74
5.4.1 Terrain Following . . . 74
5.4.2 Wall Following . . . 75
5.4.3 Passing Narrow Corridor . . . 76
5.5 Conclusions . . . 78
6. UNTETHERED FLIGHT . . . 80
6.1 Introduction . . . 81
6.2 System Design . . . 83
6.3 Onboard System Integration . . . 85
6.3.1 Actuation . . . 86
6.3.2 Sensing and Control . . . 91
6.3.3 Power Regulation . . . 91
6.3.4 Circuit Layout . . . 93
6.4 Experimental Result and Discussion . . . 94
6.5 Conclusion . . . 96
7. CONCLUSION AND FUTURE WORK . . . 97
REFERENCES . . . 100

LIST OF TABLES

Table Page

3.1 RMSE Comparison of Tested Sensor Fusion Algorithms 43

6.1 Parameters of The Proposed Wing-actuation System 86

LIST OF FIGURES

Figure Page

1.1 Flapping wing platforms that demonstrated sustained hover flight: (a). AeroVironment Nanohummingbird [26]: weighs 19 grams and has a wingspan of 165mm; (b). Harvard Robobee [42], weighs 0.8 grams and has a wingspan of 30mm; (c). Texas A&M robotic hummingbird [30], weighs 62 grams and has a wingspan of 300mm; (d). ULB COLIBRI [31], weighs 22 grams and has a wingspan of 210mm; (e). KUBeetle [32], weighs 21 grams and has a wingspan of 200mm; (f). Delfly Nimble [35] weighs 28 grams and has a wingspan of 330mm, (g). Purdue Hummingbird, the proposed platform in this thesis: has a wingspan of 170mm and weighs 12 grams with power tethers. The untethered version of Purdue Hummingbird weights 20 grams with the same wingspan. 4

1.2 Power density versus mass of various actuators from [46]. 5

2.1 Design of the proposed hummingbird robot. 16

2.2 Schematic diagram of the onboard electronic system of the proposed hummingbird robot. 16

2.3 Prototyped hummingbird robot. The system is powered through thin tether wires. 17

2.4 Wing parameters of the proposed hummingbird robot. 18

2.5 (a). Experimental setup for wing kinematics validation and instantaneous lift/torque measurement. (b). Head camera view in wing motion validation. (c). Validation results of wing rotation and stroke angle in three typical wing beats. 24

2.6 (a), (b), (c), (d) illustrate the wing modulations for the thrust and roll, pitch, and yaw torque generation, respectively. Experimental validations of the modeled thrust and torque generation are shown accordingly. Gray-cross indicates the nominal operating point. 25

2.7 Coordinate definition of the vehicle body frame and the inertial frame. . . 28

3.1 Reciprocating wing motion causes severe body vibration. 30

3.2 Pitch-axis acceleration SNR in the static and oscillated condition. The noise is orders of magnitudes higher with the wing motion effect. a_{ex} compensation increases the SNR effectively on flapping wing platform. . . 35

Figure Page

3.3 Magnetometer calibration. Motor introduced offset is compensated. 36

3.4 Block diagram of the proposed sensor fusion for FWMAV attitude estimation.38

3.5 Illustration of flight test setup in VICON space. 41

3.6 (a). Attitude estimation in hovering (constraint condition). (b). Attitude estimation in maneuvering (constraint condition). (c). Euler angle estimation in maneuvering with aerodynamic force compensated acceleration for Madgwick filter and EKF. The accuracy of both was improved. Nevertheless, they still failed to converge to the ground truth before wings stopped (around 14s). 42

3.7 Pitch angle estimation in maneuvering condition with/without a_{ex} compensation for the proposed method. Without aerodynamic force compensation, pitch angle cannot be estimated correctly. 43

3.8 Two free flight test, the proposed sensor fusion working together with flight control. (a). Attitude estimation in hovering. (b). Attitude estimation in maneuvering. Both scenarios show great estimation accuracy. 44

4.1 Two examples of open-loop liftoff. (a). Liftoff with only a constant thrust command. (b). Liftoff with balanced trim condition. 50

4.2 Motor current feedback for the estimation of system trim condition. 51

4.3 Illustration of the hybrid controller structure. If the flip maneuver was triggered, RL policy takeover the original controller. 55

4.4 (a). Coordinate define and translation. (b). A successful flip over along Y-axis. (c). A failed flip over along Y-axis. 57

4.5 Illustration of reward model design. 58

4.6 (a). Time sequential result of a typical takeoff, hovering, and landing flight. Composed image only show takeoff and hovering. (b). Attitude and position of the robot in the test. Gray dash lines represent control references. 61

4.7 (a1). and (b1). Composed images showing FWMAV point to point tracking fly along longitudinal and lateral direction of the vehicle, respectively. Arrows point out the corresponding flight directions. (a2). and (b2). Attitude and X-Y position of the robot in the test. Gray dash lines represent control references for maneuvering along longitudinal and lateral direction respectively. 62

Figure Page

4.8 (a). A sample of flip maneuver sequence in simulation. Flight trajectories of the hummingbird robot in simulated flip maneuver is shown. Trajectories are averaged over 5 trials. (b). A sample of flip maneuver sequence in experiment. Flight trajectories of the hummingbird robot in experimental flip maneuver is shown. Trajectories are averaged over 5 trials. 63

5.1 A dual-motor powered hummingbird robot is navigating a 1ft width corridor relying on load variations on its wings. Wing load change can be captured by onboard motor current feedback. 66

5.2 Setup for ground effect quantification. 67

5.3 (a). Averaged lift measurement with increased ground clearance. (b). The corresponding motor current change with increased ground clearance. $D/\bar{c}$ is the ratio of ground clearance and mean chord length of the wing. $\bar{i_L}$ and $\bar{i_R}$ are cycle-averaged current feedback of the left and right wing respectively. 69

5.4 (a). When both wings hit the front-side obstacle during the forward flight (left figure), the corresponding plot of instantaneous motor current showing both wings' upstroke currents is higher than normal (right figure). (b). When the left wing's downstroke is blocking on the side by the wall barrier (left figure), only the corresponding left wings' downstroke current becomes greater than normal (right figure). (c1)-(c3). Illustration of the setup for quantifying the wing collision effect, including bumping from front/back-side as (c1) and upstroke/downstroke-side as (c2) and (c3). . . 71

5.5 Calibrated upper bound of the motor current feedback according to different collision scenarios. 72

5.6 (a). Time sequential result of a typical terrain sensing and mapping test. (b). The cycle-averaged current feedback data corresponds to (a). (c). Altitude mapping result through ground effect. 75

5.7 (a). Time sequential result of a typical wall sensing and mapping test. (b). The instantaneous current feedback data corresponds to (a). (c). Actual flight path with collisions and path alternations. 76

5.8 (a). Time sequential result of a typical corridor navigating. (b). Actual flight path with collisions and path alternations. (c). Altitude mapping result through ground effect. 77

5.9 With more flights, the contours of the corridor can be sketched clearly. . . 78

6.1 Untethered sustained outdoor hover flight of a hummingbird-scale flapping wing robot. Background is blurred to reduce distractions. 80

Figure Page

6.2 Pareto Front of the robot design. $\boldsymbol{x}^*$ is the selected design. 84

6.3 Illustration of system integration of the proposed robot. 85

6.4 Schematic diagram and prototyped circuits of the complete onboard electronic system that enables untethered flight of the proposed hummingbird robot. 87

6.5 (a). A typical record of the instantaneous current and voltage in normal hover flight condition. (b).The differential amplitude of the left and right wings are generated by flight control for the attitude stabilization. Digitized wing kinematics can be used for runtime power estimation. . . . 88

6.6 Performance comparison of bootstrap capacitance with different dielectrics. (a). Motor and driver working in normal condition. (b). Motor and driver working in overheated condition. 89

6.7 Torque ripple suppression via motor current control. 90

6.8 Illustration of the step-up regulator performance. Regulation efficiency varies depending on battery status. 92

6.9 Illustration of the layered design of onboard system. 93

6.10 (a) flight test without power and communication tether in VICON space for attitude and position recording, demonstrating the performance of onboard sensor fusion and control. (b) control result corresponds to (a). . . . 94

6.11 Compound result of a typical outdoor untethered stable hovering under 15mph averaged wind gust. 95

ABSTRACT

Tu, Zhan. Ph.D., Purdue University, December 2019. Onboard Sensing, Flight Control, and Navigation of A Dual-motor Hummingbird-scale Flapping Wing Robot. Major Professor: Xinyan, Deng, School of Mechanical Engineering.

Insects and hummingbirds not only can perform long-term stationary hovering but also are capable of acrobatic maneuvers. At their body scale, such extraordinary flight performance remains unmatched by state-of-the-art conventional man-made aerial vehicles with fixed or rotary wings. Insects' and hummingbirds' near maximal performance come from their highly intricate and powerful wing-thorax actuation systems, sophisticated sensory system, and precise neuromotor control. Flapping Wing Micro Air Vehicles (FWMAVs) with bio-inspired flapping flight mechanisms hold great promise in matching the performance gap of their natural counterparts. Developing such autonomous flapping-wing vehicles to achieve animal-like flight, however, is challenging. The difficulties are mainly from the high power density requirements under the stringent constraints of scale, weight, and power, severe system oscillations induced by high-frequency wing motion, high nonlinearity of the system, and lack of miniature navigation sensors, which impede actuation system design, onboard sensing, flight control, and autonomous navigation.

To address these open issues, in this thesis, we first introduce systematic modeling of a dual-motor hummingbird-scale flapping wing robot. Based upon it, we then present studies of the onboard sensor fusion, flight control, and navigation method.

By taking the key inspiration from its natural counterparts, the proposed hummingbird robot has a pair of independently controlled wings. Each wing is directly actuated by a dc motor. Motors undergo reciprocating motion. Such a design is a severely underactuated system, namely, it relies on only two actuators (one per wing) to control full six degrees of freedom body motion. As a bio-inspired design, it also

requires the vehicle close to its natural counterparts' size and weight meanwhile provide sufficient lift and control effort for autonomy. Due to stringent payload limitation from severe underactuation and power efficiency challenges caused by motor reciprocating motion, the design and integration of such a system is a challenging task. In this thesis, we present the detailed modeling, optimization, and system integration of onboard power, actuation, sensing, and flight control to address these unique challenges. As a result, we successfully prototyped such dual-motor powered hummingbird robot, either with power tethers or fully untethered. The tethered platform is used for designing onboard sensing, control, and navigation algorithms. Untethered design tackles system optimization and integration challenges. Both tethered/untethered versions demonstrate sustained stable flight.

For onboard attitude sensing, a real-time sensor fusion algorithm is proposed with model-based adaptive compensation for both sensor reading drift and wing motion induced severe system vibration. With accurate and robust sensing results, a nonlinear robust control law is designed to stabilize the system during flight. Stable hovering and waypoint tracking flight were experimentally conducted to demonstrate the control performance. In order to achieve natural flyers' acrobatic maneuverability, we propose a hybrid control scheme by combining a model-based robust controller with a model-free reinforcement learning maneuver policy to perform aggressive maneuvers. The model-based control is responsible for stabilizing the robot in nominal flight scenarios. The reinforcement learning policy pushes the flight envelope to pilot fierce maneuvers. To demonstrate the effectiveness of the proposed control method, we experimentally show animal-like tight flip maneuver on the proposed hummingbird robot, which is actuated by only two DC motors. These successful results show the promise of such a hybrid control design on severely underactuated systems to achieve high-performance flight.

In order to navigate confined space while matching the design constraints of such a small robot, we propose to use its wings in dual functions - combining sensing and actuation in one element, which is inspired by animals' multifunctional flapping wings.

Based on the interpretation of the motor current feedback which directly indicates wing load changes, the onboard somatosensory-like feedback has been achieved on our hummingbird robot. For navigation purposes, such a method can sense the presence of environmental changes, including grounds, walls, stairs, and obstacles, without the need for any other sensory cues. As long as the robot can fly, it can sense surroundings. To demonstrate this capability, three challenging tasks have been conducted onto the proposed hummingbird robot: terrain following, wall detection and bypass, and navigating a confined corridor.

Finally, we integrate the proposed methods into the untethered platform, which enables stable untethered flight of such a design in both indoor and outdoor tests. To the best of our knowledge, this result presents the first bio-inspired FWMAV powered by only two actuators and capable of performing sustained stable flight in both indoor and outdoor environment. It is also the first untethered flight of an at-scale tailless hummingbird robot with independently controlled wings, a key inspiration from its natural counterparts.

1. INTRODUCTION

1.1 Motivation

Through millions of years of adaptation, insects and hummingbirds have evolved with extraordinary flight capabilities. Powered by flapping wings, they can hover, make sharp turns, fly backward and sideways, land upside-down, fly dexterously in courtship, perform rapid evasive maneuvers when facing threats, and achieve nearly drift-free body flips while navigating confined, cluttered spaces [1–5]. To date, much of their extraordinary flight performances remain unchallenged by small scale man-made flying vehicles. In fact, downsizing to insect or hummingbird sizes, flight performance of the most pervasive aircraft, i.e., fixed and rotary winged vehicle, drops significantly, if not impossible. Small-sized wings and low Reynolds numbers (the ratio of inertial forces to viscous forces within a fluid) yield inadequate aerodynamic performance of those conventional aerodynamic surface designs. In contrast, by taking advantages of the unique unsteady aerodynamic mechanism of flapping flight, including clap-and-fling, rotational circulation, wake-capture, delayed stall (leading edge vortex), and added-mass effects, insects and hummingbirds are capable of generating sufficient lift and control efforts under very tight size and weight constraints [6–11]. Fascinated by their superior flying skills and compact sizes, researchers and roboticists attempted to imitate their aerodynamic performance and develop Flapping Wing Micro Aerial Vehicles (FWMAVs), which is promising for acrobatic fly of man-made MAVs in tight spaces. Moreover, since the flapping wing vehicles work favorably in compact sizes, they are expected to demonstrate excellent environmental adaptability in the cluttered spaces.

In flying animals, the highly intricate and powerful wing-thorax actuation system, the sophisticated sensory system, and the precise neuromotor control are all critical to their extraordinary flight abilities, from basic reactive control to autonomous navigation [2, 3, 12–14]. Over the past decades, extensive studies have been conducted on these sophisticated mechanisms. Besides the ever-increasing understanding of the aerodynamic mechanism and unique lift generation principles of flapping flight [6–10, 15, 16], there are many fruitful results in the design, sensing, control, and navigation of the bio-inspired FWMAVs as well. Dating back from the UC Berkeley MFI control [17,18], the development of FWMAVs has witnessed tremendous progress in recent years. Today, several designs have been proposed and prototyped from the inspiration of various nature's flyers, including insect-inspired vehicles [19–25], the hummingbird-inspired vehicles [26–33], as well as some well-designed platforms that are actuated by flapping wings with adopted different forms from those of animals [34, 35]. Developing a powerful, miniaturized, multifunctional onboard system for FWMAVs is still a focus of ongoing research, with the main challenge coming from the stringent design constraints of scale, weight, and power (SWaP) requirements. [26, 29, 36–38]. Flapping flight dynamics is also highly nonlinear with rapidly varying, unsteady aerodynamics. It varies significantly under different flight regimes, most of which remain poorly understood except hovering. The variation in dynamics poses challenges to the onboard sensing and control [26, 30–33, 39–41]. Furthermore, relying on limited onboard sensors and computational resources to achieve animal-like environmental adaptability and navigation remains an open issue on bio-inspired flapping wing platforms.

1.2 Related Work and Research Challenges

Developing onboard sensing, control, and navigation on FWMAVs to achieve autonomous flight remains significantly challenging, and is mainly due to the stringent design constraints, limited computing resources, lack of miniature sensors, unmeasurable system uncertainties, unsteady aerodynamics, and highly nonlinear dynamics of the system. Trade-offs among those issues must be carefully considered. In this section, related and previous works are reviewed in detail, and the remaining open challenges are discussed.

1.2.1 Actuation

For a flapping wing platform, the wing actuation strategy dominates the design and control principle of the overall system. As shown in Figure 1.1, according to the different actuation approaches, these state-of-the-art platforms can be divided into two main groups: those using crank-rocker four-bar (or its equivalent) mechanisms to convert unidirectional motor rotation to the reciprocal flapping motion of the wings [26, 30–32], and those employing direct drive of each wing by piezo or motor in reciprocal motion through high-frequency input power modulation [42–44]. In addition, as a notable hybrid design (Figure 1.1.(f)), such an FWMAV is based on two separate motors and linkages to drive its left and right wing pairs, while using additional actuators and translational mechanisms to generate control torques [35].

For flight control, the first group needs to rely on additional servomechanisms for stroke plane modulation or wing shape deformation, and employ a helicopter-like control instead of decoupled wing controls similar to animals' flight control mechanism. Based on this design principle, AeroVironment's Nanohummingbird [26] achieved the first hover flight of FWMAVs with remote control in 2012. Subsequently, other groups have successfully reproduced similar results following this design principle [30–32]. In such designs, as shown in Figure 1.2, due to their size, weight, and power density needs, they use DC motor as the main actuator to drive the wings. On these platforms, motor rotates continuously at high speed, thus gaining more motor efficiency. Moreover, it significantly simplifies onboard driver integration, i.e., allowing to directly implement off-the-shelf driver modules and designs, such as various brands of Electronic Speed Control (ESC) products. The typical actuation issues, such as power regulation, thermal effects, torque ripples, and motor cogging force, have minor impacts on those platforms. However, due to their coupled wing kinematics

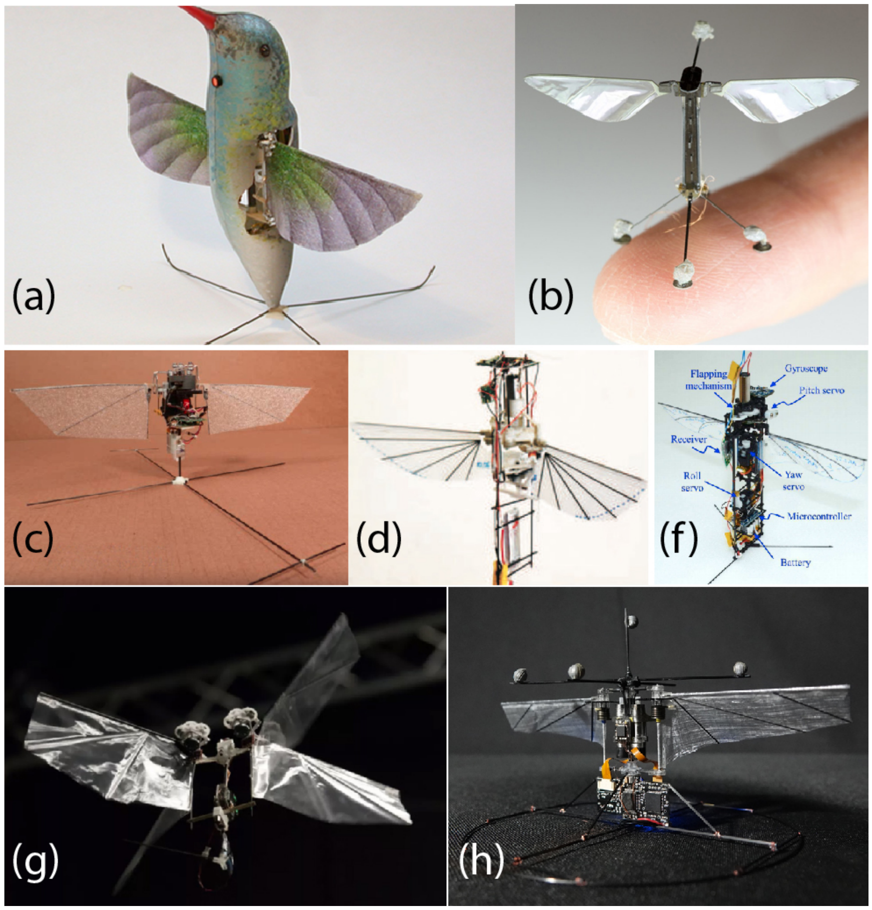

Figure 1.1. : Flapping wing platforms that demonstrated sustained hover flight: (a). AeroVironment Nanohummingbird [26]: weighs 19 grams and has a wingspan of 165mm; (b). Harvard Robobee [42], weighs 0.8 grams and has a wingspan of 30mm; (c). Texas A&M robotic hummingbird [30], weighs 62 grams and has a wingspan of 300mm; (d). ULB COLIBRI [31], weighs 22 grams and has a wingspan of 210mm; (e). KUBeetle [32], weighs 21 grams and has a wingspan of 200mm; (f). Delfly Nimble [35] weighs 28 grams and has a wingspan of 330mm, (g). Purdue Hummingbird, the proposed platform in this thesis: has a wingspan of 170mm and weighs 12 grams with power tethers. The untethered version of Purdue Hummingbird weights 20 grams with the same wingspan.

design, they usually rely on swash-plate like differential mechanisms to generate control torques, which significantly limits the system maneuverability comparing to their natural counterparts [26, 29, 36, 45].

The other FWMAV designs are proposed to drive the wing independently, which takes a key inspiration from flying animals [29, 36, 42]. With independent wing kinematics control, some flapping wing vehicles have demonstrated astonishing maneuvers, such as vertical perching and rapid evasive fly [43, 47]. Without assistance from the linkage mechanism, the actuator needs to undergo high-frequency, bi-directional movement to operate the reciprocating motion of the wings. It simplifies the mechanism design yet results in difficulties for the design of the onboard controller and driver module. The difficulties are mainly from the trade-off between SWaP constraints and high lift-to-weight ratio desires.

For FWMAVs actuated by direct-drive wings, without systematic consideration and layout, the direct adoption of the commercial drivers usually cannot match SWaP criteria properly and results in short of the performance of the lift generation. There-

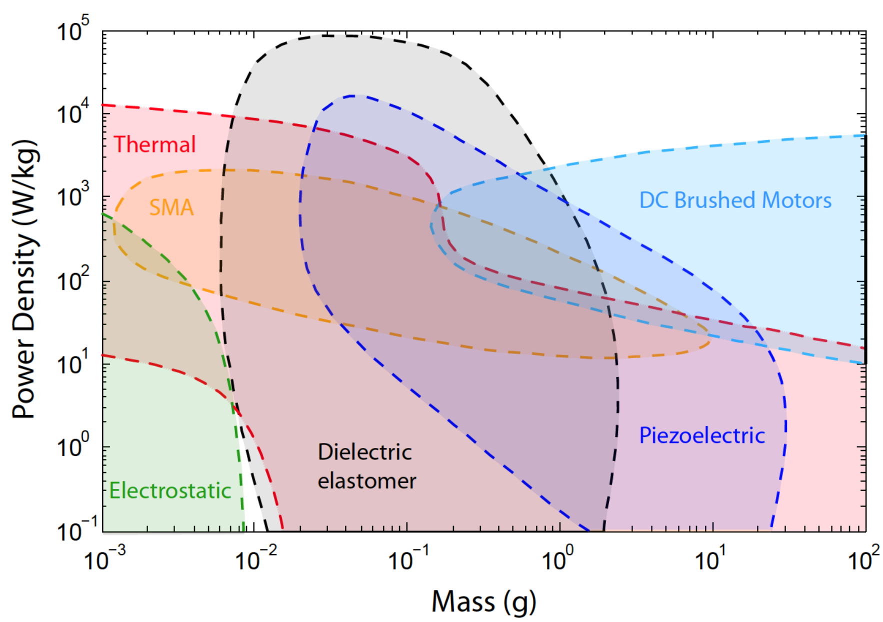

Figure 1.2. : Power density versus mass of various actuators from [46].

fore, in order to boost the system performance, designing a powerful driver module coordinated with an appropriate actuator is essential. For example, on Harvard Robobee - the first insect-scale flapping wing robot that demonstrated stable hovering, a customized 20-milligram onboard driver that can step up a 3.7V Li-poly cell input to 200V was developed to actuate the piezo-driven wings [48]. Despite that the piezoelectric actuator requires high voltage input, its high power density fits their bee-size design perfectly, as demonstrated in Figure 1.2. Specifically, the power density of the design is about 7.75- 9.75kW/kg, which provides about 2.0 lift-to-weight ratio [48]. Based on such powerful actuation system, they demonstrates stable hover flight [42] and an aggressive maneuver [47]. Recently, such insect-scale, piezo-powered FW-MAVs have even demonstrated untethered flight using optical power sources (laser or solar) [37,38]. Nevertheless, for fully autonomous purpose, insect-sized platforms may have their specific limitations on the size and weight of the payload, which extremely challenges such designs to integrate the necessary sensors and controllers onboard. Larger platforms such as hummingbird-sized FWMAVs hold a great promising to accommodate more payload for additional sensors, microcontrollers, and batteries. At such scale, DC motors are the desired actuators for FWMAVs [36,46], which provides sufficient power density for vehicle control while lower the drive voltage.

In this thesis, we propose a wing-actuation design, aiming to boost the actuation performance of a dual-motor actuated hummingbird robot to perform animal-like hovering and agile maneuvering through a pair of independently controlled flapping wings. The particular issue of such a severely underactuated bio-inspired system - tradeoff between payload limitation and power efficiency, has been solved systematically through a multi-object optimization. Following the guidance from the optimization result, the system integration challenge has been addressed as well. In particular, two motors are used to actuate the vehicle, and the wing trajectories are altered by two independent onboard motor drivers, which is controlled by an onboard microcontroller for desired aerodynamic thrust and control torque generation. Body attitude of the proposed platform is sensed by onboard inertial sensors. A dc-dc power regulation module is attached to separate the power of logic and actuation circuits. System can be powered either through power tether or onboard batteries. The proposed tethered design achieves about 2.4 lift-to-weight ratio and the burst power reaches about four times of the rated power consumption in hovering. This result is comparable to the real hummingbirds [5], thus, guarantee the superlative maneuverability and stability in its flapping flight. Untethered stable flight has been experimentally demonstrated in both indoor and outdoor environment as well.

1.2.2 Onboard Attitude Sensing

Reliable onboard attitude feedback and control is essential for autonomous MAVs. In order to accommodate weight and size constraints, the low-cost and lightweight MEMS Inertial Measurement Unit (IMU) is widely used on MAVs as a primary pose sensor, which is usually comprised of an accelerometer, a gyroscope, and a magnetometer.

On flapping wing platforms, IMU sensor presents a unique implementation problem: due to the reciprocating motions of the wings, the resulting instantaneous body acceleration is extremely higher than that of the conventional aircraft. Accordingly, the Signal to Noise Ratio (SNR) of the accelerometer's raw measurements shows orders of magnitudes drop during flapping flight. It almost drives the accelerometer readings to reach its sensing upper bound, causing attitude estimation diverging [33, 49, 50]. Traditional sensor fusion methods for attitude estimation, such as complementary filter, gradient descent methods, and Kalman filter based methods [51–53], are not designed to compensate such severe instantaneous oscillations, thus not able to be directly applied to FWMAVs.

In order to attenuate such severe oscillations, one solution is to add a suppression mechanism between the sensor and the vibration source, i.e., the wing system. Verboom et al. employed this method on Delfly-II [49]. They combine a foam-based mechanical damper with a moving average filter to reject the body vibrations. This approach successfully filtered out the original DC motor vibration up to 300Hz as well as the oscillations from their clap-and-fling wing pair. Compared to their special crossed wing pair design, which mostly generates undesired accelerations along the thrust direction, the reciprocating motion of the wing with bio-inspired structure usually results in more serious consequences. It generates stronger accelerations along the dorsoventral orientation of the vehicle due to the large instantaneous aerodynamic drag in flapping motion and produces obvious Flapping Counter Force (FCF) and Flapping Counter Torque (FCT) - a unique aerodynamic effect on flapping flight platform as presented in [54, 55], both of which affect attitude stability significantly. As observed by Fuller et al., even on the insect scale platform, it can distort the accelerometer readings about two times larger than that of the interest [56]. Therefore, besides passive damping, a well-designed sensor fusion algorithm that capable of compensating such severe vibrations is also necessary for accurate attitude feedback.

On FWMAVs, as the impact of the accelerometer is more prominent than the other internal sensors in IMU, most efforts attempt to avoid using accelerometer in order to reduce the sensing error. In 2012, the AeroVironment Nanohummingbird relied on the integration result of gyroscope readings to achieve the first attitude stable hover flight using flapping wings [26]. Similarly, the Harvard Robobee implemented this strategy within an insect-sized vehicle, which enables up to 5s hovering [56]. Under such severe vibration, a single gyroscope is incapable of guarantee drift-free for long-term sensing due to the sensor bias and ambient noise [57]. In addition, Harvard RoboBee also attempted to use a magnetometer solely for pitch and yaw stabilization [58]. However, magnetometer feedback is easy to be distorted by magnetic or metallic objects, and moreover, it loses roll angle feedback. Alternatively, a promising solution could be using auxiliary sensors with different physical characteristics to aid the inertial sensors, such as cameras or optic flow sensors [59–63]. However, considering SWaP constraints and the usage restrictions of the added sensor, such as the light condition for visual sensors, FWMAVs implementing this alternative solution may still have limited performance [64–66].

In sum, for bio-inspired FWMAVs, in order to achieve a robust, long-term onboard attitude sensing, it is desirable to have a well-designed sensor fusion algorithm that could compensate for aerodynamic forces, sensor measurements noise and drifting. To address this problem, we propose a model-based sensor fusion solution with adaptive compensation for both sensing drift and aerodynamic forces induced by flapping wings.

1.2.3 Onboard Control

To date, numerous efforts have been devoted to interpreting flapping flight control [17, 27, 67–71]. Based on these studies, we have proficient knowledge about flapping flight principles and control methods, such as averaging theory [72, 73]. However, controlled hover flight for a small-sized flapping wing robot remains significantly challenging due to the highly nonlinear system dynamics, complex time-varying aerodynamics, severe body oscillation, limited actuation, manufacturing imperfections, and undesired disturbances. The nonlinearity is mainly caused by the additional damping coming from FCF and FCT, which affects instantaneous aerodynamic force and system dynamics under various flight regimes. In order to deal with system nonlinearity, as our previous work presented [33], a model-based, nonlinear geometric controller with global exponential attractiveness is designed. However, the performance of such design is limited by the run-time varying dynamic model and control command offset. These undesired system uncertainties are due to manufacturing imperfections and unmeasurable components wearing off, which challenges control law design seriously. To reject such trim conditions induced by the mechanical asymmetry of the system, some engineer tricks have been conducted before the flight test, such as repeated manually trim tuning [29,33,40,74]. Since the trim condition also varies with time and operating conditions, the tuning result could become inaccurate after just several flights [29, 74]. Model-based adaptive control allows online parameter adaptation to compensate trim effect in a certain extent [74]. However, during the flight, unmodeled dynamics, such as actuator torque ripples, ground effect, and complex body vibrations, can still drop down the performance of the controller [47]. The robustness of the system needs to be enhanced to withstand these unexpected uncertainties.

Even though stable flight control is already difficult for FWMAVs, in addition to that, performing animal-like extreme maneuvers is an even tougher challenge. Flight dynamics under many maneuvers remain unknown. Different from the model-based control law design, nature's flyers never rely on the strict mathematical calculation to tune the stability of their flight. Insects and hummingbirds mastered their flight control through millions of years adaptation. They can perform 'controlled unstable flight' with consistent performance to demonstrate their extraordinary maneuverability. For example, flies can make nearly drift-free backflips within a minimum footprint. In the man-made control system, doing such maneuvers, the maneuvering control authorities can even contradict to vehicle stabilization goal when the vehicle poses upside down. Relying on a pre-planned force/torque for a temporary open-loop piloting is not always feasible to address such a fierce maneuver because the flight condition is easily affected by system uncertainties and disturbances, causing serious safety consequences [75,76]. Actually, natural selection for insects and hummingbirds can be viewed as a long-term training and optimization process of their flight control strategy. In order to adapt to various goals in harsh conditions, nature's flyers acquired the skill of performing surprisingly stable and reliable maneuvers. Their reward mechanism is to gain more chances for survival under certain circumstances such as being chased or cornered. Taking this inspiration, in this thesis, we propose to incorporate machine learning to facilitate flight control.

In this thesis, we first introduce our model-based control law, which is designed to ensure the stability of the proposed hummingbird robot in normal flight (head up) (Figure 1.1.(g)). In such a design, we propose to use motor current feedback to quantify system asymmetries for trim compensation. With the balanced trim condition, we design a deterministic robust control (DRC) law to counter the undesired uncertainties and disturbances, achieving robust altitude control. From our modeling result, with a robust altitude control and thrust generation, control torques can be approximated by a single variable dominated, linear-varying term. Therefore, to reduce the computational load of onboard control, body attitude and lateral position of our hummingbird robot are controlled by a simple cascade proportional–integral–derivative (PID) controller. This design serves as our baseline control law, the accuracy and convergency speed of which is validated through experiments on free flight tests, including stable hovering and waypoint tracking. Based upon it, to achieve an optimal flip on the proposed hummingbird flapping wing robot, we focus on the integration of a learning-based control strategy to mimic the flight training in nature. In particular, Reinforcement Learning (RL) is used here to generate reliable maneuver policy for the demonstration of a flip maneuver, instead of using a traditional optimal control or a trajectory planning algorithm. The process from low-level actuation commands to the vehicle states can be modeled as a Markov Decision Process (MDP). Thus, the optimal maneuver policy can be searched in the learning process.

The proposed control strategy can not only stabilize the robot in normal flight but also work with instantaneous uncontrollable scenarios. As a hybrid flight control strategy, it combines a model-based nonlinear controller (DRC+PID) to guarantee the nominal flight stability and a model-free maneuver policy to push flight envelope and guide an aggressive maneuver. We made this control scheme on the proposed hummingbird robot because the stabilization control is ineffective during flip over due to the contradictory control effort and unmanageable control error [17]. Since our hummingbird robot equips only two actuators (DC motors), we aim to investigate if machine learning can aid bio-inspired flapping wing robots to deal with system uncertainties, varying dynamics, and demanding performance even under severely actuation constraints. We demonstrate that, although bio-inspired robots cannot replicate the elaborate actuation in animals, it can achieve flight performance that closely resembles their natural counterparts with the aiding of model-free learning.

1.2.4 Navigating Confined Spaces

Compared to flying animals, environment perception capabilities of engineered flapping wing platforms are still limited, especially when the surroundings becomes cluttered and confined. To date, employing man-made flapping wing vehicles to autonomously navigate an unexplored tight space is still an open question. Besides navigation, flapping wing vehicles flying in a tight, cluttered space also poses a huge flight safety issue since they always face inevitable collisions and wing wear and tear.

Different from the inadequacies of artificial platforms, by taking advantage of the sophisticated sensory system, flying animals exhibit extraordinary environmental adaptability [2, 13, 14]. Inspired by nature, many FWMAVs has implemented bio-inspired sensors for perception. Among them, the visual sensors are the most widely used ones. At insect-scale, Harvard Robobee implemented an ocelli-inspired sensor for its upright orientation control [77]. At bird-scale, Delfly equipped a customized stereo vision system to provide visual guidance for obstacle avoidance and environment exploration [40, 78]. However, for FWMAVs, visual sensors at such a scale have their specific usage restrictions due to light conditions, SWaP constraints, and high computational resources cost.

In turn to nature, animals rely on many other sensing approaches that can be an alternative or complementary method besides vision, providing diverse aiding information to improve the sensing capability. For example, haptic feedback also indicate surrounding changes [3, 12, 79, 80]. Inspired by the cockroaches antennas, artificial antennas are prototyped and implemented on some ground vehicles to enable bio-inspired tactile sensing [79, 80]. Without any visual cues, these works successfully demonstrated cockroach-like wall detection and following. Similarly, such a tactile sensing strategy can also be employed on the FWMAVs. Actually, wings of flying animals not only generate aerodynamic lift but also can be used to sense surrounding changes [2, 3, 12, 13]. Such dual functions of sensing and actuation coupled in one element are particularly useful for small-sized, bio-inspired robotic flyers, whose SWaP are under stringent constraint. However, to date, man-made FWMAVs generally use their wings only for actuation and rarely for sensing.

In this thesis, we propose to use motor current feedback to interpret the wing load changes and thus sense its surroundings. With wing load information, we demonstrate that the proposed hummingbird robot can provide the onboard somatosensory-like feedback as same as flying-animals: using flapping wings to navigate confined spaces without additional sensors' feedback. During the navigation, by taking advantages of the wings' material flexibility and reciprocating motion, the safety of the vehicle can be passively assured if an inevitable collision happens. In comparison, drones with rotors usually avoid for touching objects directly, e.g., one relied on a cage-like shield to ensure passive safety when traveling through narrow corridors with obstacles and turns [81, 82].

1.3 Thesis Contribution and Organization

In the course of this study, the main contributions are:

1. Systematic modeling and validation of a dual-motor at-scale flapping wing hummingbird robot.

2. Designed a novel sensor fusion algorithm for real-time onboard attitude feedback of flapping wing vehicles to compensate both wings' high-frequency reciprocating motion induced large instantaneous oscillation and sensor drift simultaneously.

3. Proposed a novel hybrid control scheme by combining model-based control with model-free reinforcement learning to enhance flight control performance and enable animal-like aggressive maneuvers.

4. Proposed the first flapping wing robot using its flapping wings in such dual functions - sensing and actuation coupled in one element for environmental perception and navigation in tight space, without the need for any auxiliary feedback.

5. Addressed the payload and power efficiency challenges of the proposed hummingbird robot to enable untethered flight through system optimization. Developed

the first bio-inspired FWMAV powered by only two actuators, whose sustained untethered stable hovering is achieved through a pair of independently controlled wings.

The rest of this thesis is organized as follows. In Chapter 2, the systematic modeling work of the proposed robot platform is introduced. In Chapter 3, a novel real-time onboard sensor fusion of flapping wing vehicles is proposed. In Chapter 4, we present a novel flight control design by combining model-based control with model-free reinforcement learning to boost the performance of FWMAVs. In Chapter 5, a strategy of using the two wings as a primary sensor to navigate tight space is proposed. In Chapter 6, the untethered flight of a dual-motor actuated at-scale hummingbird robot with bio-inspired decoupled wings is demonstrated. All of the proposed algorithms and methods above are validated through experimental flight tests. Finally, in Chapter 7, the thesis works are summarized and future works are outlined.

2. ROBOT DESCRIPTION AND MODELING

In this chapter, the flapping-wing hummingbird robot designed in Purdue Bio-robotics Lab is briefly introduced. All of the following works in this thesis, i.e., onboard sensing, flight control, navigating confined space, and untethered flight, are based upon it. The detailed schematics and parameters of such a design are elaborated. In addition, systematic modeling of the overall system is presented, including wing rotation and stroke dynamics, wing kinematics modulation, control authority analysis, and body dynamics.

2.1 System Overview

The mechanical design of the proposed flapping wing robotic hummingbird platform in this thesis is shown in Figure 2.1. It has a wingspan of 170 mm, weighs 12 grams without battery. By taking the inspiration from its natural counterparts, the kinematics of its two wings are fully decoupled, with each of them driven by a brushless DC motor independently. A pair of reduction gears are equipped on each motor for efficient torque transmission. Torsional springs paired with wings are installed to restore kinetic energy, which dominates the wingbeat frequency at system resonance (around 34Hz) to further improve actuation efficiency. Inspired by some insects' passive rotational wings [83, 84], the wing rotation angle varies passively through the effect of aerodynamic and inertial loading, meanwhile only the wing stroke motion is under active control.

The schematic drawing of a typical onboard electronic system of the proposed hummingbird robot is shown in Figure 2.2, which includes two motor drivers, a microcontroller, and an IMU sensor. Battery and onboard power boost regulators are optioned for untethered flight scenarios, which provides about 8 grams additional

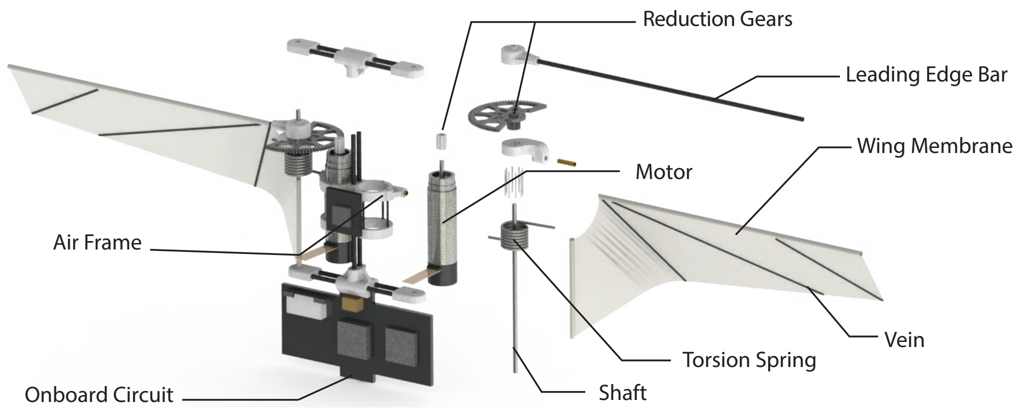

Figure 2.1. : Design of the proposed hummingbird robot.

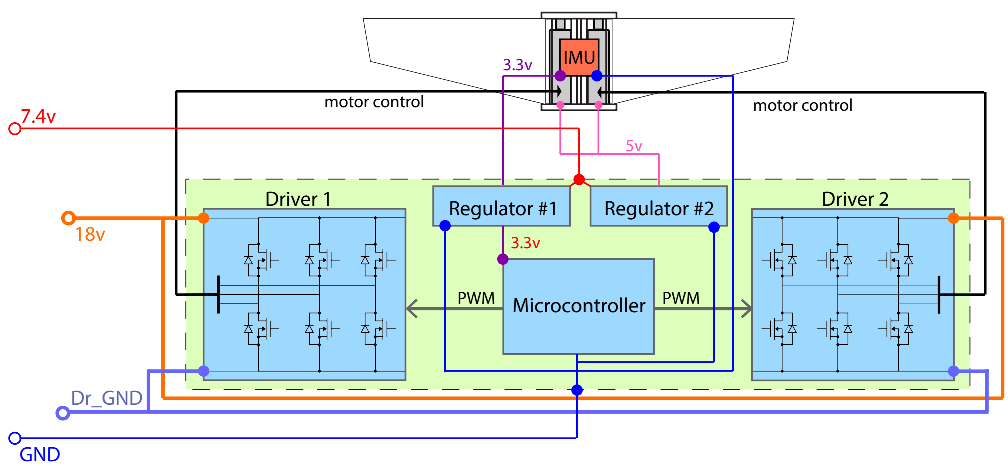

Figure 2.2. : Schematic diagram of the onboard electronic system of the proposed hummingbird robot.

weight cost. Based on different power sources, i.e., onboard or offboard, the robot demonstrates both tethered and untethered stable flight. The tethered platform, as shown in Figure 2.3, is used for designing onboard sensing, control and navigation algorithms. Untethered design tackles system optimization and integration challenges. Such onboard system integration, covering components selection, ripple suppression, power regulation, and layered circuit design, are detailed in Chapter 6.

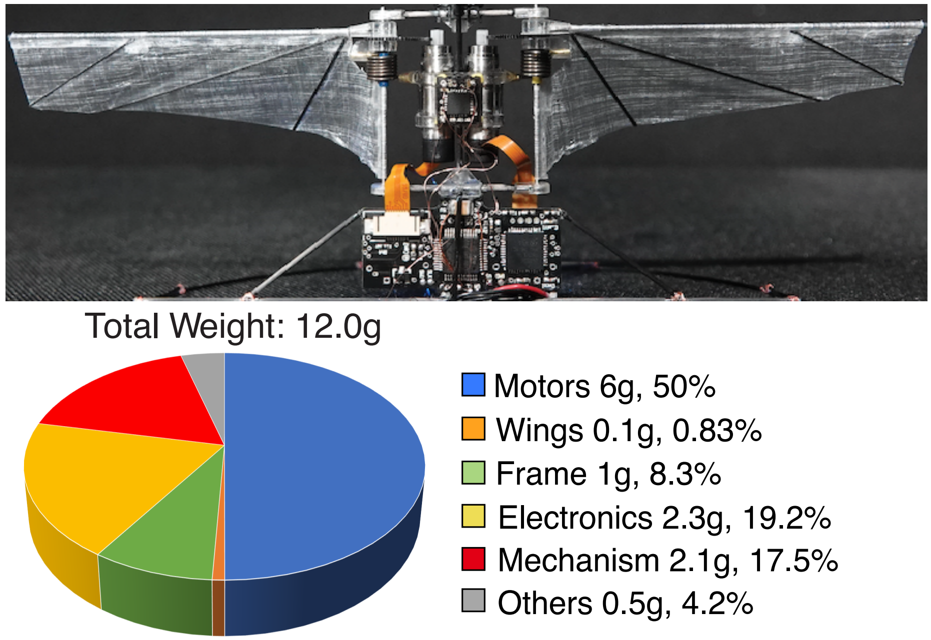

Figure 2.3. : Prototyped hummingbird robot. The system is powered through thin tether wires.

A brief summary of the design concept of the entire onboard system: With an IMU sensor, an onboard attitude estimation algorithm can be implemented to enable feedback control (Chapter 3); With reliable feedback, the microcontroller handles a hybrid control law to achieve stable flight and aggressive maneuvering (Chapter 4); Two sensing resistors are adopted to sense instantaneous wing load relying on motor current feedback, which not only facilitates vehicle control and can also be used to interpret the surrounding changes for navigation (Chapter 5). In the onboard system design, from hardware to software, we addressed sensing, control, and navigation issues. Furthermore, the payload and power efficiency issues also have been addressed through design optimization. With proper design, the proposed robot is capable of generating sufficient control effort to carry onboard power source for fully untethered flight (Chapter 6).

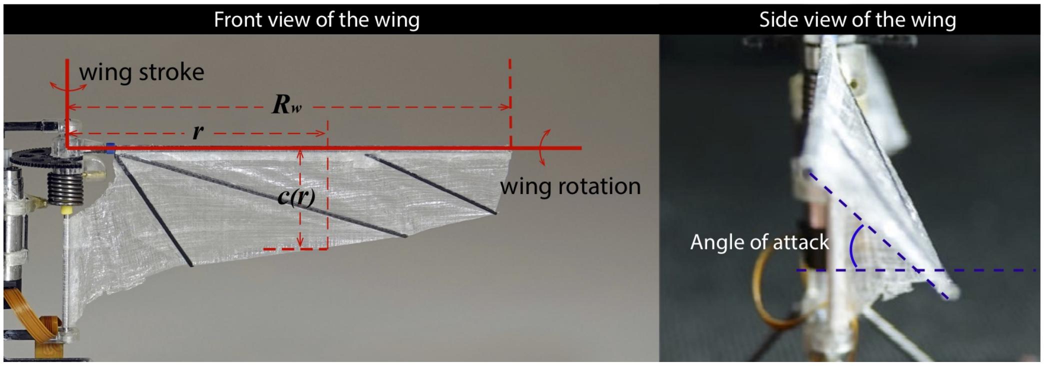

Figure 2.4. : Wing parameters of the proposed hummingbird robot.

2.2 Wing-actuation System Dynamics

Wing-actuation system is the core subsystem in FWMAVs. It generates aerodynamic lift and flight control authority for controlled flight. In order to control the hummingbird robot, understanding the dynamics of this subsystem is essential. In this section, we propose a complete, multidisciplinary dynamic model of our motor-direct-drive design.

2.2.1 Dynamics of Wing Rotation

The rotation mechanism of the robot's wings is shown in Figure 2.4. It has a bi-stable design similar to [26, 31, 32]. Clearance fitted sleeves are shaped along the leading edge and driveshaft to enable passive wing rotation. Such a morphology is inspired by the insects whose wings can perform passively rotating [83, 84]. In both upstroke and downstroke flapping motion, the wing shape of the proposed hummingbird robot can be formed with a desirable camber in order to keep the majority of the wing area having an optimal rotation angle. The formulation of our wing morphology follows Ellington's definition presented in [6].

As shown in Figure 2.4, the wing rotates about the steel shaft crossing the shoulder. The wing rotational dynamics of the proposed design is formulated by

$$J_{w_r}\ddot{\theta}_w - \frac{1}{2}J_{w_r}\dot{\psi}_w^2 \sin 2\theta_w + J_{w_{rs}}\ddot{\psi}_w \cos\theta_w = \tau_{aero} + \tau_d, \tag{2.1}$$

where J_{w_r} is the moment inertia of the wing along wing rotational direction, $J_{w_{rs}}$ is the product moment of inertia of the wing about the wing rotational and stroke directions, θ_w is the wing rotation angle, ψ_w is the wing stroke angle, τ_{aero} and τ_d are the total aerodynamic moment and rotational damping integrated along the wingspan respectively. To calculate τ_{aero} and τ_d, we need to figure out the normal force applied on the wings during flapping.

The angle of attack $\alpha = sgn(\dot{\psi}_w)\phi_w + \frac{\pi}{2}$, which denotes the angle about the fluid velocity and the wing chord. The lift and drag coefficients can be formulated by a sinusoidal function [7, 11]. From [11]

$$\begin{aligned} C_L(\alpha) &= C_{Lmax}\text{sin}(2\alpha), \\ C_D(\alpha) &= (\frac{C_{Dmax} + C_{D0}}{2}) - (\frac{C_{Dmax} - C_{D0}}{2})\text{cos}(2\alpha). \end{aligned} \tag{2.2}$$

The best fits of the coefficients are presented in [11], wherein $C_{Lmax} = 1.8, C_{D0} = 0.4, C_{Dmax} = 3.4$.

The normal force combines the lift and drag applied on the wing. The normal force coefficient $C_N(\alpha) = \cos(\alpha)C_L(\alpha) + \sin(\alpha)C_D(\alpha)$.

Using blade element theory, τ_{aero} and τ_d are

$$\begin{aligned} \tau_{aero} &= -\text{sgn}\left(\dot{\psi}_w\right)\frac{1}{2}\rho_a\dot{\psi}_w^2 C_N(\alpha)R_w^3\bar{c}^2\hat{d}_{cp}\hat{z}_{cp}, \\ \tau_d &= -\frac{1}{8}|\dot{\theta}_w|\dot{\theta}_w C_{rd}R_w\bar{c}^4\hat{z}_{rd}, \end{aligned} \tag{2.3}$$

where ρ_a is the air density, R_w is the wing length, $\bar{c}$ is mean chord length of the wing, $\hat{d}_{cp}$ is the non-dimensional center of pressure from the leading edge bar, and C_{rd} is the wing rotational damping coefficient. The two integral constants are $\hat{z}_{cp} = \int_0^1 \hat{r}^2\hat{c}(\hat{r})^2 d\hat{r}$ and $\hat{z}_{rd} = \int_0^1 \hat{c}(\hat{r})^4 d\hat{r}$ where $\hat{r}$ and $\hat{c}$ are the non-dimensional axes along wing span-wise and wing chord-wise direction, respectively [7, 11].

Based on the dynamic model above, the numerical solution of the wing rotation angle can be determined given a certain wing stroke kinematics. With the camber wing design, the angles of attack of the wings have been optimized to 45° approximately, which determines the aerodynamic drag coefficient C_D [7]. Subsequently, The cycle-averaged aerodynamic damping coefficient can be solved by

$$B_w = \frac{1}{2}\rho_a \bar{C}_D R_w^4 \bar{c}\hat{r}_3^3. \tag{2.4}$$

where $\bar{C}_D$ is cycle-averaged drag coefficient, $\hat{r}_3^3$ is the 3rd dimensionless moment of wing area [6]. B_w is used to derive the aerodynamic damping applied on the wing, which represents a time-varying aerodynamic load of the wing-actuation system.

2.2.2 Dynamics of Wing-actuation System

The wings of the proposed hummingbird robot are directly actuated by their paired dc motors. Therefore, the wing-actuation system can be modeled as a spring-mass-damper system combining with the aerodynamic load. The dynamics is given by

$$J_m\ddot{\psi}_m + B_m\dot{\psi}_m = \tau_m - \tau_{ext}, \tag{2.5}$$

where J_m is the moment of inertia of the motor, ψ_m is the motor rotation angle, B_m is the damping constant of the motor, τ_m is motor torque output, and τ_{ext} denotes the overall external motor loading.

Motor torque output $\tau_m = K_a i_a$, where K_a is motor torque constant and i_a is motor armature current. τ_{ext} is mainly comprised by the moment of inertia of the wing (J_w) and the reduction gear (J_g), wing's aerodynamics damping B_w during flapping, and the wing motion induced elastic restoring torque $K_s\psi_w$ (wherein K_s is the spring coefficient and ψ_w is the instantaneous wing stroke angle). Through the gear transmission, the total motor loading is

$$\tau_{ext} = \frac{[(J_w + J_g)\ddot{\psi}_w + B_w\dot{\psi}_w^2 sgn(\dot{\psi}_w) + K_s\psi_w]}{\eta_g N_g}. \tag{2.6}$$

where N_g is the gear ratio, η_g is the gear efficiency. With the gear transmission, $\psi_m = N_g \psi_w$.

For motor control, an on-board driver circuit is needed to generate periodic alternating phase-phase voltage to adjust motor torque and spinning direction. By neglecting the small motor inductance, the electric model of the motor-driven system can be approximated by

$$u - i_a R_a = K_a \dot{\psi}_m, \tag{2.7}$$

where u is the motor drive voltage and R_a is the motor winding resistance. Note, for an actual system, R_a is not a constant due to the motor thermal effect. The expression for resistance change is

$$R_a = R_0(1 + \gamma_{c_u}(T_w - T_\infty)), \tag{2.8}$$

where R_0 is the winding resistance under ambient temperature, γ_{c_u} is thermal effect coefficient of copper winding which is $0.00383°C^{-1}$, T_w is the current winding temperature, and T_∞ is ambient temperature. If R_a increased too much, more energy would wast on heat dissipation, which results in insufficient power for actuation. When flapping-wing MAV is doing aggressive maneuver or flying in a deteriorated weather condition (e.g., counter big wind gust), it needs to overdrive the motor temporarily for stabilization, which causes the motor to overheat. In this situation, the wing stroke amplitude and lift force decrease significantly. Meanwhile, the attitude stabilization is affected in series due to the inherent coupling between lift force and 3-axis body torque [33]. Therefore, in order to sustain a consistent flight performance, accommodating the motor thermal effect is necessary.

2.2.3 System Efficiency

Since the wing is driven around its natural resonance frequency, the inertial torque and elastic torque are balanced [29]. Thus, the electrical characteristics of this motor-driven system can be approximated by

$$\begin{aligned} i_a &= \frac{1}{N_g k_a}(B_l + B_w\dot{\psi}_w)\dot{\psi}_w, \\ u &= K_a\dot{\psi}_m + i_a R_a, \end{aligned} \tag{2.9}$$

where B_l is the lumped linear damping coefficient.

With u and i_a, the cycle-averaged input power $\bar{P}_{in}$ is

$$\bar{P}_{in} = \frac{1}{T}\int_T |u| \cdot i_a. \tag{2.10}$$

During the flap motion, with the time-variant aerodynamic load, the cycle-averaged wing drag cost $\bar{P}_d$ is

$$\bar{P}_d = \frac{1}{T}\int_T B_w\dot{\psi}_w^{\,2} sgn(\dot{\psi}_w)dt. \tag{2.11}$$

Therefore, the cycle-averaged system efficiency $\bar{\eta}$ can be estimated by

$$\bar{\eta} = \zeta\frac{\bar{P}_d}{\bar{P}_{in}}, \tag{2.12}$$

where ζ is power regulation efficiency.

2.3 Wing Kinematics Modulation

Like flying animals, the proposed hummingbird robot adopts a pair of reciprocal wing-actuation systems with horizontal stroke planes in order to enable flight control (Figure 2.6). Each wing is driven independently by a DC motor. Thus, the two wings are fully decoupled and generate independent wing kinematic trajectories. With proper wing motion profile design and modulation, the two wings are capable of generating aerodynamic thrust and control torques. Such a unique design is severely underactuated, i.e., using only two actuators to demonstrate the capability of 6-DoF controlled flight, which provides a great challenge of flight control.

The wing modulation technique as introduced in [85] is used here to generate the roll, pitch, yaw torque and thrust by four parameters respectively: the differential voltage amplitude of left and right wings δV, the mean voltage bias V_0, the split-cycle parameter change $\delta\sigma$, and the input voltage amplitude V_{I0}. The two input voltages follow a modulated sinusoidal form

$$u_i = \begin{cases} V_{I_i}\cos\left(\frac{2\pi f t}{2\sigma_i}\right) + V_0 & \text{if } 0 \le t \le \frac{\sigma_i}{f} \\ V_{I_i}\cos\left(\frac{2\pi f t - 2\pi}{2(1-\sigma_i)}\right) + V_0 & \text{if } \frac{\sigma_i}{f} \le t \le \frac{1}{f} \end{cases} \tag{2.13}$$

where i represents the left ($i = 0$) or right motor ($i = 1$), $V_{I_i} = V_{I_0} + (-1)^i \delta V$ and $\sigma = 0.5 - (-1)^i \delta\sigma$.

With such wing control command, the steady-state wing kinematic response is shown in Figure 2.6, which generates the following stroke trajectory [36, 50]

$$\psi_{w_i} = \begin{cases} \Psi_{w_i}\cos\left(\frac{2\pi f t}{2\sigma_{w_i}} + \beta_i\right) + \psi_{w0} & \text{if } 0 \le t \le \frac{\sigma_{w_i}}{f} \\ \Psi_{w_i}\cos\left(\frac{2\pi f t - 2\pi}{2(1-\sigma_{w_i})} + \beta_i\right) + \psi_{w0} & \text{if } \frac{\sigma_{w_i}}{f} \le t \le \frac{1}{f} \end{cases} \tag{2.14}$$

where ψ_{w_0} is bias angle, β is phase shift and σ_{w_i} is the resulting split-cycle parameter.

In order to validate the modeled wing kinematics, we conduct experimental tests. The test setup is shown in Figure 2.5. A high-speed head camera (*Photron FAST-CAM Mini UX50 high-speed camera*) is set to capture the wing motion. A 6-axis force/torque transducer (*Nano17, ATI Ind. Automation*) is used to measure the corresponding thrust and control torque generated by the robot's two wings. A NI data acquisition box (*NI SC-86 DAQ*) is connected to a desktop for force/torque measurements logging. The head camera view is shown in Figure 2.5.(a). With high-speed video, the instantaneous wing rotation and stroke angle can be digitized. Wings are actuated by the onboard driver circuits. Both wing rotation and stroke responses are validated as shown in Figure 2.5.(b).

To quantify the ability of the torques and thrust generation, we define the kinematic force gains as the ratio between resulting forces/torques and kinematics change from trim condition (stable hovering). The nominal kinematics is $\Psi_{w_1} = \Psi_{w_0}$, $\beta_i = 0$,

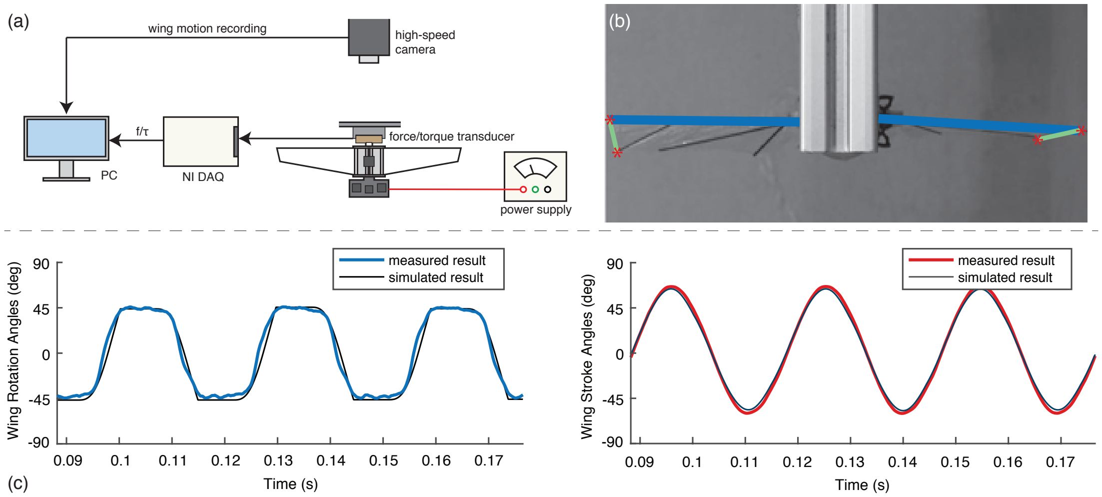

Figure 2.5. : (a). Experimental setup for wing kinematics validation and instantaneous lift/torque measurement. (b). Head camera view in wing motion validation. (c). Validation results of wing rotation and stroke angle in three typical wing beats.

$\psi_{w0} = 0$ and $\sigma_{w_i} = 0.5$, i.e., the body control torque is balanced, and the thrust generated by the two wings equals to the body weight: $mg = \bar{F}_L$.

The kinematic force gains can be derived from the nominal kinematics parameters based on the assumption of near-hover condition [55, 86].

The control torque and thrust are formulated by:

1. Thrust F_z is adjusted by symmetric amplitude change, with $\Psi_{w_l} = \Psi_{w_r} = \Psi_{w_t} = \Psi_{w_0} + \delta\Psi_w$

$$
\begin{aligned}
F_z &= \frac{1}{2}\rho_a \bar{C}_L R_w^3 \bar{c}\hat{r}_2^2(S)\omega_n^2 \Psi_{w_t}^2 = F_0 v_1^2, \\
v_1 &= \frac{\delta\Psi_w}{\Psi_{w_0}} + 1 \approx \frac{1}{\Psi_{w_0}\omega_n}\frac{K_u}{\sqrt{B_l^2 + 4B_w V_I K_u}}\delta V_{I_0} + 1
\end{aligned}
\tag{2.15}
$$

where $F_0 = mg$, $K_u = \eta_g N_g \frac{K_a}{R_a}$ is the gain of the motor input, $V_{I_0} = V_I + \delta V_{I_0}$ and V_I is the nominal voltage amplitude for hovering.

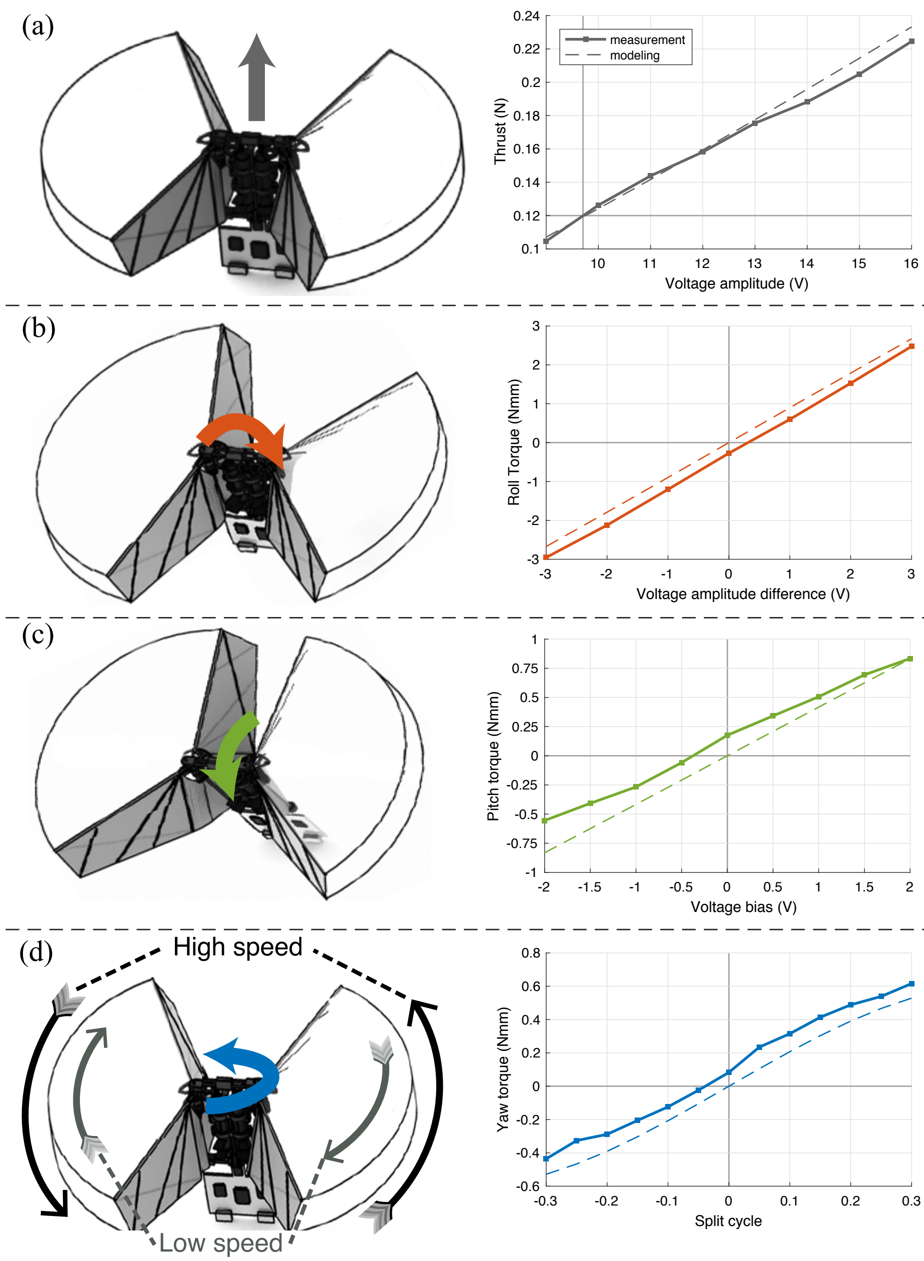

Figure 2.6. : (a), (b), (c), (d) illustrate the wing modulations for the thrust and roll, pitch, and yaw torque generation, respectively. Experimental validations of the modeled thrust and torque generation are shown accordingly. Gray-cross indicates the nominal operating point.

2. Roll torque is produced with asymmetric amplitude change, with $\Psi_{w_l} = \Psi_{w_t} + \delta\Psi_w$ and $\Psi_{w_r} = \Psi_{w_t} - \delta\Psi_w$.

$$\begin{aligned}
\tau_\phi &= \frac{1}{2}\rho_a \bar{C}_L R_w^3 \bar{c}\hat{r}_2^2(S)\omega_n^2 \Psi_{w_t}^2 r_{cp}\left(\frac{2\delta\Psi_w}{\Psi_{w_t}}\right) \\
&= r_{cp}F_0 \frac{\Psi_{w_t}}{\Psi_{w_0}}\frac{2\delta\Psi_w}{\Psi_{w_0}} = r_{cp}v_1 v_2 \\
v_2 &= \frac{2\delta\Psi_w}{\Psi_{w_0}} \approx \frac{2}{\Psi_{w_0}\omega_n}\frac{K_u}{\sqrt{B_l^2 + 4B_w V_I K_u}}\delta V
\end{aligned} \tag{2.16}$$

where r_{cp} is the span wise center of pressure and $\delta\Psi$ is the change of amplitude.

3. Pitch torque is generated by shifting mid stroke position for both wings

$$\begin{aligned}
\tau_\theta &= r_{cp}F_z \sin\psi_{w_0} = r_{cp}F_0 v_1^2 v_3 \\
v_3 &= \sin\psi_{w_0} \approx \psi_{w_0} = \frac{K_u}{K_s}V_0
\end{aligned} \tag{2.17}$$

4. Yaw torque is realized using antisymmetric split-cycle modulation with $\sigma_{w_l} = 0.5 - \delta\sigma_w$ and $\sigma_{w_r} = 0.5 + \delta\sigma_w$

$$\begin{aligned}
\tau_\psi &= \frac{1}{8}\rho_a \bar{C}_D R_w^4 \bar{c}\hat{r}_3^3(S)\omega_n^2 \Psi_{w_t}^2 \left(\frac{1-2\sigma_w}{\sigma_w(1-\sigma_w)}\right) \\
&= r_{cp}F_0 \frac{\bar{C}_D}{\bar{C}_L} v_1^2 v_4 \\
v_4 &= \frac{\bar{C}_D}{\bar{C}_L}\left(\frac{1-2\sigma_w}{4\sigma_w(1-\sigma_w)}\right) \approx 2\delta\sigma_w = 2k_{sc}\delta\sigma
\end{aligned} \tag{2.18}$$

where k_{sc} is a scaling factor. This scaling is due to the strong attenuation of the flapping wing dynamics to the non-sinusoidal excitation with split cycle. This factor can be quantified through a simple FFT analysis [33]. For our specific design, it is around 0.1.

The proposed formulation of the thrust and control torque is verified experimentally, as shown in Figure 2.6. The experimental result matches the analytical prediction. The offsets between measurement and modeling results are due to the manufacturing imperfection of the vehicle. Despite our best effort to maintain the symmetry and consistency of the vehicle's components, these offsets cannot be eliminated completely due to the semi-manual fabrication process. To achieve stable flight, it requires sufficient control effort and closed-loop control to compensate for the negative effect of such system asymmetries.

2.4 Body Dynamics

Body motion of flapping flight induces additional forces and torques on the wing through the kinematic coupling. Such effects due to additional aerodynamic damping caused by body motion during different phases of wing motion are modeled and presented as flapping counter forces (FCFs) and flapping counter torques (FCTs) [55]. It is a unique aerodynamic phenomenon for FWMAVs that can directly change flight dynamics and affect flight control bandwidth. To improve the control bandwidth and flight performance, such coupling cannot be ignored in the modeling of vehicle body dynamics. In this section, we present the body dynamics of the flapping-wing vehicle taking consideration of wing motion induced passive damping.

The coordinate definition is shown in Figure 2.7. For flight control law design, the vehicle is approximated as the standard rigid body system

$$\begin{cases} \dot{\boldsymbol{P}} = \boldsymbol{V} \\ m\ddot{\boldsymbol{P}} = \boldsymbol{R}\boldsymbol{f}^b + m\boldsymbol{g} \\ \dot{\boldsymbol{R}} = \boldsymbol{R}[\boldsymbol{\omega}^b_\times] \\ \boldsymbol{I}\dot{\boldsymbol{\omega}}^b = \boldsymbol{\tau}^b - \boldsymbol{\omega}^b \times \boldsymbol{I}\boldsymbol{\omega}^b \end{cases} \tag{2.19}$$

where $\boldsymbol{P} = [x, y, z]^T$ is the position vector of the vehicle in the inertial frame XYZ which is defined by North-East-Up (NEU); $\boldsymbol{V}$ is the velocity vector of the vehicle in the inertial frame; m is the total mass; $\boldsymbol{g} = [0, 0, -1]^T$ is the normalized gravity acceleration vector; $\boldsymbol{R}$ is the rotation matrix; $[\bullet_\times]$ denotes the skew-symmetric matrix mapping from vector dot product to cross product; $\boldsymbol{I}$ is the inertia matrix of the vehicle; $\bullet^b$ represents the vector in the body frame $x^b y^b z^b$, e.g., the thrust vector $\boldsymbol{f}^b = [0, 0, f_z]^T$, the vehicle angular velocity $\boldsymbol{\omega}^b = [p, q, r]^T$, and the 3-axis control torque $\boldsymbol{\tau}^b = [\tau_x, \tau_y, \tau_z]^T$.

The overall stroke-averaged wrenches from the flapping wings are given by

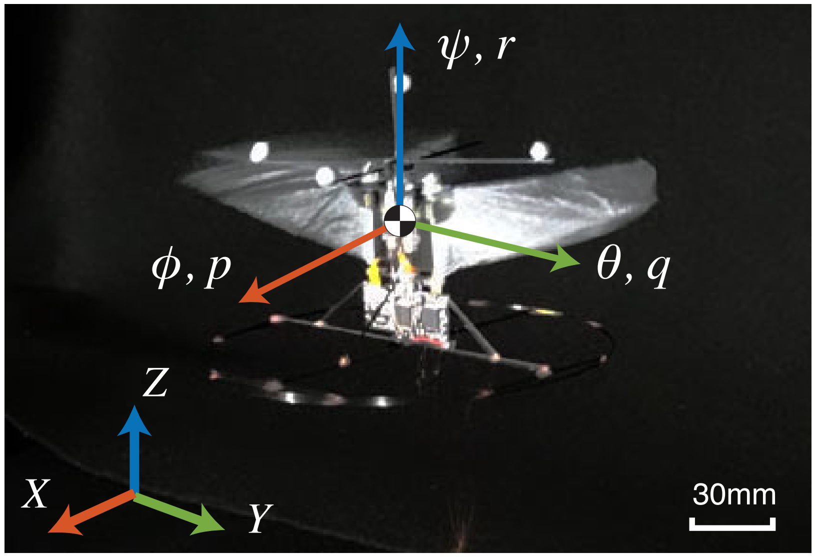

Figure 2.7. : Coordinate definition of the vehicle body frame and the inertial frame.

$$\boldsymbol{f}^b = \underbrace{\begin{bmatrix} 0 \\ 0 \\ f_z \end{bmatrix}}_{\boldsymbol{f}_n^b} + \underbrace{\begin{bmatrix} -c_x u - c_x d_s q \\ -c_y v + c_y d_s p \\ -c_z w \end{bmatrix}}_{\boldsymbol{f}_d^b},$$

$$\boldsymbol{\tau}^b = \underbrace{\begin{bmatrix} \tau_x \\ \tau_y \\ \tau_z \end{bmatrix}}_{\boldsymbol{\tau}_n^b} + \underbrace{\begin{bmatrix} d_s c_y v - (d_s^2 c_y + c_\phi) p \\ -d_s c_x u - (d_s^2 c_x + c_\theta) q \\ -c_\psi r \end{bmatrix}}_{\boldsymbol{\tau}_d^b}, \tag{2.20}$$

where $\boldsymbol{f}_n^b$ and $\boldsymbol{\tau}_n^b$ are the nominal wrenches, $\boldsymbol{f}_d^b$ and $\boldsymbol{\tau}_d^b$ are the damping wrenches, $f_z, \tau_x, \tau_y, \tau_z$ are the four inputs of the system, d_s is the offset between the stroke plane and the center of mass, $[u, v, w]^T$ is the body translational velocity vector in the body frame, and $c_\bullet$ denotes the 3-axis FCF/FCT.

From [55], for the platform with a pair of wings at near-hovering condition, the damping coefficients can be formulated by

$$\begin{bmatrix} c_x \\ c_y \\ c_z \\ c_\phi \\ c_\theta \\ c_\psi \end{bmatrix} = \begin{bmatrix} 2\rho_a R_w^2 \bar{c} \Psi_{w0} \omega_n \hat{r}_1^1 \overline{C_D \cos^2(\psi_w) |\frac{d\hat{\psi}_w}{d\hat{t}}|} \\ 2\rho_a R_w^2 \bar{c} \Psi_{w0} \omega_n \hat{r}_1^1 \overline{C_D \sin^2(\psi_w) |\frac{d\hat{\psi}_w}{d\hat{t}}|} \\ \rho_a R_w^2 \bar{c} \Psi_{w0} \omega_n \hat{r}_1^1 \overline{\frac{dC_N(\alpha)}{d\alpha}|_{\alpha_0} \cos(\alpha_0) |\frac{d\hat{\psi}_w}{d\hat{t}}|} \\ \rho_a R_w^4 \bar{c} \Psi_{w0} \omega_n \hat{r}_3^3 \overline{\frac{dC_N(\alpha)}{d\alpha}|_{\alpha_0} \cos(\alpha_0) \cos^2(\psi_w) |\frac{d\hat{\psi}_w}{d\hat{t}}|} \\ \rho_a R_w^4 \bar{c} \Psi_{w0} \omega_n \hat{r}_3^3 \overline{\frac{dC_N(\alpha)}{d\alpha}|_{\alpha_0} \cos(\alpha_0) \sin^2(\psi_w) |\frac{d\hat{\psi}_w}{d\hat{t}}|} \\ 2\rho_a R_w^4 \bar{c} \Psi_{w0} \omega_n \hat{r}_3^3 \overline{C_D |\frac{d\hat{\psi}_w}{d\hat{t}}|} \end{bmatrix} \tag{2.21}$$

wherein $\hat{t} = \omega_n t$ is the non-dimensional time, Ψ_{w_0} is the nominal stroke amplitude, $\frac{d\hat{\psi}_w}{d\hat{t}}$ is the non-dimensional flapping velocity of the wing.

3. ONBOARD ATTITUDE SENSING

On small scale FWMAVs, the high-frequency reciprocating wing motion introduces severe instantaneous body oscillations. Such oscillations affect the reading accuracy of onboard inertial sensors seriously, resulting in poor performance of real-time attitude sensing of the vehicle. In this chapter, we present a sensor fusion design for onboard attitude sensing of FWMAVs by using an of-the-shelf IMU sensor. The proposed design is composed of a model-based compensation scheme and an adaptive sensing error estimator. The effect of both sensing drift and undesired aerodynamic forces has been addressed. Such a design has been validated on our hummingbird robot in both indoor and outdoor flight. The experimental results have demonstrated the accuracy, convergence, and robustness of the proposed sensor fusion algorithm.

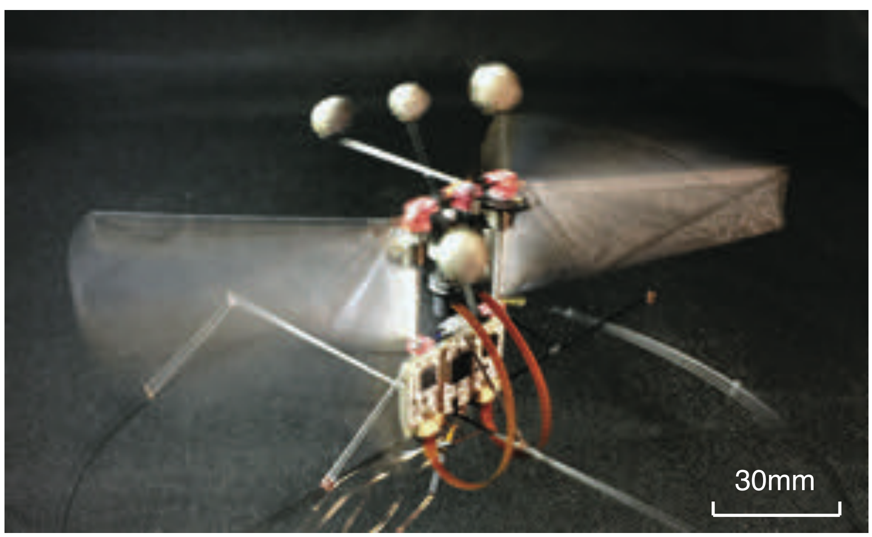

Figure 3.1. : Reciprocating wing motion causes severe body vibration.

3.1 Introduction

Though the development of flapping-wing MAVs has witnessed tremendous progress over the past years, there remain open challenges that must be addressed in order for them to approach the flight performance of their natural counterparts. Among those challenges, with the design constraints and especially with the introduced severe vibration from the high-frequency flapping motion of current FWMAVs, real-time onboard attitude sensing is still not fully solved yet, as discussed in Chapter.1.2.2.

On FWMAVs, in order to cope with the stringent size and weight constraints, MEMS-based IMU sensors are typically used for onboard attitude sensing. It has been demonstrated that IMU sensors work well on conventional MAVs (with fixed or rotary wings) with proper sensor fusion algorithms [51–53, 87, 88]. However, for FWMAVs, direct adoption of conventional sensor fusion algorithms usually results in poor performance [26, 49, 50, 56]. The sensing errors are largely caused by the severe oscillation induced by wings' reciprocating motion, complex time-varying aerodynamics, and sensor drift [57].

In order to enable onboard feedback control, in this chapter, we introduce an onboard sensor fusion algorithm that can attenuate the severe sensing error caused by body oscillation from high-frequency, high-amplitude wing motion. The sensing performance has been experimentally validated on the proposed hummingbird robot through several flight tests. All of the flight tests were conducted into a VICON space (an external camera-based motion capture system, check *www.VICON.com*). The VICON data provides ground truth with a certain communication delay. Two flight scenarios have been studied, i.e., hovering and maneuvering. The results demonstrate the accuracy and robustness of the proposed sensor fusion method for FWMAVs.

3.2 Sensor Fusion Design

In this section, we introduce our novel sensor fusion solution for FWMAVs' onboard attitude sensing. It consists of aerodynamic force compensation, external magnetic field correction, and adaptive sensing error estimation. To avoid singularities in geometric transformation, all of the attitude calculation is based on quaternion theory. The test platform is the proposed hummingbird robot in this thesis. An MPU9250 IMU is implemented on our test platform due to its lightweight, compact size, and reliable performance [89].

As shown in Figure 3.1, body frame and inertial frame are defined respectively. The origin of the body frame is docked at the center of the onboard IMU. IMU is placed close to the Center of Mass (CoM) of our robot. A NEU (local north, east, up) coordinate is chosen for the inertial frame as aircraft frequently used. Orientation quaternion $\boldsymbol{q}$ is defined as $[q_0, q_1, q_2, q_3]^T \in R^4$. The corresponding Euler angle representation of vehicle body attitude can be converted from $\boldsymbol{q}$ trivially.

$$\begin{aligned}
\theta &= atan2(2q_2q_3 + 2q_0q_1, 1 - 2q_1^2 - 2q_2^2), \\
\phi &= asin(2q_0q_2 - 2q_3q_1), \\
\psi &= atan2(2q_0q_3 + 2q_1q_2, 1 - 2q_2^2 - 2q_3^2),
\end{aligned} \tag{3.1}$$

where θ, ϕ and ψ are roll, pitch and yaw Euler angle respectively.

3.2.1 Modeling of Sensor Readings

The raw data of IMU includes the vehicle linear acceleration, magnetic field and angular velocity, which can be modeled by

$$\begin{aligned}
\boldsymbol{a} &= \boldsymbol{R(q)g} + \boldsymbol{a_{ex}} + \boldsymbol{b_a} + \boldsymbol{n_a}, \\
\boldsymbol{\omega} &= \bar{\boldsymbol{\omega}} + \boldsymbol{b_g} + \boldsymbol{n_g}, \\
\boldsymbol{m} &= \boldsymbol{R(q)M} + \boldsymbol{b_m} + \boldsymbol{n_m},
\end{aligned} \tag{3.2}$$

where $\boldsymbol{a}, \boldsymbol{\omega}, \boldsymbol{m} \in R^3$ are raw data of acceleration, body angular rate and magnetic field, respectively. $\boldsymbol{R}(\boldsymbol{q})$ is the quaternion represented rotation matrix which aligns inertial frame and body frame. $\boldsymbol{g} = (0, 0, -1)^T$ and $\boldsymbol{M} = (m_N, 0, m_D)^T$ are normalized gravitational acceleration and magnetic field, which construct a local NED coordinate. Sensor biases $\boldsymbol{b_a, b_g, b_m}$ can be investigated by Allan variance [57]. Sensor noise $\boldsymbol{n_a}, \boldsymbol{n_g}, \boldsymbol{n_m}$ are assumed as zero-mean Gaussian white noises. $\boldsymbol{a_{ex}}$ denotes the external acceleration applied to the sensor. During flapping flight, $\boldsymbol{a_{ex}} \neq \mathbf{0}$ due to the time-varying aerodynamic forces caused by the flapping wings. From Figure 3.2, $\boldsymbol{a_{ex}}$ is prominent in accelerometer's measurement, which affects the useful gravitational information in attitude sensing. From SNR comparison, the gravitational output is about 30 times less than wing-flapping effect. Therefore, external acceleration compensation is critical to mitigate accelerometer errors caused by wings.

In addition to the effect of vibration, magnetometers, and gyroscopes also have other flaws. For instance, the magnetic field radiated by the motor can disrupt magnetometer readings, and output drift on the gyroscope is difficult to correct due to bias and noise uncertainty. To solve these issues, in the sensor fusion algorithm, we first compensate external acceleration based on aerodynamic forces approximation. We then calibrate the magnetometer to obtain an accurate inertial frame magnetic field by using gravity vector only. In addition to the calibration, an adaptive observer is designed for overall sensing error estimation and correction based on all IMU readings.

3.2.2 External Acceleration Compensation

To obtain a valid accelerometer reading, extra accelerations produced by flapping-wings need to be subtracted from the sensor output. Such additional acceleration can be approximated by aerodynamic force modeling. On the hummingbird robot, the wings are independently driven by two brushless DC motors, which can be modeled as a spring-mass-damper system with extra aerodynamic damping. Referring to the modeling work in Chapter 2, the wing subsystem dynamic is

$$J_s\ddot{\psi}_w + B_l\dot{\psi}_w + B_w\dot{\psi}_w^2 sgn(\dot{\psi}_w) + K_s\psi_w = K_u u \tag{3.3}$$

where ψ_w is the wing stroke angle, J_s is the total moment of inertia, B_l and B_w are the linear and aerodynamic damping coefficients, respectively, K_u is the lumped motor voltage input gain.

To solve the responses of equation (3.3) around the natural frequency $\omega_n \approx 34\text{Hz}$, we use the method of multiple time scales [90,91] for analyzing: Given the dimensionless perturbation term $\epsilon = B_w/J_s$, which is the normalized linear damping coefficient, the new time variable is scaled by $T_i = \epsilon^i t, i = 0, 1, 2...$ and the first-order approximation $\psi_{w0} = \Psi_w cos(\omega_n T_0 + \beta(T_1)) + \mathcal{O}(\epsilon)$ can be used for aerodynamic forces estimation.

The wing is driven by a sinusoidal voltage input u with amplitude V_I. The steady-state solution of the approximation is

$$\begin{aligned} \Psi_w &= \frac{3\pi}{16 B_w \omega_n} \left(\sqrt{B_l^2 + \frac{32 K_u B_w V_I}{3\pi}} - B_l \right), \\ \beta &= -\frac{\pi}{2}. \end{aligned} \tag{3.4}$$

Thus, the wing stroke angle can be approximated by $\psi_w(t) = \Psi_w cos(\omega_n t + \beta)$, which is experimentally validated as presented in Chapter 2.

Quasi-steady model can be used for aerodynamic lift (F_L) and drag (F_D) calculation [7] in normal flight condition, which fits the aerodynamic behavior of our wings and works with a relatively low computation load because of its simplified formulation. The instantaneous aerodynamic lift and drag applied on the flapper can be calculated by

$$\begin{aligned} F_L &= \frac{1}{2} \rho_a C_L(\alpha) R_w^3 \bar{c} \hat{r_2}^2 \dot{\psi}_w^2, \\ F_D &= \frac{1}{2} \rho_a C_D(\alpha) R_w^3 \bar{c} \hat{r_2}^2 \dot{\psi}_w^2, \end{aligned} \tag{3.5}$$

where ρ_a is the air density, F_L and F_D respectively denote aerodynamics lift and drag applied on the wings, $C_L(\alpha)$ and $C_D(\alpha)$ are corresponding lift and drag coefficients where the angle of attack α is close to $45°$ as validated in Chapter 2.

Note, it is preferred to have additional sensors that aids to acquire reliable wing motion feedback, e.g., speed, position, or current feedback of the motor [44, 92], since the $\psi_w(t)$ can be easily obtained instead of using the approximation way above. Compared to the model-based estimation, direct sensing and interpretation of motor current can also capture the unsteady aerodynamic drag, increasing the accuracy of the sensor fusion result.

The aerodynamics on vehicle body frame can be calculated as

$$\boldsymbol{f^b_{a_{ex}}} = \begin{bmatrix} F^l_D cos(\psi_{lw}) sgn(\dot{\psi}_{lw}) + F^r_D cos(\psi_{rw}) sgn(\dot{\psi}_{rw}) \\ F^l_D sin(\psi_{lw}) sgn(\dot{\psi}_{lw}) - F^r_D sin(\psi_{rw}) sgn(\dot{\psi}_{rw}) \\ F^l_L + F^r_L \end{bmatrix}, \tag{3.6}$$

where ψ_{lw} and ψ_{rw} are stroke angles of left side and right side wing respectively. With $\boldsymbol{f^b_{a_{ex}}}$, the subtraction of external acceleration can generate a relative clean accelerometer output for sensor fusion. With compensation, the improvement of SNR is shown in Figure 3.2. However, $\boldsymbol{a^b} = \boldsymbol{a} - \boldsymbol{a_{ex}}$ cannot be directly adopted for attitude estimation because the compensation process introduces new approximation errors. Moreover, other types of sensor noise still exist.

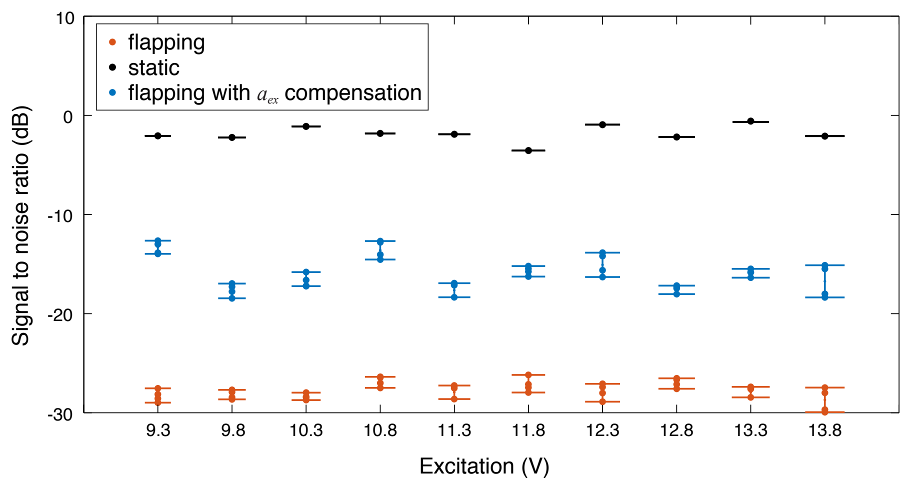

Figure 3.2. : Pitch-axis acceleration SNR in the static and oscillated condition. The noise is orders of magnitudes higher with the wing motion effect. a_{ex} compensation increases the SNR effectively on flapping wing platform.

3.2.3 Magnetometer Calibration

The magnetometer can evaluate the magnetic field on the inertial frame. From sensor characteristics, the raw magnetometer outputs include substantial errors introduced by vicinity electronics, metals, and actuators. Specifically, on our robotic hummingbird, the main magnetic disturbance is from the reciprocating spinning of the two motors.

Due to the static nature of the hardware configuration and the established operating point of the vehicle, a constant offset on the raw magnetometer measurements are observed during flight. So b_m can be removed by sensor calibration wherein the magnetometer signals between motor run/stop are compared. The offset cancellation result shows in Figure 3.3, where the red line reports the measured Y-axis magnetic field in the absence and presence of the disturbance, and moreover, the blue line represents the offset cancellation result.

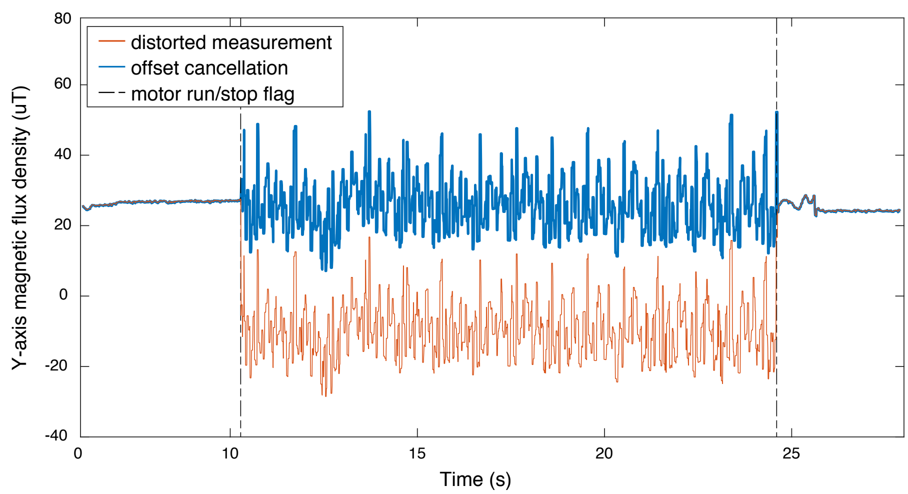

Figure 3.3. : Magnetometer calibration. Motor introduced offset is compensated.

To estimated full orientation, it requires an accurate measurement of the magnetic field in the inertial frame. The typical approach relies on magnetic field mapping. However, it is affected by a lot of unsettled distortions in some particular environments and implementation cases. The method we present in this section relies on $\vec{g}$ only to map the magnetic field orientation from the body frame to the inertial frame.

Body frame gravity distribution can be expressed by $\boldsymbol{R(q)\vec{g}}$, so the magnetic field direction in the inertial frame can be updated through

$$\begin{aligned}
&(\boldsymbol{R(q)\vec{g}})^{\boldsymbol{T}}\boldsymbol{R(q)M} = (\boldsymbol{R(q)\vec{g}})^{\boldsymbol{T}}m, \\
&\Rightarrow \boldsymbol{\vec{g}^T M} = (\boldsymbol{R(q)\vec{g}})^{\boldsymbol{T}}m, \\
&\Rightarrow m_D = (\boldsymbol{R(q)\vec{g}})^{\boldsymbol{T}}m, \\
&\quad m_N = \sqrt{1 - m_D^2}.
\end{aligned} \tag{3.7}$$

The overall measurement error of orientation in accelerometer-magnetometer system can be updated by

$$\boldsymbol{y_{err}(q, a^b, m)} = \begin{bmatrix} \boldsymbol{a^b} - \boldsymbol{R}(\boldsymbol{q})\boldsymbol{g} \\ \boldsymbol{m} - \boldsymbol{R}(\boldsymbol{q})\boldsymbol{M} \end{bmatrix} \in R^{6\times 1}. \tag{3.8}$$

Error function $\boldsymbol{y_{err}(q, a^b, m)}$ indicates the unknown sensor noise combined with the discrepancy between sensor measurements and NED reference which needs a correction.

3.2.4 Adaptive Orientation Update

To achieve an accurate and drift-free attitude estimation $\boldsymbol{\hat{q}}$, the sensor fusion algorithm is designed to cancel the overall sensing error adaptively. The rough attitude can be estimated via a simple integration of gyroscope data due to the following reasons:

1. Compared with the other two sensors in the IMU system, gyroscope is more robust at a certain high-frequency working condition. The rate-noise spectral density of MPU9250 is only $0.01°/s/\sqrt{Hz}$, which can be neglected at flapping resonance frequency in contrast to the acceleration noise.

2. From the Allan variance investigation of MPU9250 [89], an unknown slowly drifting bias $\boldsymbol{b_g}$ (instability $\leq 0.0013°/s$) dominates the gyroscope output noise during a long cluster time (800s). In the high-frequency updated estimation algorithm, $\boldsymbol{b_g}$ can be assumed as an unknown constant.

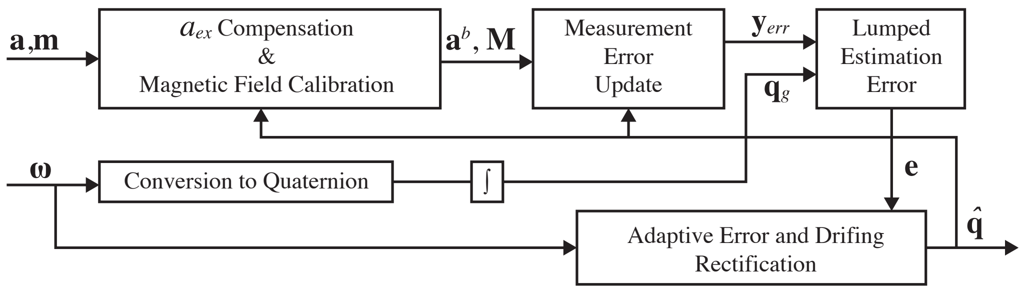

Figure 3.4. : Block diagram of the proposed sensor fusion for FWMAV attitude estimation.

3. Gaussian noises $\boldsymbol{n_g}$ can be filtered.

To enable quaternion calculation. we augment gyroscope measurements as $\{0, \boldsymbol{\omega}\} \in R^4$. The raw attitude estimation based on gyroscope can be expressed by

$$\dot{\boldsymbol{q}}_g = 0.5 \cdot \boldsymbol{q_g} \otimes \{0, \boldsymbol{\omega}\}, \tag{3.9}$$

where $\boldsymbol{q_g}$ is vehicle orientation quaternion and $\otimes$ denotes quaternion multiplication.

The best estimation can be the integration of $\dot{\hat{\boldsymbol{q}}} = 0.5 \cdot \hat{\boldsymbol{q}} \otimes \{0, \bar{\boldsymbol{\omega}}\}$. However, as $\boldsymbol{\omega} \neq \bar{\boldsymbol{\omega}}$ and $\boldsymbol{q_g} \neq \hat{\boldsymbol{q}}$. The accuracy of integration is limited by $\boldsymbol{y_{err}}$ and $\boldsymbol{b_g}$. Consequently, an adaptive observer is designed for $\boldsymbol{y_{err}}$ and $\boldsymbol{b_g}$ compensation.

Introducing $\boldsymbol{E}$ to represent the lumped estimation error in $\hat{\boldsymbol{q}}$, so $\hat{\boldsymbol{q}} = \boldsymbol{q_g} \otimes \boldsymbol{E}$. With force compensation and calibration, $\boldsymbol{E} \approx [1, \boldsymbol{e}]^T$, where $\boldsymbol{e} \in R^3$.

From [93],

$$\dot{\boldsymbol{e}} = 0.5(\bar{\boldsymbol{\omega}} - \boldsymbol{\omega}) + 0.5\boldsymbol{e} \times (\bar{\boldsymbol{\omega}} - \boldsymbol{\omega}) - \boldsymbol{\omega} \times \boldsymbol{e}, \tag{3.10}$$

where $\boldsymbol{e} \times (\bar{\boldsymbol{\omega}} - \boldsymbol{\omega}) \approx \boldsymbol{0}$ since both two terms are very small. Thus,

$$\dot{\boldsymbol{e}} \approx 0.5(\bar{\boldsymbol{\omega}} - \boldsymbol{\omega}) - \boldsymbol{\omega} \times \boldsymbol{e} = -\boldsymbol{\omega} \times \boldsymbol{e} - \boldsymbol{\xi}, \tag{3.11}$$

where $\boldsymbol{\xi}$ represents lumped sensor error of gyroscope raw data.

Solve $\boldsymbol{e}$:

$$\boldsymbol{R(\hat{q}) = R(E)R(q_g) = R(q_g) - 2}[e_\times]\boldsymbol{R(q_g)}, \tag{3.12}$$

where

$$[\boldsymbol{e}_\times] = \begin{bmatrix} 0 & -e_3 & e_2 \\ e_3 & 0 & -e_1 \\ -e_2 & e_1 & 0 \end{bmatrix}, \tag{3.13}$$

based on (3.8),

$$\boldsymbol{y_{err}(q_g, a^b, m)} = \begin{bmatrix} 2[\boldsymbol{R}(\boldsymbol{q_g})\boldsymbol{g}_\times] \\ 2[\boldsymbol{R}(\boldsymbol{q_g})\boldsymbol{M}_\times] \end{bmatrix} \boldsymbol{e}. \tag{3.14}$$

From the derivation above, $\boldsymbol{e}$ can be approximated by using least square approximation presented in [94]. Since accelerometer-magnetometer readings generate an overdetermined sensory system, such an approximated method can minimize the overall estimation errors of every single equation in the calculation.

$\boldsymbol{\xi}$ can be estimated with an adaptive observer:

$$\dot{\hat{\boldsymbol{e}}} = -\boldsymbol{\omega} \times \hat{\boldsymbol{e}} - \hat{\boldsymbol{\xi}} - \boldsymbol{k_1}\boldsymbol{\delta e}, \quad \dot{\hat{\boldsymbol{\xi}}} = \boldsymbol{k_2}\boldsymbol{\delta e}, \tag{3.15}$$

where $\boldsymbol{k_1}$ and $\boldsymbol{k_2}$ are positive defined gain matrices, $\boldsymbol{\delta e}$ and $\boldsymbol{\delta \xi}$ are estimation errors where $\boldsymbol{\delta e} = \hat{\boldsymbol{e}} - \boldsymbol{e}, \quad \boldsymbol{\delta \xi} = \hat{\boldsymbol{\xi}} - \boldsymbol{\xi}$.

The observation is designed to compensate unknown measurement noise, approximation and estimation errors such that (1) all of the measurements and approximations are bounded, and (2) $\boldsymbol{\delta \xi}$ converges asymptotically to $\boldsymbol{0}$.

With the updating, the best estimation of orientation $\hat{\boldsymbol{q}}$ is given by

$$\dot{\hat{\boldsymbol{q}}}_g = 0.5 \cdot \hat{\boldsymbol{q}}_{\boldsymbol{g}} \otimes (\{0, \boldsymbol{\omega} + \hat{\boldsymbol{\xi}}\}), \quad \hat{\boldsymbol{q}} = \hat{\boldsymbol{q}}_{\boldsymbol{g}} \otimes \hat{\boldsymbol{E}}. \tag{3.16}$$

The proposed sensor fusion method can be summarized as a block diagram as shown in Figure 3.4.

The observer stability proof is given below:

As

$$\begin{aligned} \dot{\boldsymbol{\delta e}} &= -\boldsymbol{\omega} \times \boldsymbol{\delta e} - \boldsymbol{\delta \xi} - \boldsymbol{k_1}\boldsymbol{\delta e}, \\ \dot{\boldsymbol{\delta \xi}} &= \boldsymbol{k_2}\boldsymbol{\delta e}. \end{aligned} \tag{3.17}$$

The Lyapunov candidate function can be

$$\boldsymbol{\mathcal{L}} = \frac{1}{2}\|\boldsymbol{\delta e}\|^2 + \frac{1}{2k_2}\|\boldsymbol{\delta \xi}\|^2, \tag{3.18}$$

where $\boldsymbol{\mathcal{L}}$ is a smooth, positive definite, and radially unbounded function [95]. The derivative of $\boldsymbol{\mathcal{L}}$ yields

$$\begin{aligned}\dot{\boldsymbol{\mathcal{L}}} &= (\boldsymbol{\delta e})^T(-\boldsymbol{\omega}\otimes\boldsymbol{\delta e}-\boldsymbol{\delta\xi}-k_1\boldsymbol{\delta e})+\frac{1}{k_2}(\boldsymbol{\delta\xi})^T(k_2\boldsymbol{\delta e}),\\ &= 0-(\boldsymbol{\delta e})^{\boldsymbol{T}}\boldsymbol{\delta\xi}-k_1|\boldsymbol{\delta e}|^{\boldsymbol{2}}+(\boldsymbol{\delta\xi})^{\boldsymbol{T}}\boldsymbol{\delta e},\\ &= -k_1|\boldsymbol{\delta e}|^2\leq 0.\end{aligned}\tag{3.19}$$

Here $\boldsymbol{\mathcal{L}}$ is negative semi-definite, which guarantees the global stability of the observer. Furthermore, for global asymptotic stability proof, it needs more arguments.

Given $0\leq\boldsymbol{\mathcal{L}}$, thus the upper bound of $\dot{\boldsymbol{\mathcal{L}}}$ is determined by its initial value $\boldsymbol{\mathcal{L}}_0$. Because $\boldsymbol{\mathcal{L}}$ is a radially unbounded function in terms of $\boldsymbol{\delta e}$ and $\boldsymbol{\delta\xi}$, $\boldsymbol{\delta e}$ and $\boldsymbol{\delta\xi}$ are bounded. Since the gyroscope measurement w is bounded as well due to the characteristic of sensor, all terms on the right side of (3.17) are bounded. It can conduct $\boldsymbol{\delta e}$ and $\boldsymbol{\delta\xi}$ are continuous and moreover, $\boldsymbol{\delta\dot{e}}$ and $\boldsymbol{\delta\dot{\xi}}$ are bounded, which yields $\boldsymbol{\delta e}$ and $\boldsymbol{\xi}$ are uniformly continuous.

Thus, for any $t\geq 0$, we have

$$\sqrt{\int_0^t|\boldsymbol{\delta e}(\tau)|^2d\tau}\leq\sqrt{\frac{\boldsymbol{\mathcal{L}}_0}{k_1}},\quad \boldsymbol{\delta e}\in L^2.\tag{3.20}$$

From Barbalat's lemma [95] and boundedness of $\boldsymbol{\omega}$, $\boldsymbol{\delta e}$ and $\boldsymbol{\delta\dot{\xi}}$ are globally asymptotically stable at the origin.

Since $\boldsymbol{\omega}$ and $\boldsymbol{e}$ satisfy the persistent excitation criteria [95], based on Lemma A.1 as presented in [96], the globally asymptotically stability for $\boldsymbol{\delta\xi}$ can be proved.

3.3 Experimental Result and Discussion

The indoor experiment setup is shown in Figure 3.5. During the test, the proposed hummingbird robot is flying in a VICON space. Totally 6 VICON cameras are in use. VICON captured information is received by a desktop computer via VICON Tracker 1.0.3 software at 200Hz. The transmission delay is about 0.03s. A NI myRIO is used to relay the position feedback and log data. The onboard circuit is powered an external power supply through tethers. The proposed sensor fusion and flight control algorithms are running onboard. The onboard IMU communicates with onboard microcontroller through I2C bus protocol. In this specific test, VICON also provides ground truth.

Note, in this thesis, most of the indoor flight test uses this setup.

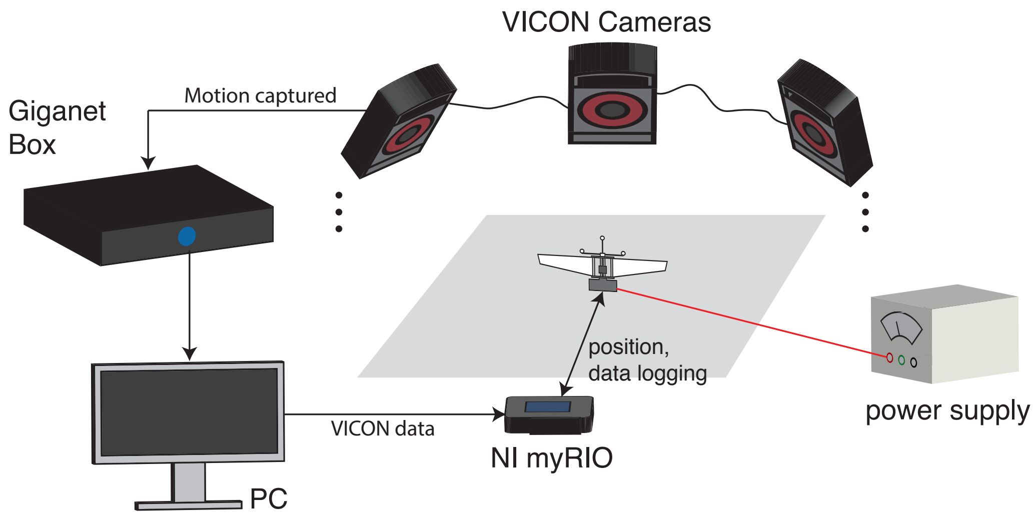

Figure 3.5. : Illustration of flight test setup in VICON space.

Before we achieve the controlled free flight, to tune the sensor fusion algorithm, we conducted several flight trials with wire constraints on the landing gear of the robot to aid the attitude stability, generating a near-hover flight condition. Tightening and relaxation of the wires can be considered a low-frequency external disturbance. Maneuvering tests were also conducted by manually adjusting the tightness of wires or short-time free flight. We compared the proposed sensor fusion solution with two state-of-the-art algorithms: Extended Kalman Filter and Madgwick Filter. We tuned their sensor fusion gains to achieve their overall best performance respectively. As shown in Table 3.1, without a particular concern of FWMAVs' specific properties, traditional methods cannot perform adequately sensing results. We also applied a_{ex}

compensation onto two comparison methods, both of their performance becomes better but only marginally, as shown in Figure 3.6.(c).

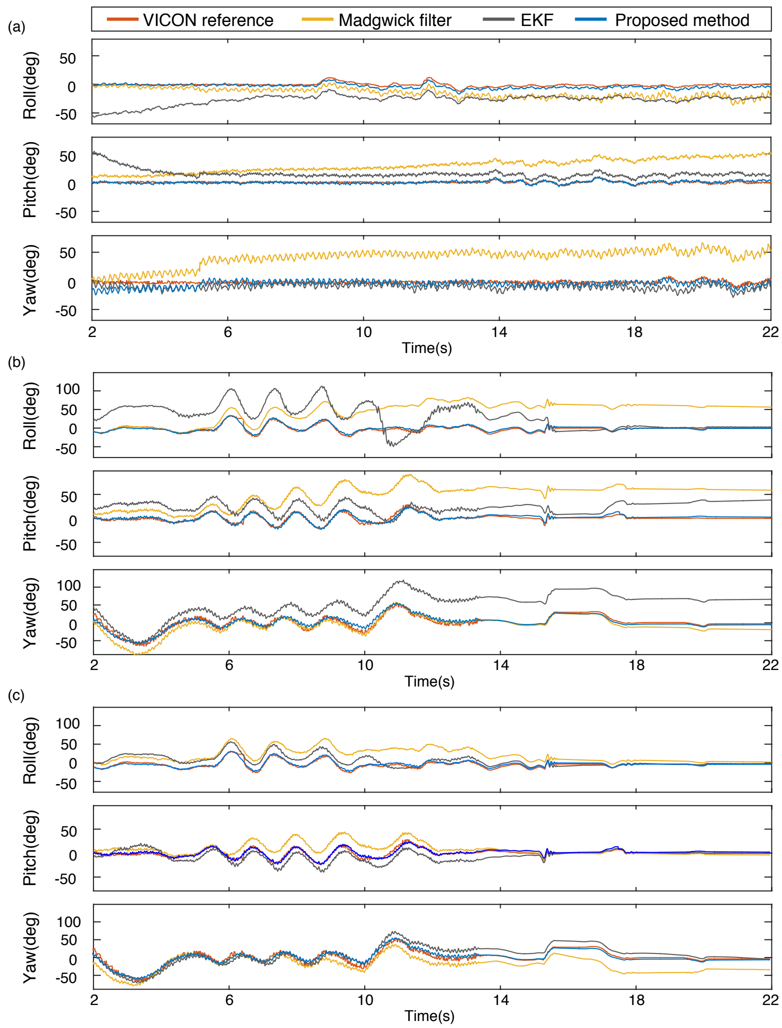

Figure 3.6. : (a). Attitude estimation in hovering (constraint condition). (b). Attitude estimation in maneuvering (constraint condition). (c). Euler angle estimation in maneuvering with aerodynamic force compensated acceleration for Madgwick filter and EKF. The accuracy of both was improved. Nevertheless, they still failed to converge to the ground truth before wings stopped (around 14s).

From Figure 3.6.(a,b), during the initial test, the idea attitude set-point is around zero. Due to the severe acceleration induced by wings, the EKF and Madgwick filter

Table 3.1. : RMSE Comparison of Tested Sensor Fusion Algorithms

		Proposed	Madgwick	EKF
Hovering test	roll	**2.2161°**	30.1043°	17.4910°
	pitch	**2.0454°**	37.2643°	28.8441°
	yaw	**2.8318°**	37.0175°	11.6472°
Maneuvering test	roll	**2.2320°**	28.7868°	24.6769°
	pitch	**2.0262°**	35.4507°	24.7713°
	yaw	**3.6863°**	17.5361°	29.7953°
Maneuvering test with a_{ex} compensation	roll	**2.2320°**	17.9809°	10.8939°
	pitch	**2.0262°**	12.3591°	9.8938°
	yaw	**3.6863°**	19.3879°	17.4390°

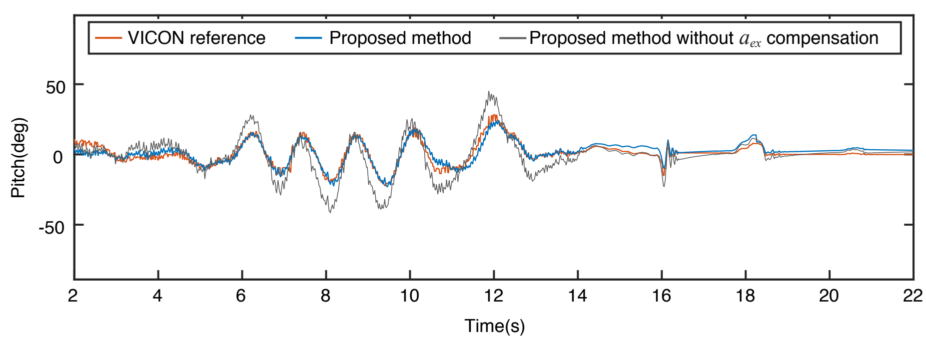

Figure 3.7. : Pitch angle estimation in maneuvering condition with/without a_{ex} compensation for the proposed method. Without aerodynamic force compensation, pitch angle cannot be estimated correctly.

are failed to obtain correct attitude information. As shown in Figure 3.6, Madgwick filter is hard to overcome the trade-off between chattering results from higher complementary gain and drifting results from smaller complementary gain. EKF shows obvious sensing error and its convergence speed is slow. Such a slow, drifting response

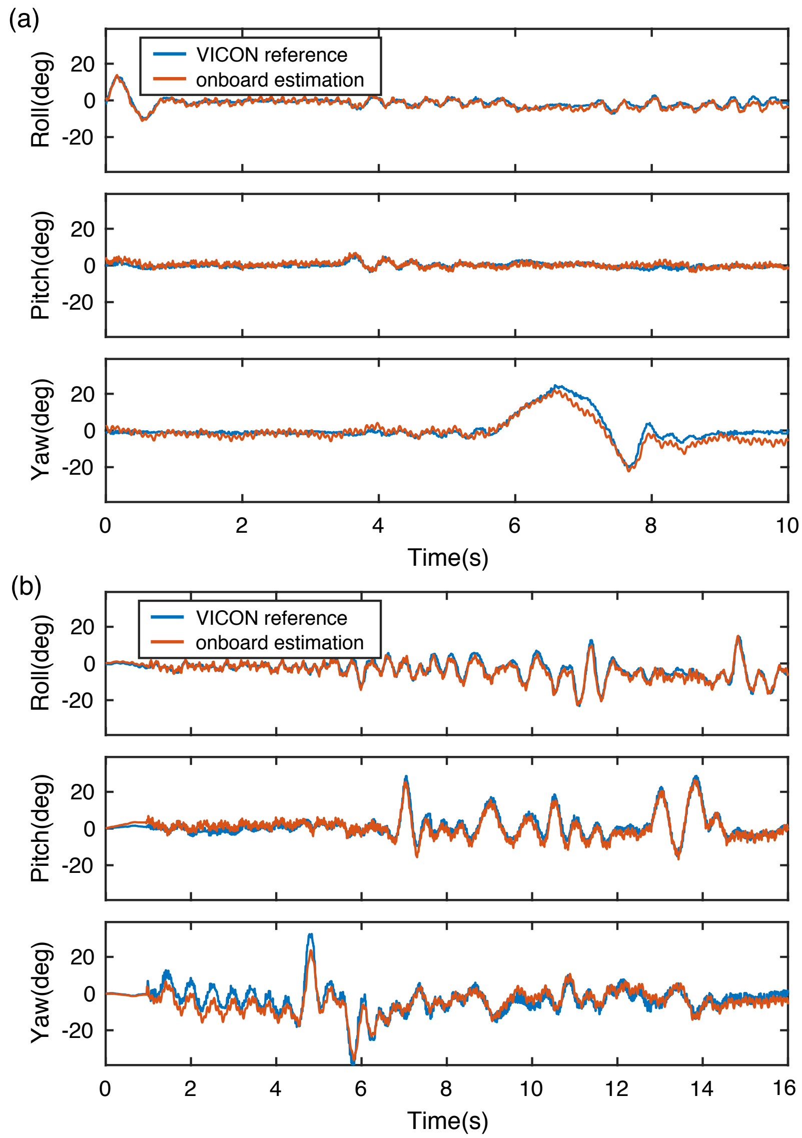

Figure 3.8. : Two free flight test, the proposed sensor fusion working together with flight control. (a). Attitude estimation in hovering. (b). Attitude estimation in maneuvering. Both scenarios show great estimation accuracy.

will affect onboard feedback control significantly. Both of them can hardly reject the sensing error under such severe vibration. In contrast, the accuracy of the proposed method was not impacted by such a huge vibration.

From Table.3.1, along wing stroke direction, i.e., pitch axis, sensing result becomes even worse for EKF and Madgwick filter, which indicates the significance of model-based compensation. As shown in Figure 3.7, even for the proposed method, without $\boldsymbol{a_{ex}}$ compensation, error $\boldsymbol{E}$ cannot be fully rectified as well, especially during aggressive maneuvering. Thus, we then implemented the model-based compensation design to feed compensated acceleration information onto both Madgwick filter and EKF for comparison. Their accuracy improvement in pitch angle sensing can be observed on RMSE. However, the introduced approximation error within the compensation step affects their roll and yaw angle estimation. To address it, the proposed sensor fusion design employs an adaptive updating law to correct the lumped sensing error, covering sensor drift and model error.

We then test the effectiveness of the proposed sensor fusion working together with onboard flight control. We detail the controller design in Chapter 4. Here, we implemented the proposed controller to guarantee flight stability and then retested the sensor fusion performance in two typical free flight scenarios. The results of both flight samples show the convergence and accuracy of the proposed method. Compared to the preliminary test, it illustrates that the effectiveness of the proposed sensor fusion does in free flight. It has been used in untethered flight as well, as presented in Chapter 6.

3.4 Conclusion

On FWMAVs, many existing onboard sensor fusion methods exhibit performance degradation in terms of accuracy, robustness, and convergence in attitude sensing, which is mainly due to their flapping wing induced severe oscillations. To address this open issue, in this work, a model-based sensor fusion approach is proposed for the onboard real-time attitude sensing of FWMAVs by using MEMS-based IMU sensor. The sensing performance of the proposed method has been validated experimentally.

From the experimental result, such an approach demonstrates accurate and robust performance. The proposed method can be used for closed-loop feedback control.

4. ONBOARD FLIGHT CONTROL

Relying on their sophisticated sensory-motor systems, insects and hummingbirds are among the most nimble flying animals. They have mastered the flight capability through millions of years of adaptation, which can be treated as a long-term optimization strategy of their flight control mechanism. In order to match the flight performance on similar scale FWMAVs, a well-designed control law is required. We propose a novel hybrid control (in terms of combining conventional with learning-based control) strategy. We first design a model-based nonlinear control law to achieve stable hovering and waypoint tracking. A motion control policy is then trained to perform aggressive maneuvers through Reinforcement Learning (RL). These two sets of control logic can complement each other perfectly. In normal stable flight, model-based control is pursuing stability and robustness over a large region of attraction. The trained model-free policy is specifically designed to push the boundary of the flight envelope to enable the extreme maneuvers that model-based control is hard to handle, such as flip upside down (control efforts contradict to vehicle stabilization goal). In this chapter, we first present our model-based control law design. Several flight tests were conducted to demonstrate its performance, including hovering and waypoint tracking. Based upon it, we then challenge animal-like tight flip maneuver relying on RL. We demonstrate a nearly drift-free rapid 360° body flip on our bio-inspired hummingbird robot. Such a result indicates that although bio-inspired robots cannot fully replicate the elaborate actuation in animals, through a combined method of machine learning and conventional controls, they can achieve flight performance that closely resembles their natural counterparts with the help of learning.

4.1 Introduction

Through millions of years of natural selection, insects and hummingbirds have evolved with superior flight capabilities. Their ability to perform acrobatic maneuvers in indoor or confined spaces showed great potential and attracted great interest from the robotics community to develop bio-inspired Flapping Wing Micro Aerial Vehicles (FWMAVs). As a result, the development of such biomimetic flying platforms has witnessed remarkable progress over the past decade as we introduced in Chapter 1. Nevertheless, to match the flight performance of their natural counterparts, there remain many open issues that need to be addressed. Particularly, flight control of such vehicles is a great challenge. The difficulties are mainly from their highly nonlinear system dynamics, complex time-varying aerodynamics, severe body oscillation, limited actuator performance, and manufacturing imperfections, to name but a few. These system uncertainties affect system robustness significantly and challenge the control law design. We first deal with the uncertainty from manufacturing imperfections that cause the trim condition. To deal it and avoid repeated manually trimming, we propose to use motor torque feedback to estimate and rectify the lumped system asymmetries. Furthermore, we address unsteady aerodynamics and nonlinearity caused control issues. Based on the control authority study and averaging theory [17, 72], we design a robust control law to generate stable altitude control and thrust generation, which allows a linear attitude and lateral control. Such a design aims to save onboard computational resources while maintaining flight performance. Hovering and waypoint tracking tests were performed to evaluate the overall performance of the proposed control algorithm with unknown trim conditions. The result demonstrates that even with only two actuators, such a bio-inspired hummingbird robot can still track full 6-DoF perfectly by modulating its decoupled flapping wings.

The proposed nonlinear controllers provide an effective solution for stable flight. However, it is not enough to challenge high-performance maneuvers observed in animals. To address acrobatic maneuvers, conventional flight controls rely on preplanned trajectories and model-based flight control algorithms. However, flapping flight is highly nonlinear, coupled dynamics which is further complicated by its unique inherent dynamic mechanisms such as FCF and FCT [54], and the rapidly changing, unsteady aerodynamics. As a result, flight dynamics vary significantly under different flight modes and many remain unknown besides hovering dynamics. Therefore, the conventional planned method is hard to be directly applied to FWMAVs. Most importantly, during certain maneuvers such as back or side flips, the maneuvering control authorities can contradict to vehicle stabilization goal. For example, body flips remain significant challenges since such maneuver contradicts the normal flight control system, i.e., the vehicle is unstable when turned upside-down.

On the other hand, natural selection can be viewed as a long-term training and optimization process for biological systems. For example, Flies can perform nearly drift-free backflips within a minimum footprint (translational drift). Thus, we propose to incorporate machine learning to facilitate flight control performance in maneuvering. In particular, besides the stable and robust hovering, we integrate a reinforcement learning control policy to enable tight flips on our hummingbird robot. A proposed stable control law works as a baseline control for stabilization purposes. Reinforcement learning is used here to enable the aggressive maneuvers of the robot instead of a traditional trajectory planning algorithm. This design can work with instantaneous uncontrollable scenarios. The process from low-level actuation commands to the vehicle states can be modeled as a Markov Decision Process (MDP). Thus, the optimal maneuver policy can be searched in the learning process. This design choice is made because the averaged dynamics model of the system for stabilization is relatively accurate, while for extreme maneuvers the approximation error becomes unmanageable for model-based controller design [17]. Particularly, in drift-less body flip maneuver, a model-free maneuver policy is trained by using Deep Deterministic Policy Gradients (DDPG) to take over the flip motion control when the stable controller is infeasible, e.g., flying upside-down. Our goal is to find out if machine learning can aid bio-inspired flying robots to cope with model uncertainty, varying dynamics, and demanding performance even under severely underactuated systems. The test result shows that although bio-inspired robots cannot replicate the elaborate actuation in animals, through a combined method of machine learning and conventional controls, they can achieve flight performance that closely resembles their natural counterparts.

4.2 Model-based Control

4.2.1 System Trimming

Unlike conventional aerial vehicles, the aerodynamic force and torque generation of the flapping wing robots are very sensitive to any slight fabrication asymmetries, which affects system passive stability significantly as shown in Figure 4.1. Since such system imperfection cannot be completely eliminated in fabrication as discussed in Chapter 2, it motivates the trim conditioning work to generate a default asymmetric control effort on the two wings to compensate for the inherent asymmetry of the system.

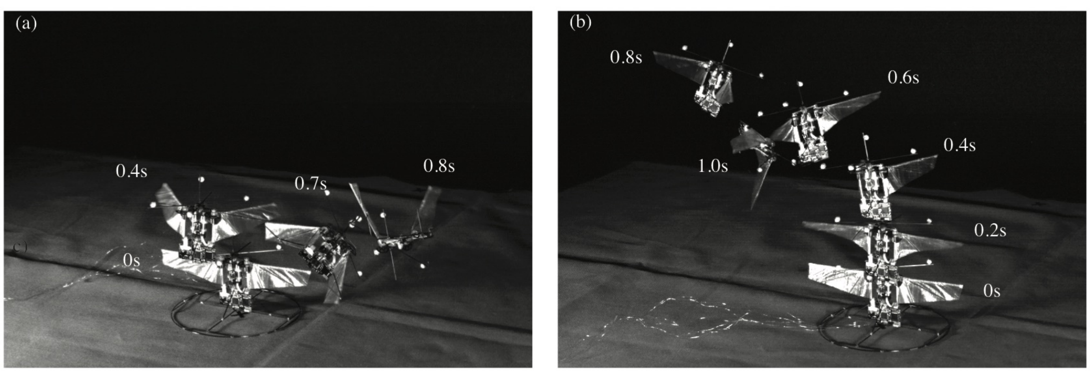

Figure 4.1. : Two examples of open-loop liftoff. (a). Liftoff with only a constant thrust command. (b). Liftoff with balanced trim condition.

In order to avoid the repeated manually trim tuning [29, 33, 40, 41], we present a new method to quantify trim condition based on motor torque feedback. Since the angle of attack of our wings are fixed at 45^o, the production of the aerodynamic force and drag becomes a function of the angular speed of the wing motion ($\dot{\phi}_w$) [7], which can be fully sensed by the motor torque asymmetry based on the motor current feedback as shown in equation 2.7. Therefore, with the current feedback of the two motors, the trimming process can be converted to a power balance problem. For example, Figure 4.2 shows the current feedback of the two motors in hover with the nominal power input - 10V/0.5A. Based on this, we can conduct the trim condition as below:

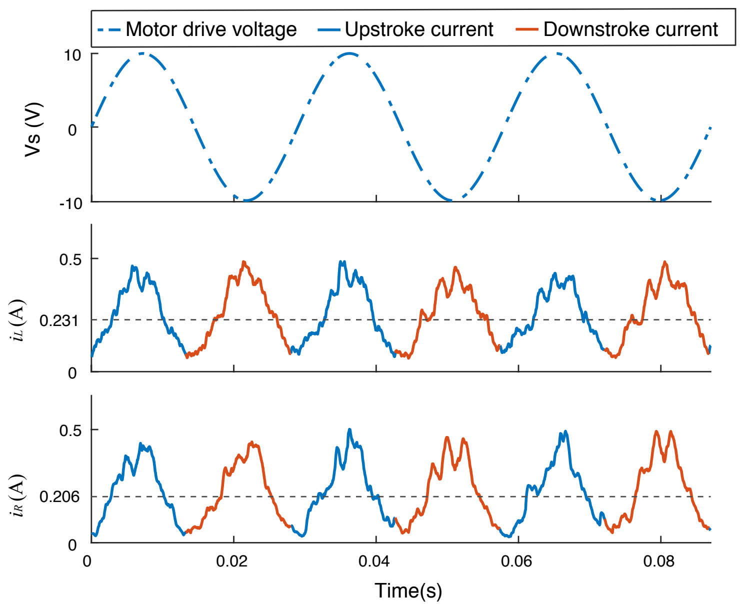

Figure 4.2. : Motor current feedback for the estimation of system trim condition.

1. The mean current difference between the left and right side wings are 0.025A. According to the nominal current, it stands about 5% aerodynamic force discrepancy during flight and must cause an undesired roll-axis rotation. From the force mapping, since motor excitation is proportional to the $\dot{\phi}_w^2$, 5% aerodynamic force discrepancy requires $(1.05^2 - 1) \times 10V \approx 1V$ to balance the roll torque offset.

2. The left and right wings have -0.003A and -0.002A average excitation bias respectively and two wings have overall -0.001A average offset between upstroke and downstroke. These indicate the pitch and yaw trims are fairly small.

4.2.2 Control Law Design

From Chapter 2.3, the control inputs of the system is given by

$$
\begin{aligned}
f_z &= F_0 v_1^2, \\
\boldsymbol{\tau} &= \begin{bmatrix} r_{cp} F_0 v_1 v_2 \\ r_{cp} F_0 v_1^2 v_3 \\ r_{cp} F_0 v_1^2 u_4 \end{bmatrix},
\end{aligned} \tag{4.1}
$$

where $F_0 = \frac{1}{2}\rho_a \bar{C}_L R_w^3 \bar{c} \hat{r}_2^2(S)\omega_w^2 A_0^2 = mg$ is the nominal lift force to counter the gravitational force of the robot. Obviously, the thrust term dominates the robot control as it impacts all control torques generation. It means any slight altitude drift could affect attitude stability simultaneously. Therefore, f_z plays an important role in FWMAVs control, namely, robust altitude tracking aids the whole system stability significantly.

To achieve fast reaction and guarantee transient control performance, a deterministic robust control law (DRC) is designed to generate proper thrust for altitude control.

For our hummingbird robot, altitude dynamics is

$$m\ddot{z} = -mg + cos\phi cos\theta f_z + d_z, \tag{4.2}$$

where d_z represents the lumped system uncertainty from modeling errors and external disturbances.

Given a reference input z_d, we define a sliding surface

$$s_z = \dot{e}_z + k_s e_z = \dot{z} - \dot{z_{eq}}, \tag{4.3}$$

where $e_z = z - z_d$ is the tracking error, k_s is a positive gain and z_{eq} is the equivalent tracking error which can be derived trivially.

As shown in Figure 2.6, with the input voltage growing, the thrust increase can be approximated with a linear fitting

$$f_z = k_u(u_z - u_{z_0}), \tag{4.4}$$

where k_f is a positive slope, u_z is voltage input, and u_{z_0} is a constant term.

Rewrite system dynamics along z-axis as:

$$m\dot{s}_z = K_z u_z + \boldsymbol{\varphi}_z^T \boldsymbol{\Theta}_z + \Delta_z, \tag{4.5}$$

where

$$\begin{cases} K_z = K_u cos\phi cos\theta, \\ \boldsymbol{\varphi}_z^T = [-K_z u_{z_0}, -(g + \ddot{z}_{eq}), 1], \\ \boldsymbol{\Theta}_z = [1, m, \tilde{d}_z]^T. \end{cases} \tag{4.6}$$

Here $\Delta_z = d_z - \tilde{d}_z$, wherein $\tilde{d}_z$ denotes the estimated lumped modeling error that may vary slowly.

Assuming the parameters and uncertainty are bounded:

$$\begin{aligned} &\boldsymbol{\Theta}_z \in \Omega_{\boldsymbol{\Theta}_z} \triangleq \{\boldsymbol{\Theta}_z : \boldsymbol{\Theta}_{min} \leq \boldsymbol{\Theta}_z \leq \boldsymbol{\Theta}_{max}\}, \\ &\Delta_z \in \Omega_{\Delta_z} \triangleq \{\Delta_z : |\Delta_z| \leq \delta_z\}. \end{aligned} \tag{4.7}$$

where $\boldsymbol{\Theta}_{min} = [1, 12, -0.5]$ and $\boldsymbol{\Theta}_{max} = [1, 12, 0.5]$. It means that it can handle ± 0.5 gram modeling error in total mass weighing. We set $\delta_z = 1$ then control model can tolerate 1 gram estimation error. Note, this setup does not affect the flight performance, control efforts in other axes are still sufficient as normal, as shown in Figure 2.6.

As $\Omega_{\boldsymbol{\Theta}_z}$ and Ω_{Δ_z} are known, a control law is designed by

$$K_z u_z = u_{z_m} + u_{z_l} + u_{z_r}, \tag{4.8}$$

where $u_{z_m} = -\boldsymbol{\varphi}_z^T \hat{\boldsymbol{\Theta}}_z$ is model-based compensation terms and $u_{z_l} = -k_{z_l} s_z$ is the linear stabilizing terms, wherein $\hat{\boldsymbol{\Theta}}_z$ is the reference model from system identification and k_{z_l} is a positive gain.

With the control law defined in equation 4.8, the error dynamics becomes

$$m\dot{s}_z + k_{z_l} s_z = u_{z_r} - \boldsymbol{\varphi}_z^T \tilde{\boldsymbol{\Theta}}_z + \Delta_z, \tag{4.9}$$

Thus, the robust control input u_{z_r} should be designed such that

$$\begin{cases} s_z(u_{z_r} - \boldsymbol{\varphi}_z^T \tilde{\boldsymbol{\Theta}}_z + \Delta_z) \leq \varepsilon_z, \\ s_z u_{z_r} \leq 0, \end{cases} \tag{4.10}$$

where ε_z is a designed parameter that represents the approximation accuracy between the ideal sliding mode control law and the proposed method. ε_z should be positive and sufficiently small.

To satisfy all of the above conditions, referenced from [92], one example of u_{z_r} design is given by

$$u_{zr} = -\frac{1}{4\varepsilon_z}[||\boldsymbol{\Theta}_{z_{max}} - \boldsymbol{\Theta}_{z_{min}}||^2 ||\boldsymbol{\varphi}_z||^2 + ||\delta_z||^2] s_z, \tag{4.11}$$

The stability proof of this design is similar to [92] with different input. Such a robust controller guarantees the transient and steady state tracking performance. The upper bound of tracking error e is: $\exp(-k_e t)[|e(0)|^2 - |e(\infty)|^2] + |e(\infty)|^2$ wherein $|e(\infty)|^2 \leq \frac{2\varepsilon_z}{k_e}$, $k_e = 2k_{z_l}/m$.

As discussed before, with robust altitude control, lateral and attitude control of our hummingbird robot become similar to drone control except for the FCF and FCT induced damping disturbances. Particularly, on our platform, the x-y position is controlled by a proportional controller that generates velocity control reference, where the velocity is controlled by a PID controller in inner-loop to generate roll and pitch angle control references. The attitude is also constructed as a cascading form where the outer loop is a proportional controller mapping angle error to angular velocity references and relying on the inner-loop PID controller generating torque command. Combing with the wing kinematics control, eventually, torque command are converted to motor signal that powers the vehicle.

Note, the proposed DRC+PID control law only guarantees the vehicle stability in stable flight condition. To challenge extreme maneuvers, the advanced control method is required.

4.3 RL-enabled Acrobatic Maneuvering

A learned policy is used to take over the model-based control when it is infeasible, e.g., flying upside down. The framework structure is shown in Figure 4.3. An RL policy training is performed in a high fidelity simulation tool that is developed with full system dynamics including flapping flight aerodynamics, wing-actuation thorax dynamics, and vehicle body dynamics [97]. In order to transfer to the real robot platform, the sensing error, communication delay, and arbitrary noise are also introduced in the simulator to emulate the real flight condition. In the simulation, all physical parameters and signal characteristics came from system identification of the real hummingbird robot.

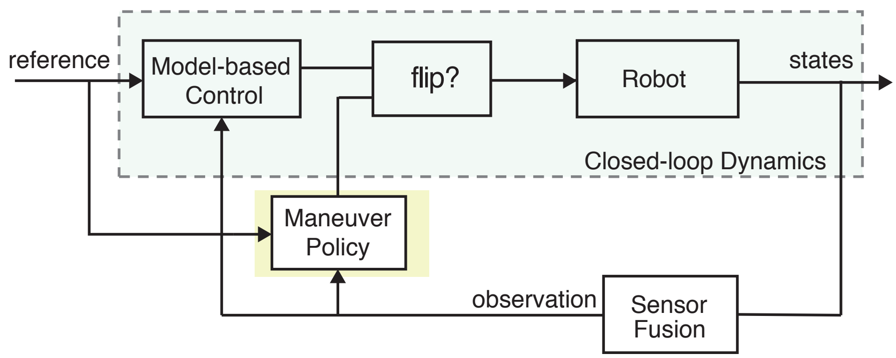

Figure 4.3. : Illustration of the hybrid controller structure. If the flip maneuver was triggered, RL policy takeover the original controller.

4.3.1 Problem Formulation

Reinforcement learning is a specific area of machine learning. The key mechanism in RL is performing optimal actions to maximize a certain reward. In a typical RL problem setup, there is an agent that keeps interacting with an environment. This interaction can be formulated as a MDP, which consists of environment state space $\mathcal{S}$, action space $\mathcal{A}$, state transition model $p(s_{t+1}|s_t, a_t)$, reward model $r(s_t, a_t)$, and discount factor γ, wherein t represents time step. An agent policy function $\pi : \mathcal{S} \to \mathcal{A}$

is accordingly defined to take the current environment state and return an action. π is a policy network $\pi_\theta(a_t|s_t)$ which is parameterized by θ.

The agent starts from an initial state distribution $p(s_1)$. At each time step, the environment state changes according to the agent's action. Meanwhile, agent action results in a reward/penalty response from the environment. The goal of the learning process is to obtain the optimal policy parameter θ, i.e. how actions affect the state, such that it can maximize the cumulative rewards.

The expected discounted return of a finite-horizon RL problem is

$$J = \mathbf{E}_{a_i \sim \pi_\theta}[\mathcal{R}] = \mathbf{E}_{a_i \sim \pi_\theta} \sum_{i=0}^{T} \gamma^{i-1} r(s_i, a_i), \tag{4.12}$$

where T is the horizon, i is the discrete step and γ is the discount factor.

In this study, each component is defined as follows:

1. Agent: the hummingbird robot.
2. Environment: a constraint 'world' defined in simulation.
3. States $s = [\hat{i}, \hat{j}, \hat{k}, x, y, z, p, q, r, \dot{x}, \dot{y}, \dot{z}]^T] \in \mathcal{S}$. All terms are defined in Chapter 2.
4. Action: the additional control commands, wherein action $a = [u, \delta V, V_0, \delta\sigma] \in \mathcal{A}$. All terms are defined in Chapter 2.
5. State transition dynamics: closed-loop vehicle dynamics, where the feedback controller is described above.
6. Reward function: a customized function to incentivize robot to perform certain maneuvers.

4.3.2 Reward Design

To perform the flip maneuver, the robot hovers at $\mathbf{p}_0 = [0, 0, 0.5]^T$. When a trigger signal is given, the robot initiates a 360° turn and then stabilize at $\mathbf{p}_0$ again.

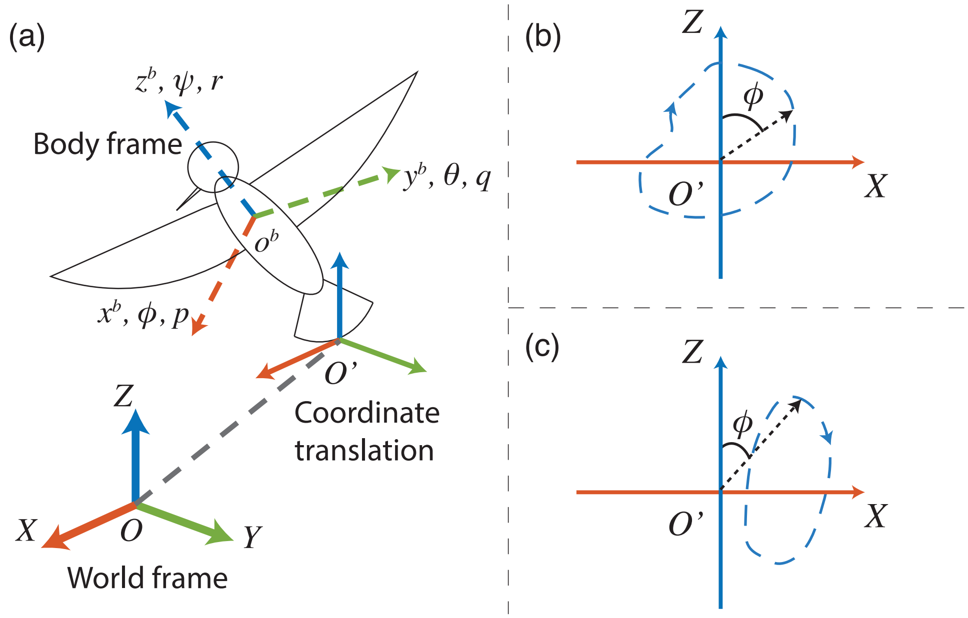

Figure 4.4. : (a). Coordinate define and translation. (b). A successful flip over along Y-axis. (c). A failed flip over along Y-axis.

As shown in Figure 4.4, a successful front/back rollover can be described by the flight trajectory projection crossing all four quadrants of $ZO'Y$. Side flip is the same. The coordinate system attached to the tail of the vehicle is translated from the world frame. With the rigid body assumption, such a coordinate translation will not affect the maneuver definition, which can be proved trivially through 3D coordinate transformation.

Since a successful flip maneuver can be defined clearly, designing the reward function is straightforward. Considering the entire flip process, a complete flip maneuver can be intuitively split into two steps: first, tilting upside down, then, turning back to the head-up state. Therefore, we propose a 'carrot-and-stick' design to describe the whole process: the first 'carrot' is set to the bottom of the robot; after the robot flips 180° vertically and successfully reached the first 'carrot', the second 'carrot' appears at the robot's original head area to lead the robot to turn back. In order to get the reward in the second stage, at the end of the first stage, the vehicle will learn to maintain a certain rotational speed to avoid the failed case as described by Figure 4.4.(c).

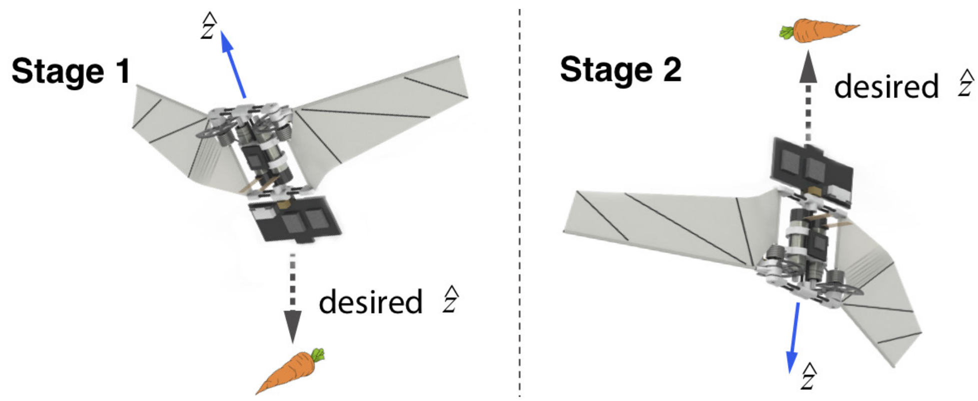

Figure 4.5. : Illustration of reward model design.

During the first step, a well-designed reward model should incentivize the robot to perform an upside-down motion. Mathematically, the reward should increase significantly when the body z-axis projection in the inertia frame $\hat{z} = \hat{k} \cdot \hat{K}$ was approaching to -1, which represents the robot heading downwards. So the reward model on the first half stage of flip motion is designed as $r_1 = K_1/[1 + (1 + \hat{z})^2]$, wherein K_1 is a positive gain. Once the robot finished the upside-down step, the reward function will move on to award the $\hat{z}$ approaching 1. Thus, the second term of our reward model is defined oppositely to r_1, which is $\bar{r}_2 = K_2/[1 + (1 - \hat{z})^2]$. Like r_1, K_2 is a positive gain as well. Such a 'carrot-and-stick' configuration successfully guides a basic flip maneuver.

Besides flip maneuver, the above setup may generate some undesirable behavior. For example, the robot will learn to oscillate at very large amplitude to collect more cumulative reward. To filter out these undesirable behaviors, a linear growing stability reward r_s and a position tracking reward $r_p = K_{\mathbf{p}}||\mathbf{e_p}|| + K_{\mathbf{v}}||\mathbf{v}||$ have also been added to r_2 to further promote a flip-drift-recovery process, where $K_{\mathbf{p}}$ and $K_{\mathbf{v}}$ are positive gains. r_s leads the robot to perform flip as quick as possible for gaining more cumulative reward. Meanwhile, these additional terms prevent large positional drift, assisting the model-based control when the robot turns back to normal flight. The lumped $r_2 = \bar{r_2} + r_s + r_p$.

The total reward is given by

$$r_t = (1 - \lambda)r_1 + \lambda r_2 \tag{4.13}$$

where λ is a binary flag to indicate whether robot is in the first or second stage in the flip maneuver.

In order to achieve animal-like performance where the available space for flipping is tuned to be tightly constrained. Eventually, we only allow one wingspan length of translational drift in all X-Y-Z direction. During the training, if the robot travels out of bounds, the current rollout will be terminated to cut the cumulative reward, thus penalizing the corresponding action. By maximizing the reward, the policy will learn to minimize the vehicle's position drift.

4.3.3 Training

In our design, both state transition model and reward model are deterministic functions. Therefore, a Deep Deterministic Policy Gradients (DDPG) is chosen as our training algorithm due to its robust performance on such robot platforms with continuous action spaces [98]. DDPG is an off-policy algorithm constructed with actor-critic architecture that updates a policy function (actor) and an action-value function (critic) by batch sampling from a replay pool of tuples (s_t, a_t, r_t, s_{t+1}) [98]. The function approximators are fully connected multilayer perceptrons.

The actor and critic network are configured with 32×32 and 64×64 hidden units respectively. Hidden and output activation functions in both networks are hyperbolic tangent (tanh) function. The simulation is solving the physics at 10kHz. Considering the consistency between real and simulated flight control of the robot, the control frequency is downsampled to 500Hz which is same as the onboard control. The horizon of each rollout has a maximum of 1000 samples which corresponds to 2 seconds. Each epoch is set to a maximum of 10000 samples, i.e., $\leq$ 20 seconds (10 rollouts) at least. The algorithm implementation is based on [99] with hyperparameters from [98].

In order to acquire a sim-to-real portable solution, we use dynamic randomization approach in the training process [100]. Randomness was injected into the physical parameters of the vehicle, such as mass/inertia, actuator parameters, mechanical configurations, and sensing noise to imitate the modeling error of the system.

During the training process, the termination condition is set to stop an episode early to improve the training efficiency and prevent the useless action state appeared in the replay pool. By setting termination conditions, we intend to penalize the meaningless behavior with a huge position drift or fully destabilized flight. Successful maneuvers wherein the robot resumes to a hovering flight will keep collecting positive rewards and maximizing the total return.

4.4 Experimental Result and Discussion

We conducted a couple of flight tests to evaluate the performance of the proposed model-based controller and RL maneuver policy on our hummingbird robot. During the test, a VICON system is used to provide position feedback.

4.4.1 Stable Flight: Hovering and Waypoint Tracking

To validate the performance of the proposed controller, we first performed hover flight tests on our hummingbird robot. During the test, the altitude reference is prescribed. To avoid unrealizable ascending and descending velocity, a first-order filter is used to generate a smooth reference trajectory z_d. X-Y, and attitude control reference are set at zero. A typical flight result is shown in Fig. 4.6. The vehicle is commanded to takeoff and hover at $0.4m$. The tracking error is small enough to enable a stable hovering in sustained performance.

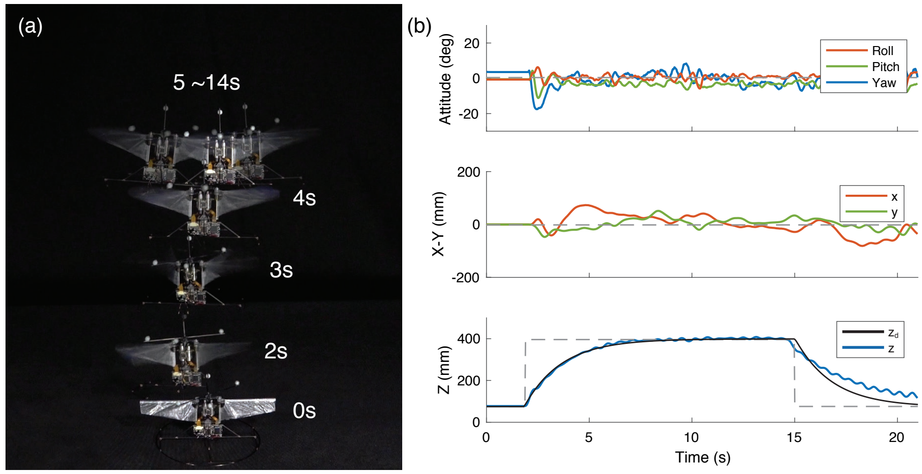

Figure 4.6. : (a). Time sequential result of a typical takeoff, hovering, and landing flight. Composed image only show takeoff and hovering. (b). Attitude and position of the robot in the test. Gray dash lines represent control references.

In addition, we also performed waypoint tracking flight tests. During the test, a single set point is specified and the reference trajectory is generated by a first-order filter as well. The results is shown in Fig.4.7.

From the experimental result, the proposed model-based controller successfully stabilizes the flapping wing robot in all flight tests and demonstrates great tracking performance. Based on such a design, we train our hummingbird robot to achieve aggressive maneuver control.

4.4.2 Extreme Maneuver: Drift-free Flip

The trained flip maneuver of our hummingbird robot converges to the side flip motion, which is a bit out of our expectation since the front/back flip is more observed on the animals. Theoretically, the front/back flip is easier for flapping wing platform due to FCF and FCT effect. Perhaps due to the larger torque generation along the roll axis, the manifested flip maneuver trends to side direction. The work presented in [35] demonstrates a similar motion using the traditional planning method. Compared to

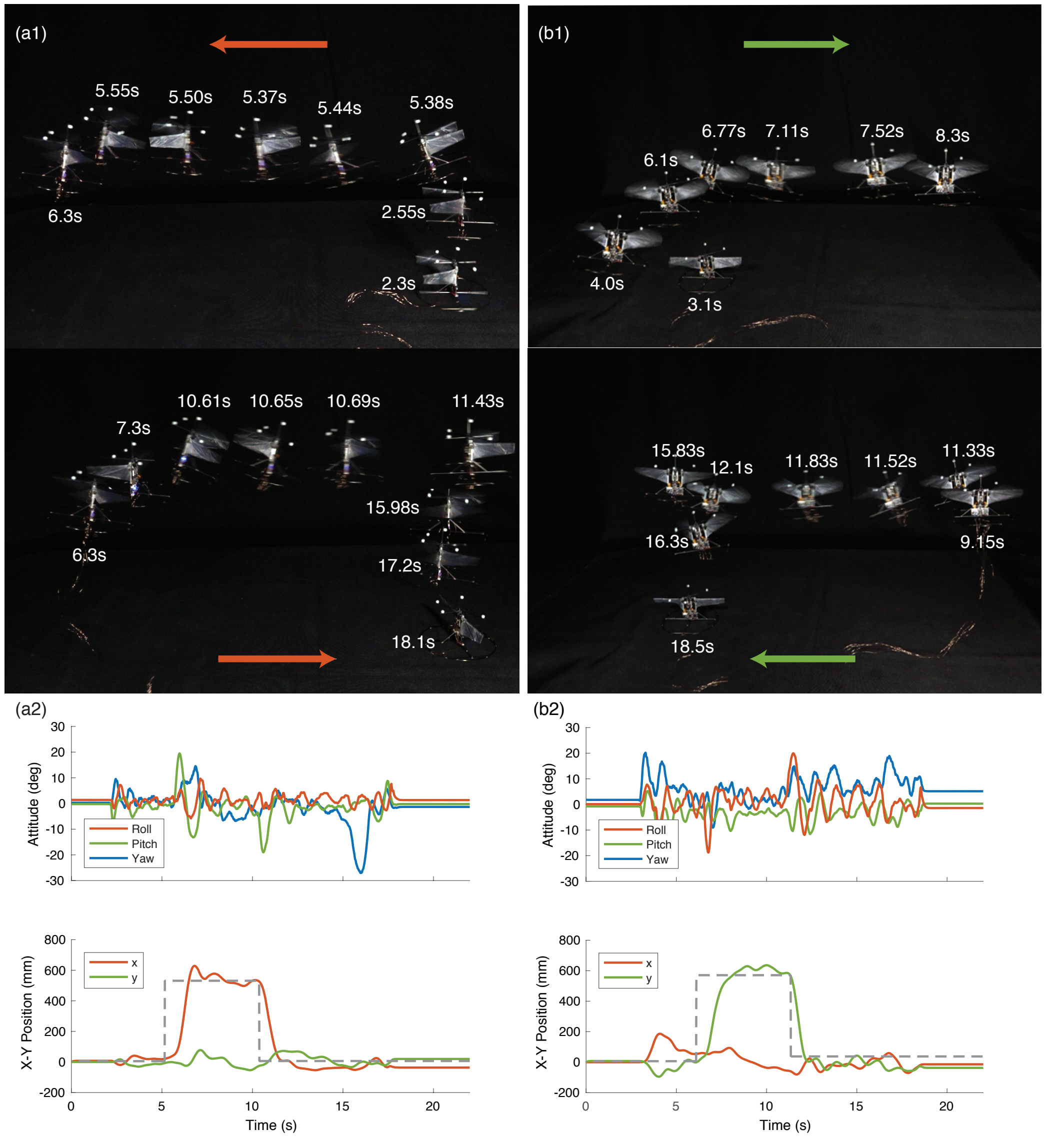

Figure 4.7. : (a1). and (b1). Composed images showing FWMAV point to point tracking fly along longitudinal and lateral direction of the vehicle, respectively. Arrows point out the corresponding flight directions. (a2). and (b2). Attitude and X-Y position of the robot in the test. Gray dash lines represent control references for maneuvering along longitudinal and lateral direction respectively.

their obvious altitude drop in flipping, we show much smaller peak to peak vertical travel, which is less than one wingspan.

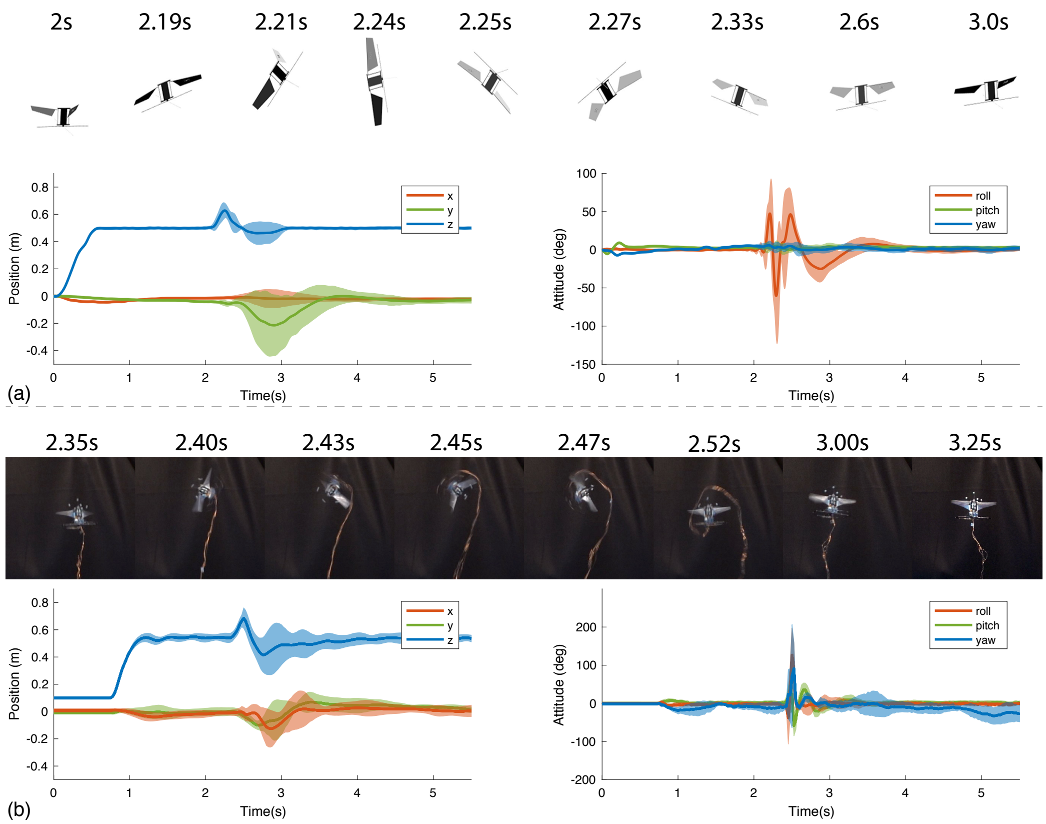

Figure 4.8. : (a). A sample of flip maneuver sequence in simulation. Flight trajectories of the hummingbird robot in simulated flip maneuver is shown. Trajectories are averaged over 5 trials. (b). A sample of flip maneuver sequence in experiment. Flight trajectories of the hummingbird robot in experimental flip maneuver is shown. Trajectories are averaged over 5 trials.

To finish such a tight flip, the robot learned to first generate an upward acceleration. After gaining some momentum, the left wing's amplitude increases to enable the roll turn. When the robot is upside down, the right wing's amplitude increases to decelerate body rotation. To reduce the altitude drop, the maneuver policy is optimized to sacrifice a few X-Y tracking performance. Eventually, the robot will return to the upright position with small overshoots, which results in small lateral position drift. Once return to the normal flight, such a small lateral tracking error can be corrected by the model-based flight controller quickly.

The optimized policy can complete the flip maneuver about 0.13 seconds, and within a vertical travel of approximately one wingspan. This is the first time such maneuver is achieved on a flapping wing robot with only two actuators within such tight spacial constraints, similar to such behaviors observed on animals.

4.5 Conclusion

In this work, we present the attempts to develop a combined control law for bio-inspired flapping wing robots to achieve animal-like stationary hovering and acrobatic maneuvers. Among the design, a model-based controller guarantees the stability of the robot in normal flight. During aggressive maneuvers, a model-free reinforcement learning policy is trained to push the boundary of the flight envelope to approach its extreme performance. We experimentally demonstrate that sustained flight and accurate waypoint tracking based on the proposed robust controller. Furthermore, we demonstrate such AI-assisted control strategy can achieve animal-like drift-free rapid 360° body flip on our hummingbird robot, which is powered by only two actuators. The successful performance in these flight tasks shows the promise of combining robust control and machine learning in mobile robots to cope with system imperfections, unexpected disturbance, and demanding performance on severely underactuated systems.

5. NAVIGATING CONFINED SPACE USING FLAPPING WINGS

Wings of flying animals can not only provide thrust and enable superior flight control, they can also be used to sense their surroundings. Such dual functions of sensing and actuation coupled in one element is particularly useful for those FWMAVs under stringent SWaP constraints while having sensing and navigating demands. In this chapter, we demonstrate the proposed hummingbird robot using its wings for environment sensing and navigation in tight spaces; no visual feedback is required. By interpreting the wing load changes, our robot achieves onboard somatosensory-like feedback. The wing load information indicates the presence of environmental changes such as grounds, walls, stairs, and some other obstacles. Wing load can be onboard quantified from the measurements and interpretation of the current feedback by the motor that actuates the wing. We conducted several flight tests on our hummingbird robot to validate the proposed sensing and navigation approach, which covers three specific tasks: terrain following, wall following, and flying in a narrow corridor. Our robotic hummingbird can successfully finish all the tasks above without visual cues. In sum, using a flapping wing in dual functions - sensor and actuator, is a promising method for the size and weight constrained robots. Such a strategy can also be an alternative or complementary method of visual perception.

5.1 Introduction

Bio-inspired FWMAVs target to achieve the similar stability and maneuverability of flying animals, such as insects and hummingbirds. Besides the flight performance, compared to their natural counterparts, autonomous navigation for such systems is still an open issue, especially in unexplored, tight spaces These are mainly due to their stringent SWaP constraints. These constraints, as well as the undesired vibrations

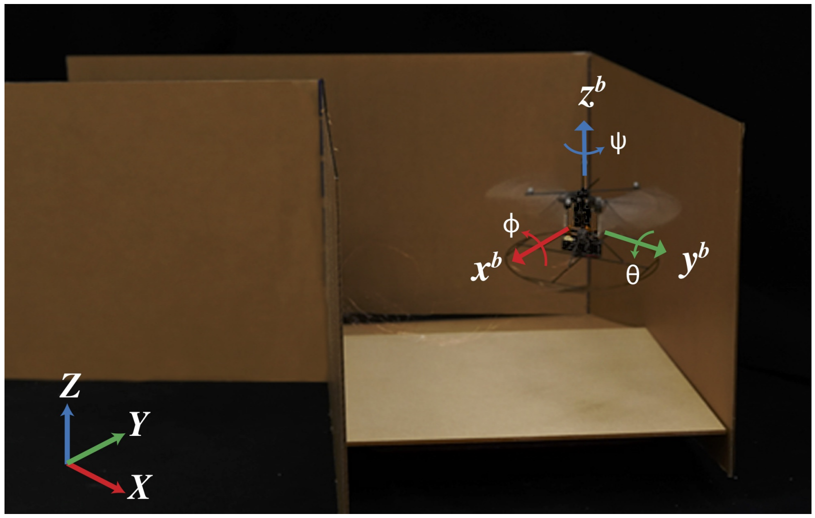

Figure 5.1. : A dual-motor powered hummingbird robot is navigating a 1ft width corridor relying on load variations on its wings. Wing load change can be captured by onboard motor current feedback.

caused by the high-frequency reciprocating wing motion, severely limit the available sensors that can be used for autonomous navigation.

In nature, the flying creatures' wings are usually multi-functional: they not only can generate aerodynamic lift, but also can provide somatosensory information to sense their surroundings. Therefore, they play an important role in the neuromotor control to accommodate the uncertainties in their environments [2, 3, 12, 13]. To date, wings of engineered FWMAVs are usually just for actuation purpose [26, 29, 32, 33, 35, 42]. Employing dual functions of actuation and sensing in flapping wings like the ones in natural flyers has rarely been studied.

In this chapter, we target to autonomous navigation of the FWMAVs by using their flapping wings. We propose to use onboard motor current feedback to capture wing load variation. Environmental changes can induce instantaneous wings load, which in turn manifest as changes in the current feedback of the motors that actuate the wings. Therefore, on FWMAVs, besides generating aerodynamic lift, their wings can be utilized as physical range finders. Such a dual function element can enable autonomous navigation of the FWMAVs that cannot carry visual sensors. The effectiveness of the proposed navigation method is experimentally demonstrated. We conducted several challenging tasks which are essential for tight space navigation on the proposed hummingbird robot: terrain following, wall following, and passing through a narrow corridor with turns, without using any vision or standard proximity sensors. The proposed baseline controller proposed in Chapter 4 is implemented here to ensure flight stability.

5.2 Environment Sensing Principle

5.2.1 Terrain Sensing

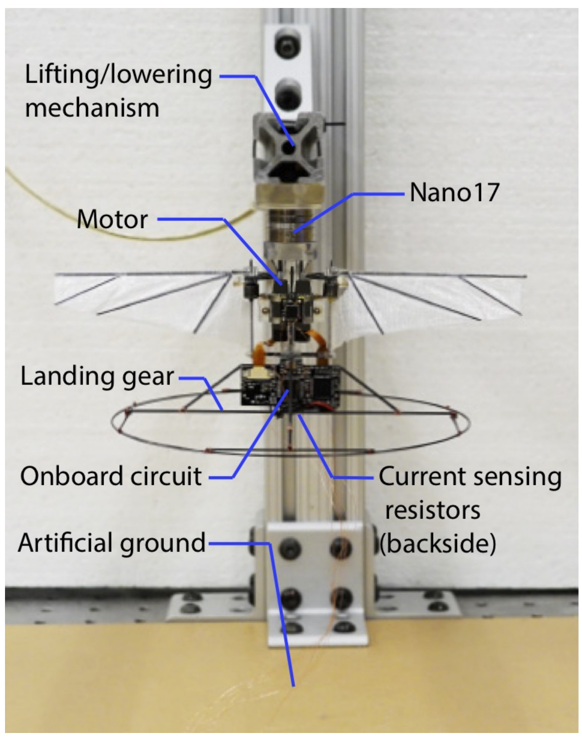

Figure 5.2. : Setup for ground effect quantification.

When the flying animals are approaching the ground, the interaction between the downwash airflow generated by their flapping wings and the ground surface yields a strong aerodynamic forces change (both lift and drag) [101, 102], which is named ground effect. From the real hummingbird study by Kim et al via airflow visualization [101], ground effect results in large lift enhancement. On the proposed hummingbird robot, a similar effect was found as well. In addition, we also observed a simultaneous reduction of the motor current on both wings while the vehicle is flying towards the ground. Such a phenomenon means indicates that the resulting aerodynamic drag is reduced. This correlation between ground clearance and motor current reduction can be employed to detect terrain change.

We experimentally calibrate the ground effect on our hummingbird robot. The details of the experiment setup are shown in Figure 5.2, which is similar to the setup of our wing kinematics validation test. The only difference is the ground clearance between our robot and the artificial ground can be adjusted. All the other lift/torque measurements are the same. Before the test, the robot is aligned to perpendicular to the artificial ground. As introduced in Chapter 2, on our hummingbird robot, two dc motors are used to directly actuate the wings (one per each) with sinusoidal input. For onboard sensing, two 0.3Ω/0.5W sensing resistors are paired with the motor to sense its current feedback. The connection follows the low-side sensing strategy. During the calibration, the vehicle is gradually moved to approach to the ground from $15\bar{c}$ to $1.5\bar{c}$ distance, where $\bar{c}$ is the mean chord length of the wing. For our specific wing morphology, $\bar{c}$=21.2mm. On each certain height, the input voltage of the system ramps up from 10V to 15V with 1V stepsize. The result of a particular voltage is the average of the total 20 datasets. Each dataset contains 3 complete wingbeats data with the 2000Hz sampling frequency. The calibration results are shown in Figure 5.3.

From the calibration result, the ground effect appears around 2-$4\bar{c}$. Within this range, $2.3\bar{c}$ and $3.3\bar{c}$ are two special points as they denote the minimum drag and maximum lift respectively. It shows an interesting finding: the most efficient flying altitude of our hummingbird robot is around $3.3\bar{c}$, which comes with the optimal lift and near-optimal energy cost, maximizing the bonus from the ground effect. For

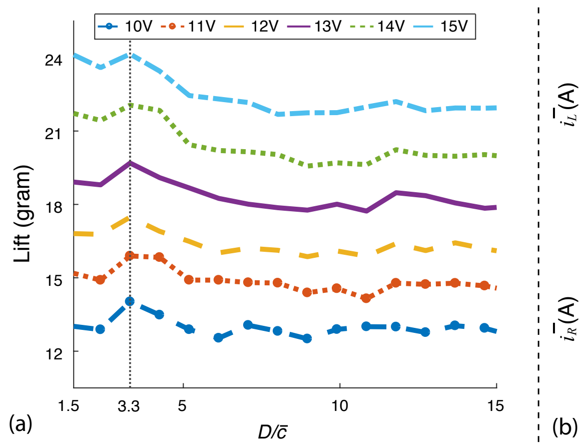

Figure 5.3. : (a). Averaged lift measurement with increased ground clearance. (b). The corresponding motor current change with increased ground clearance. $D/\bar{c}$ is the ratio of ground clearance and mean chord length of the wing. $\bar{i_L}$ and $\bar{i_R}$ are cycle-averaged current feedback of the left and right wing respectively.

implementation, the current value of $3.3\bar{c}$ and the corresponding inputs can be fitting as,

$$\begin{aligned} i_{L_{3.3\bar{c}}} &= 0.015V_s + 0.062, \\ i_{R_{3.3\bar{c}}} &= 0.014V_s + 0.037. \end{aligned} \tag{5.1}$$

During the flight, if we set $3.3\bar{c}$ as the threshold of current feedback, a feedforward altitude control law can complement the proposed baseline control to adapt to the terrain undulation. Meanwhile, the relative altitude can be recorded to analysis the topology of the terrain change.

5.2.2 Wall Sensing

Unlike ground effect test, motor current can not perceive the wall effects of our hummingbird robot. This might be due to the weak tip vortex, as studied on both man-made platforms and animals [7, 101].

Inspired by insects' tactile sensing, we allow the wing to physically contact with objects. The wing collision induced motor current spike can be employed for wall inspection. Wing collision is a severe issue for conventional aircraft with rigid wings. However, due to their typically flexible wings and reciprocating wing motion, FW-MAVs are passively protected by their wings and can survive in collisions.

During flapping flight, an entire wingbeat can be divided into two phases, namely, upstroke and downstroke. The possible collisions on each half-stroke can be sensed by motor current feedback, which indicates the relative location of the obstacles. Therefore, flapping wings can be treated as range finders, which points the objects along with six directions: front, back, front left, front right, back left, back right.

In general, arbitrarily placed wall barriers can be categorized into two different cases as described in Figure 5.4.(a). In the first scenario, the wall obstacle is in front of the robot that barricades its forward path. If a collision happens, both wings would show increased current feedback on the upstroke. Compared to the unaffected downstroke current feedback, the obstacle location can be identified accordingly. The same strategy can be implemented to the backward flight case. Actually, the collision not only causes the current differential change, but it also results in an overall higher mean current compare to the normal flight. In the second scenario, the wall barrier is along the wing spanwise direction which blocks the side path as shown in Figure 5.4.(b). In this case, only one wing collide, which yields the related motor current changing while the other one not.

Considering the trim condition, to enable sensing function, the motor current feedback needs to be calibrated, including upstroke and downstroke movement for both two wings. To demonstrate the navigation capability of our hummingbird robot, we calibrated the touch-based current feedback with the $3.3\bar{c}$ ground clearance to integrate ground sensing for the later flight test. An artificial wall is set for allowing wing collision as shown in Figure 5.4.(c). The motor input is the same as the previous ground effect test. The calibration result is shown in Figure 5.5. Both wings on both stroke directions show about 10% increase of the motor normal current during the

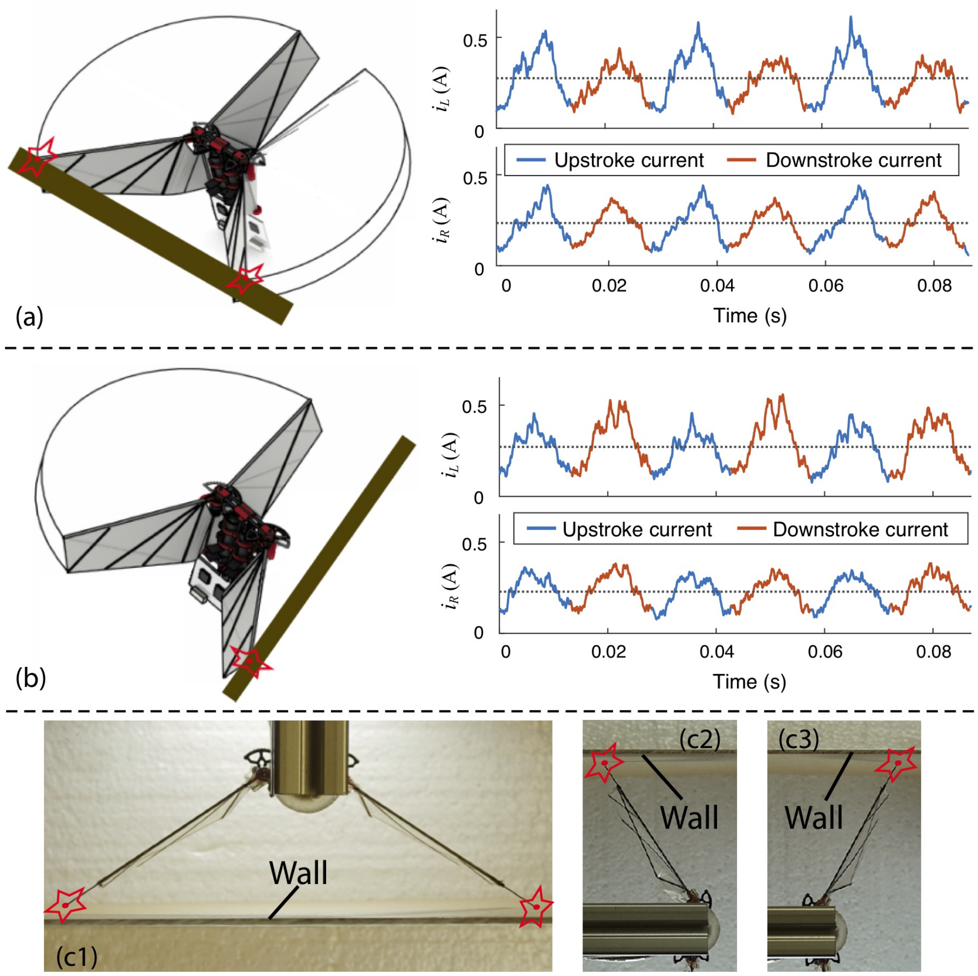

Figure 5.4. : (a). When both wings hit the front-side obstacle during the forward flight (left figure), the corresponding plot of instantaneous motor current showing both wings' upstroke currents is higher than normal (right figure). (b). When the left wing's downstroke is blocking on the side by the wall barrier (left figure), only the corresponding left wings' downstroke current becomes greater than normal (right figure). (c1)-(c3). Illustration of the setup for quantifying the wing collision effect, including bumping from front/back-side as (c1) and upstroke/downstroke-side as (c2) and (c3).

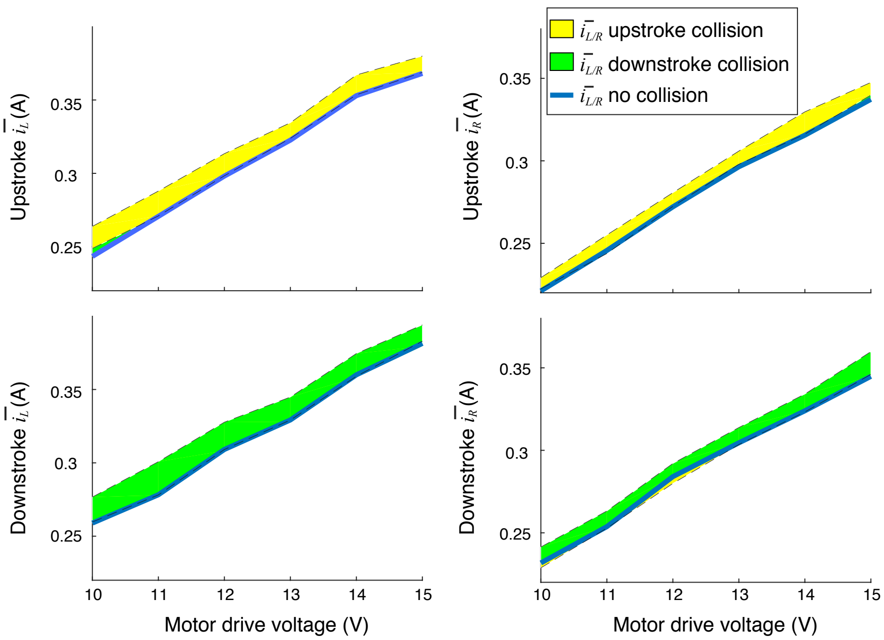

Figure 5.5. : Calibrated upper bound of the motor current feedback according to different collision scenarios.

collision. The incremental current caused by collisions rises approximately linearly with the voltage increasing.

5.3 Motion Plan

As discussed in section 5.2, the motor current feedback of our FWMAV can be used to identify different environmental factors and further assist in navigation, especially when the robot is flying in compact spaces without vision or proximity sensors.

To detect and follow the terrain change, a feedforward control is proposed,

$$\begin{aligned}\delta z_r &= K_{\hat{z}}(i_{L/R} - i_{3.3\bar{c}_{L/R}}),\\ z_r &= z_r + \delta z_r,\end{aligned} \tag{5.2}$$

where δz_r is the detected relative altitude variation, $K_{\hat{z}}$ is the feedforward proportion gain, and z_r is the altitude reference.

To achieve a stable terrain sensing and following, mathematically, $cos\phi cos\theta \approx 1$, namely, attitude control error should be fairly small. As relatively noisy feedback, current fluctuation can result in oscillated z control performance. Therefore, we implemented a low-pass filter for signal conditioning, the cut-off frequency of which is 200Hz. In addition, we set a response dead-band for the current readings, which is tuned to be 75%-100% of $i_{L/R_{3.3\bar{c}}}$ to delay the possible aggressive altitude control. Obviously, in the dead-band zone, the following performance would be limited. Nevertheless, such a design smooth the altitude travel effectively.

For lateral control, ideally, the robot positioning can always be handled by the VICON system. Therefore, through touch-based sensing, the robot can detect where the obstacle is and then alter its default flying path for avoidance. However, VICON sometimes can be blinded due to object shield and light condition restriction, losing the object tracking. It causes that the robot loses its position feedback and affects the pre-plan trajectory tracking accordingly. To address this problem in actual flight, we use the onboard IMU to approximate the robot position in a short period until the VICON system recovered. A 2-D transformation matrix is defined by

$$\begin{bmatrix} x_k \\ y_k \\ 1 \end{bmatrix} = \begin{bmatrix} \begin{bmatrix} cos\psi & -sin\psi \\ sin\psi & cos\psi \end{bmatrix} & [x_{k-1}, y_{k-1}]^T \\ 0 & 1 \end{bmatrix} \boldsymbol{p^b} \tag{5.3}$$

where $\boldsymbol{p^b} = (x^b, y^b, 1)$ is the augmented lateral position vector in the body frame.

With continuously position feedback, the flying path planning of the robot can be keep updating. To demonstrate the sensing capability discussed in section 5.2.2, we implemented a simple and robust path planning method to address obstacle following and avoidance demands: When a blind FWMAV flying in an unexplored space with obstacles, firstly, the planner is greedy to shorten the flight time - straightly flying towards its target point; once the obstacles were detected by wing collision, a retreating action along the opposite direction of the detected obstacle was performed; then shifting the original flight trajectory along the perpendicular direction of the current moving direction for collision avoidance. Keeping the head orientation, the timing greedy policy will pilot the robot to perform a 'following' flight if it continuous shifts its flight path. Once it bypassed all obstacles, it would directly fly towards the target. Such a method is similar to 'Bug' planner [103, 104].

5.4 Experimental Result and Discussion

To validate the proposed sensing method, we conducted several flight tests. At first, we demonstrated the basic terrain and wall following the capabilities of our hummingbird robot. Then, the robot is commanded to navigate a narrow corridor blindly, which integrates walls and terrain change together. The results show that FWMAVs can use their wings as the primary sensor to sensing and map the surroundings.

5.4.1 Terrain Following

In this test, the robot is planned to perform a point to point flight blindly. A 1ft length ramp with 20° slope is placed on the way to make the terrain change. The robot crossed over successfully with ground effect sensing. In the beginning, around 2-4s, the robot ascended high first and then descended to detect the ground. Once it has been detected, the robot starts to move forward with a certain speed. Based on the motor current feedback, if terrain change was detected, i.e., motor current is much lower than the predefined threshold $i_{L_{3.3\bar{c}}}$ and $i_{R_{3.3\bar{c}}}$ (out of the dead-band zone), altitude reference will be adjusted accordingly to accommodate such terrain change as demonstrated in 7-8s, 9-10s, and 11-13s flight. During such terrain following, the robot keeps recording altitude information. With the recorded data, the flight trajectory (z-axis) can be further used to reconstruct the actual terrain topology as shown in Figure 5.6.(c).

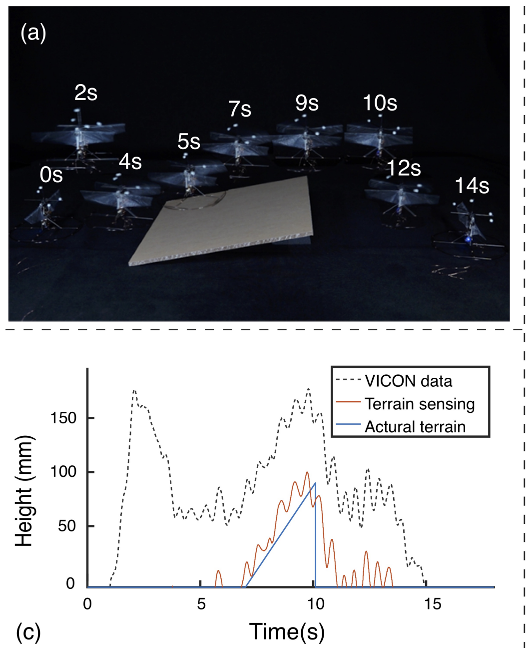

Figure 5.6. : (a). Time sequential result of a typical terrain sensing and mapping test. (b). The cycle-averaged current feedback data corresponds to (a). (c). Altitude mapping result through ground effect.

5.4.2 Wall Following

In this test, the robot was commanded to perform a point to point flight, same as the terrain following test. A $1{\times}2\text{ft}^2$ wall is placed on its way to block the flying path. During the flight, the robot relied on the wing collisions to sense the wall, and then altered the flight trajectory to avoid it. As shown in Figure 5.7, in this typical flight test, after a couple of collisions and path alternations (around at 5s, 8s, 10s, 13s), the vehicle passed the wall. Through the touch-based navigation method, the instantaneous motor current feedback can indicate wing collisions and obstacles existence. As shown in Figure 5.7.(b), the two enlarged areas with detailed upstroke/downstroke current feedback are corresponding to the 8s and 13s collisions in this flight trial. They represent collision case 1 and 2 as mentioned in section.5.2.2 respectively. Since the instantaneous motor current signal is noisy, in order to eliminate false positives,

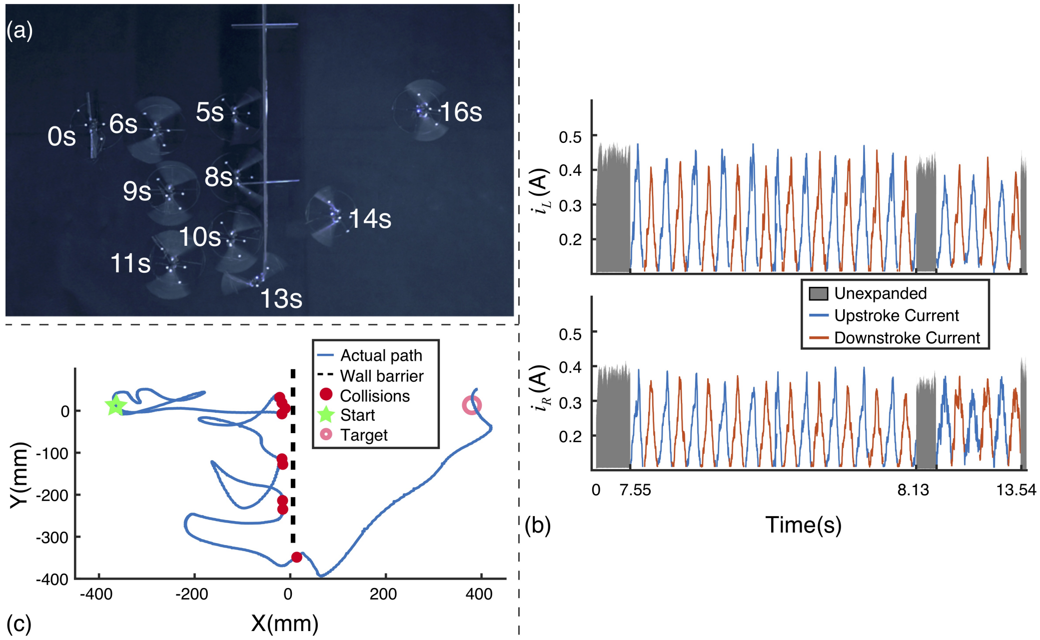

Figure 5.7. : (a). Time sequential result of a typical wall sensing and mapping test. (b). The instantaneous current feedback data corresponds to (a). (c). Actual flight path with collisions and path alternations.

multiple wing collisions are allowed around the suspected obstacle location. Meanwhile, during the flight, as long as the collisions were detected, the coordinate of such bumping points would be recorded. As shown in Figure 5.7.(c), with the recorded points, we can roughly sketch the outline of the obstacle.

5.4.3 Passing Narrow Corridor

In this test, our robot challenged navigating a narrow corridor with a sharp turn. The corridor was constructed with both wall barrier and varying terrain, which can block VICON feedback in some spots. To further increase the difficulty, the path width of the corridor was adjusted to less than two wingspans of our robot. Without any aiding information, navigating such a tight, unexplored, obstacle-filled space can be a challenging task for most MAVs. We demonstrated that flapping wing MAVs

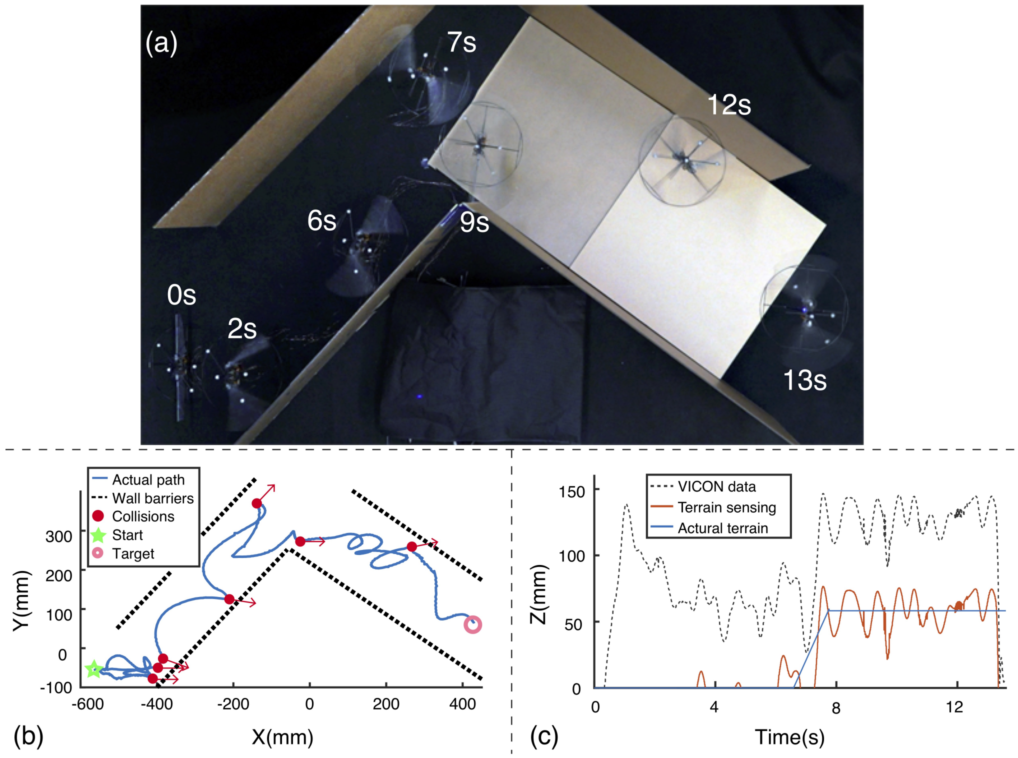

Figure 5.8. : (a). Time sequential result of a typical corridor navigating. (b). Actual flight path with collisions and path alternations. (c). Altitude mapping result through ground effect.

with the somatosensory-like feedback of their reciprocating wings show a natural advantage in the perception and adaptation of complex environments. Although Without visual sensor support, the robot successfully finished this flight task with solely the interpreted environmental information from the wings that enable the fly. Similar to the above two tests, with the recorded ground surface information and collision coordinates, the contours of the obstacles can be extracted. A typical flight path and obstacle detections are shown in Figure 5.8.(b)(c). The red dot and arrow indicate the perceived obstacle point and the corresponding heading direction in collisions.

With multiple flights, the distribution of collision points can be more uniform which result in a more complete and accurate outline of the corridor interior as shown in Figure 5.9. With such information, an artificial field can be generated to facilitate planning a safety path, aiding the later on platforms to avoid superfluous collisions. With a central node that gathers all of the collision points, this concept is certainly feasible and can be extended to many complex application scenarios.

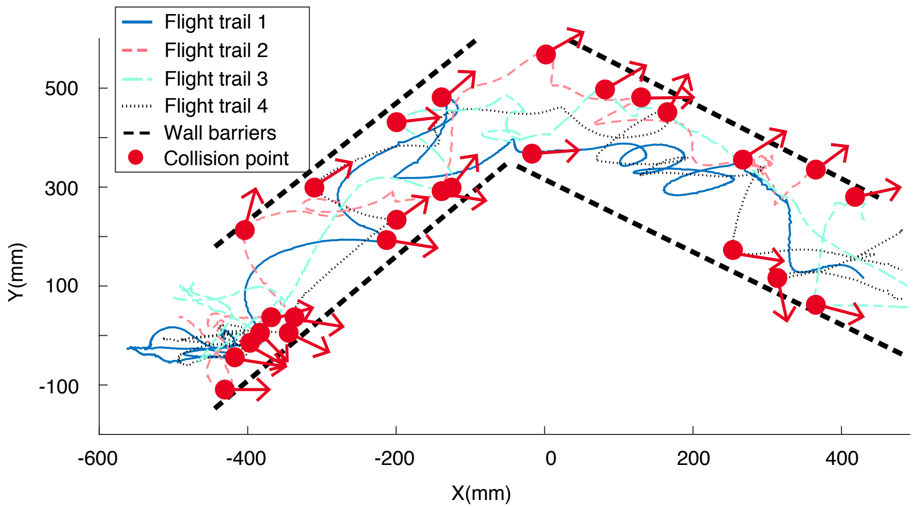

Figure 5.9. : With more flights, the contours of the corridor can be sketched clearly.

5.5 Conclusions

In this chapter, we propose to use actuator loading to sense surrounding change and assist onboard navigation of MAVs in confined spaces. The main concept of this design is inspired by flying animals, whose wings can be a somatosensory sensor to perceive surrounding changes and aid in motion/path planning. Different from fixed or rotary-winged vehicles, FWMAVs take such a unique advantage from their natural counterparts, using their reciprocating wings in dual-functions: actuation and sensing. In this work, we demonstrate the first hummingbird-scale robot using its flapping wings to obtain the somatosensory-like feedback. Such a sensing function is enabled by incorporating the instantaneous motor current feedback of the wing system, which directly senses wing load change while it does not affect its actuation function. The feasibility of the proposed sensing method has been experimentally validated. We successfully use our robotic hummingbird's flapping wings as the primary sensor for navigating through a tight, unexplored, obstacle-filled space. Such a dual-functional design provides many advantages, such as no additional payload, high sensing bandwidth and sensitivity (depending on wingbeat frequency), and low computation load which hold a great promise on a variety of applications for the robots who faces SWaP constraints. Furthermore, it can serve as an alternative or complementary method to other sensing approaches.

6. UNTETHERED FLIGHT

In this chapter, we present the first bio-inspired FWMAV powered by only two actuators and capable of sustained untethered flight in both indoor and outdoor environment. Sustained stable hovering of the proposed FWMAV is achieved through a pair of independently controlled wings, a key inspiration from its natural counterparts.

The untethered flight of such FWMAVs is a challenging task due to stringent payload limitation from severe underactuation and power efficiency challenge caused by motor reciprocating motion. In this work, we present the detailed modeling, optimization, and system integration of onboard power, actuation, sensing, and flight control to address these unique challenges of such FWMAV during untethered flight. We performed untethered flight experiments in both indoor and outdoor environment and demonstrate sustained stable flight of the robot.

Figure 6.1. : Untethered sustained outdoor hover flight of a hummingbird-scale flapping wing robot. Background is blurred to reduce distractions.

6.1 Introduction

Drawing inspiration from insects and hummingbirds for their hovering capability and acrobatic maneuvering performance [6, 7, 9], researchers have been creating bio-inspired Micro Air Vehicles (MAVs) with morphology and kinematics similar to their natural counterparts. Compared to conventional flying vehicles, flapping wing MAVs are capable of sustained flight with small-sized wings and low Reynolds numbers due to their unique unsteady aerodynamic mechanism. Therefore, they are promising alternatives to conventional MAVs especially at small-scale and can work favorably in tight indoor spaces as well as outdoor environments.

To date, several prototype insect or hummingbird scale Flapping Wing Micro Air Vehicles (FWMAVs) have demonstrated stable hovering [26, 31, 32, 35, 42, 43, 105]. Their flapping mechanisms are either based on a unidirectional motor coupled with four-bar (or equivalent) [26, 31, 32, 35] or direct-driven bi-directional actuation [42, 43, 105]. Accordingly, flight control is achieved through either additional servos to modulate wing stroke plane or wing differential (of left and right wings) [26,31,32,35] or instantaneous direct and independent modulation of wing kinematics [42, 43, 105]. In the latter case, by taking advantages of decoupled wings with independent wing kinematic control, such bio-inspired flapping-wing vehicles employ the key inspiration from real animals and can approximate their highly controllable and maneuverable flight even though they are severely underactuated [43, 47].

Untethered flight of insect or hummingbird inspired platforms have appeared in recent years. For the insect-inspired platforms, [37] and [38] have demonstrated untethered liftoff, showing the potential for fully untethered autonomous flight. While insect-sized platforms may have their specific limitation on the size and weight of payload, larger platforms such as hummingbird-sized MAVs have the potential to accommodate larger and heavier payload and off-the-shelf sensors, microcontrollers, and power source. To date, the untethered flight of hummingbird-sized FWMAVs is based on unidirectional motor(s) actuated four-bar mechanism coupled with additional servos for flight control [26, 31, 32, 35]. As a result, system integration for the untethered flight of such systems is relatively straightforward with available solutions and commercially available controller and driver modules. For the direct-drive bi-directional motor actuated platform such as the one described in this chaper, a systematic wing-actuation system design is needed to address instantaneous power fluctuation and energy consumption due to frequent acceleration and deceleration of the motors from their fast reciprocating motion. Such a unique power efficiency issue, coupled with payload capacity constraints caused by actuation limitation, calls for systematic design optimization and customized hardware and software solutions in system integration of the untethered robot to accommodate SWaP constraint.

In this work, we present the sustained stable untethered flight of a dual-motor actuated at-scale hummingbird robot. Compared to our previous tethered design which has unlimited energy input via power wires in Chapter 3∼5, untethered flight becomes energetically expensive and requires more payload capacity to handle onboard power source. Correspondingly, the system integration becomes more challenging because it requires to lead the prototyped vehicle close to its natural counterparts' size and weight meanwhile provide sufficient power and control effort. In this article, the particular issue of such a severely underactuated bio-inspired system - trade-off between payload limitation and power efficiency, has been solved systematically through a multi-object optimization. Following the guidance from the optimization result, the system integration challenge has been addressed by customized onboard actuation, sensing, control, and power supply designs. In particular, two DC motors are used to actuate the vehicle. The wing trajectories are altered by two independent onboard drivers, which is controlled by an STM32 microcontroller for desired aerodynamic thrust and control torques generation. Body attitude of the proposed platform is sensed by onboard inertial sensors. A customized dc-dc power regulator is attached to separate the power of logic and actuation circuits. System power comes from two rechargeable onboard batteries. All components and parameters of the system are carefully selected to satisfy performance requirements while matching real hummingbirds' size and weight. Both indoor and outdoor flight tests have been conducted experimentally. To the best of our knowledge, such results present the first bio-inspired FWMAV powered by only two actuators and capable of performing sustained autonomous flight. It is also the first untethered flight of an at-scale tailless hummingbird robot with independently controlled wings, a key inspiration from its natural counterparts.

6.2 System Design

Based on the modeling of the motor-wing dynamics and energy consumption in section 2.2.3, a systematic design optimization was conducted to inspire the untethered vehicle design, which governs wing morphology and kinematics, system resonance, actuator characteristics, power input, and power regulation performance. Besides the single object optimization in the previous design [36], which only focuses on generating sufficient thrust and control effort, energy efficiency is also important and is incorporated here to accommodate energy consumption and payload constraints for untethered flight. As a result, multi-object optimization is used here to address payload capacity and energy efficiency challenges in such design. This optimization problem can be formulated as: defining objective functions $[f_1(\boldsymbol{x}), f_2(\boldsymbol{x}), f_3(\boldsymbol{x}), ..., f_n(\boldsymbol{x})]$ that needs to be minimized over the vector $\boldsymbol{x}$ subject to certain constraints $\boldsymbol{X}$.

In particular, the optimization is

$$min[-\gamma_{l2w}(\boldsymbol{x}), -\bar{\eta}(\boldsymbol{x})], \quad \boldsymbol{x} \in \boldsymbol{X} \tag{6.1}$$

where $\gamma_{l2w}(\boldsymbol{x})$ represents lift-to-weight ratio, $\bar{\eta}(\boldsymbol{x})$ is the averaged actuation efficiency, $\boldsymbol{x}$ is the feature vector of the design subject to certain constraints. In particular, we define $\boldsymbol{x} = [R_w, \bar{c}, f, \Psi_w, N_g, K_s, \zeta]^T$.

We set boundary condition $\boldsymbol{X}$ according to the biological inspiration, e.g., mimicking wing morphology and the key kinematic characteristics from real hummingbirds. In particular, $R_w \in [50, 90]$ mm, $\bar{c} \in [8, 40]$ mm, $f \in [10, 50]$ Hz, to cover the different hummingbird species. $\Psi_w \in [0, \pm 95]$, which represents the range of stroke amplitude

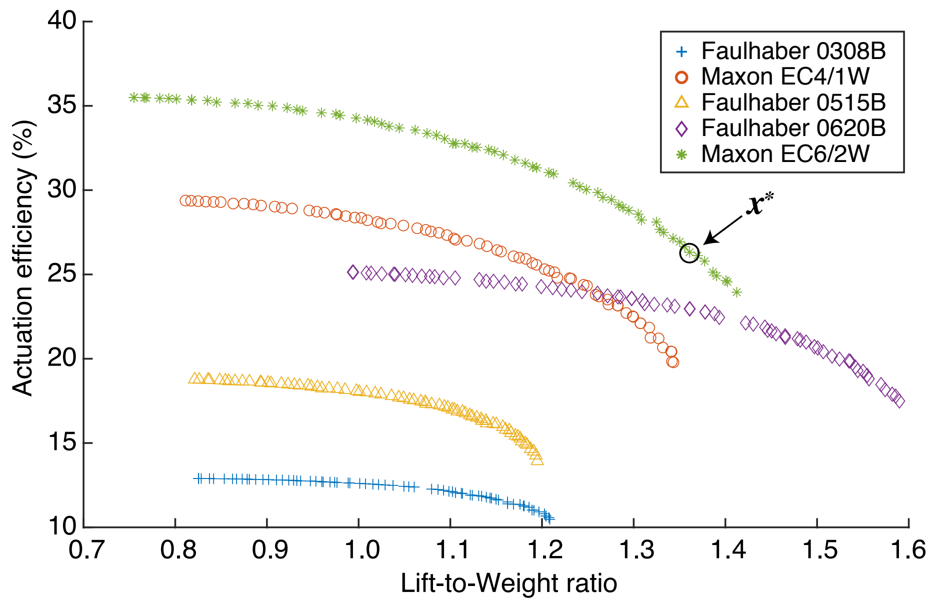

Figure 6.2. : Pareto Front of the robot design. $\boldsymbol{x}^*$ is the selected design.

of the wing. Ψ_w is constrained by mechanical configurations particularly. In addition, our previous design experience also provides valuable intuitions for gear and spring (N_g and K_s) selection [36]. Power loss in regulation step is calibrated and detailed in section 6.3. Generic algorithm is used here to solve the numerical solution. Population size is 200. Termination criteria is defined by maximum generations, which is set to 200. Crossover law is used for combining the genes. Fitness function is formulated based on the wing kinematics modeling and efficiency estimation presented in Chapter 2. The optimal result is shown in Figure 6.2.

Note that actuator selection is essential since its weight and power density determines the scale of the entire system. To achieve an at-scale robot similar to real hummingbird size and weight, we use small size DC motor due to its high power density at tens-of-gram scale [29], as presented in Chapter 1. For this purpose, we studied the off-the-shelf high-performance 3$\sim$6mm diameter precision motors to seek optimized solutions, as shown in Figure 6.2. Our final choice is Maxon EC6Φ2W with $\boldsymbol{x}^* = [70, 21.2, 34, \pm 75, 10, 0.0134, 0.8]$. Such a design resulted in a vehicle close to a typical magnificent hummingbird presented in [5], whose $R_w = 77\text{mm}, \bar{c} = 19.5\text{mm}, f = 32\text{Hz}$. Furthermore, as shown in Figure 6.2, it can handle the particular payload capacity and power efficiency requirement of the proposed hummingbird robot to achieve untethered autonomous flight.

General physical parameters of our specific wing-actuation system can be found in Table 6.1. The untethered design of the proposed hummingbird robot is shown in Figure 6.3. It keeps similar morphology as the tethered flight version and the total weight grows up to 20.4 grams with batteries and onboard electronics. Details of the onboard system are presented in section 6.3.

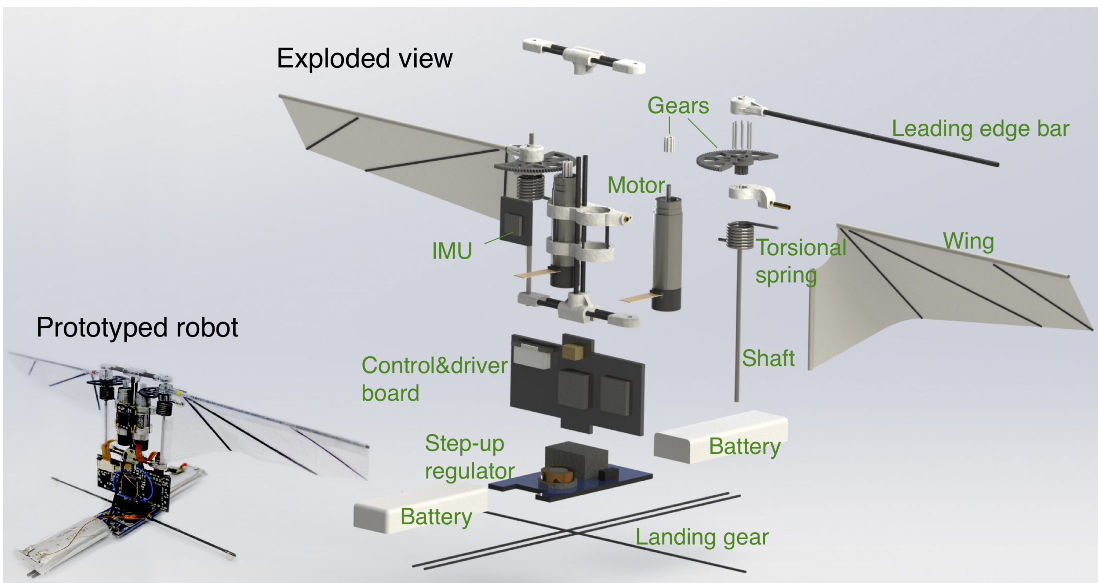

Figure 6.3. : Illustration of system integration of the proposed robot.

6.3 Onboard System Integration

In this section, we detail the design and integration of the onboard system. The prototyped platform consists of motor drivers, a micro control unit, onboard sensors, and power regulation circuits. The design follows the design presented in Table 6.1. As a result, Figure 6.4 shows the schematic diagram and the prototyped circuits respectively. We introduce each module one by one below.

Table 6.1. : Parameters of The Proposed Wing-actuation System

term	definition	value	unit
J_m	motor inertia	0.703	g.mm^2
B_m	motor damping	9700	mN.mm.sec
K_a	motor torque constant	1750	mN.mm/A
R_a	motor winding resistor	12.4	Ohm
N_g	gear ration	10	-
η_g	gear efficiency	0.8	-
J_g	gear inertia	4.7	g.mm^2
K_s	spring coefficient	0.0134	mN.mm/rad
J_w	wing inertia (stroke direction)	215.9	g.mm^2
J_{w_r}	wing inertia (rotation direction)	14.0	g.mm^2
$J_{w_{rs}}$	product wing inertia (rotation-stroke)	26.5	g.mm^2
α	optimized AOA	≈ 45	degree
R_w	wing span length	70	mm
$\bar{r}$	mean chord length	21.2	mm
$\bar{B}_w$	cycle-averaged aerodynamic damping coefficient	61856	mN.mm.sec
$\hat{r}_1$	1st dimensionless moment of wing area	0.4	-
$\hat{r}_2$	2nd dimensionless moment of wing area	0.53	-
$\hat{r}_3$	3rd dimensionless moment of wing area	0.59	-
m_w	wing mass	0.09	g
Ψ_{w_0}	nominal stroke amplitude	± 75	degree
ζ	power regulation efficiency	0.8	-

6.3.1 Actuation

To enable the flapping motion of wings, the motors undergo bi-directional oscillation. The DC motors are driven by alternating magnetic fields generated by switching

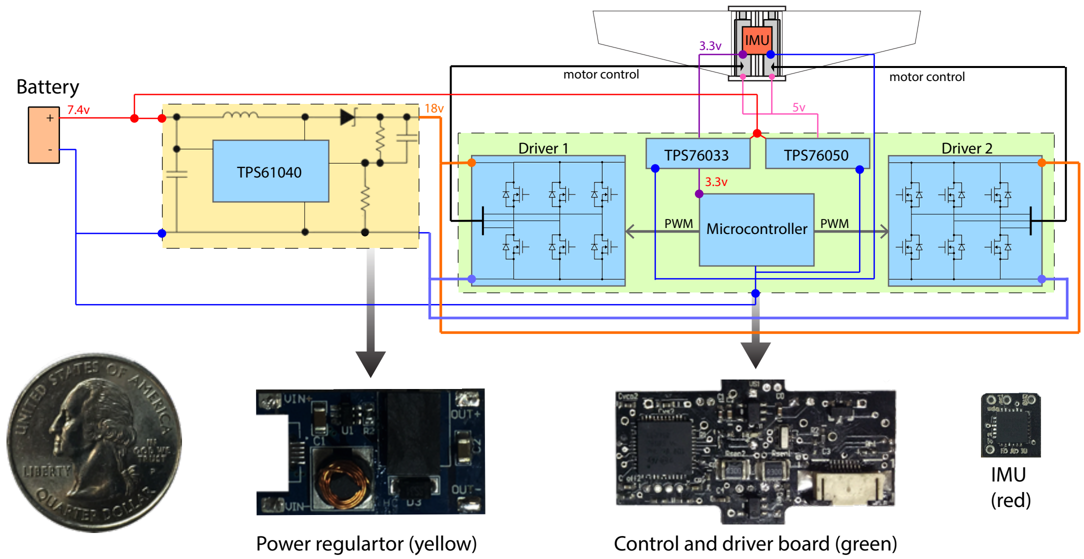

Figure 6.4. : Schematic diagram and prototyped circuits of the complete onboard electronic system that enables untethered flight of the proposed hummingbird robot.

the motor commutation sequence periodically. Here we use H-bridge circuit which is composed of three pairs of DMOS (double-diffused MOSFET) transistors to power the motor. Each motor has three embedded hall sensors to provide rotational position feedback for motor commutation. With this basic circuit structure, we can specify the requirement of the power capability of the onboard driver based on the estimated power consumption as discussed in section 2.2.3. The power specifications, namely gate-source voltage and peak-peak output current, can then be estimated and used to guide the specific driver design. As shown in Figure 6.4, the prototype circuit board on the test platform was equipped with two DMOS driver-L6235Q (7×7×1mm, 0.14 grams), and it is able to conduct 8-18V gate-source voltage and 0.1-1.2A continuously current on a 10×34mm^2 customized printed circuit board (PCB).

Performance of the circuit depends not only on the appropriate transistor used, but also carefully designed peripheral circuits. Since the H-bridge usually behaves like a switch, it imposes a problem where the output power drops too much during the periods of motor commutation. To solve this problem, installing a reservoir capacitor for instantaneous power bootstrap is a practical solution. A fitted reservoir capacitor is the key component in the entire driver circuit design since it dominates the consistency of the electrical power. Without it, the wing actuation system cannot generate lift. During the wing flapping, the reservoir capacitor undergoes simultaneous charged-discharged frequently. Therefore, in order to provide adequate energy for bootstrapping, the power capability of the reservoir capacitor must be higher than the power consumption on the discharged stage. The averaged power capability of reservoir capacitor P_c is given by

$$P_c = C_r V^2 / 2t_c, \tag{6.2}$$

where t_c is the operation time, and C_r is the desired capacitance of the reservoir capacitor.

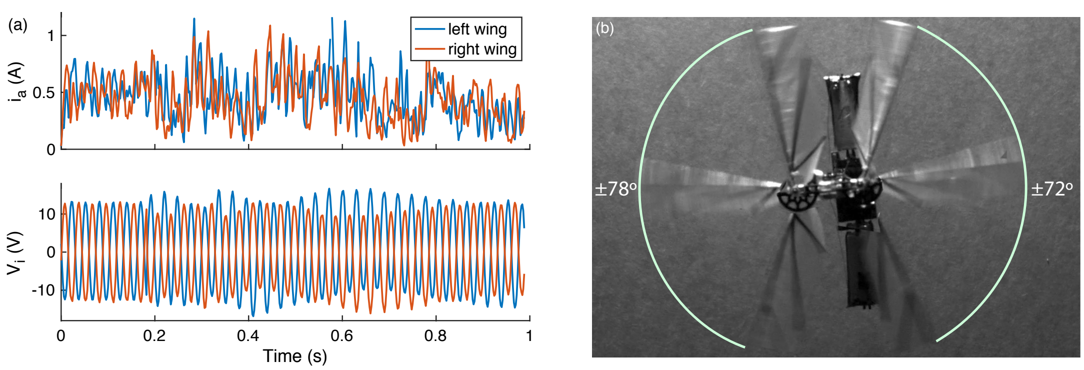

Figure 6.5. : (a). A typical record of the instantaneous current and voltage in normal hover flight condition. (b).The differential amplitude of the left and right wings are generated by flight control for the attitude stabilization. Digitized wing kinematics can be used for runtime power estimation.

A typical runtime power consumption is shown in Figure 6.5, which requires 13.0V/0.47A mean voltage/current for stable hovering. Based on equation 2.12, the overall power efficiency is about 24% in this test. To govern all possible flight conditions, the reservoir capacitor on our platform should at least be 32.7uF theoretically. Considering the commercially availability and the fabrication errors, 47uF is currently used. With a certain capacitance, we can choose dielectric material then. Since the effect of dielectric materials on actuation performance is difficult to model, we verify it through experimental tests. The result is shown in Figure 6.6. In Figure 6.6, the lift generation result of a particular voltage is the average of a total of five datasets wherein one dataset contains 100000 samples of wing motion data with the 5KHz sampling frequency. As a result, Multi-Layer Ceramic Capacitors (MLCCs) can compete with the others and exhibit overall as good performance as the tantalum capacitor. Actually, both MLCCs and tantalum capacitors are fitted to the test platform, in which the overall weight of the MLCC is lighter, while the tantalum capacitor performs better under thermal effect. Aluminum capacitors are not competitive in performance, especially when the motor is overheated.

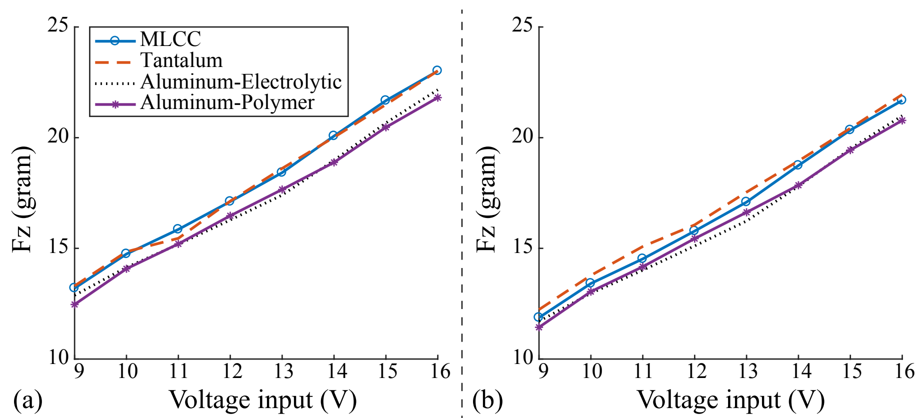

Figure 6.6. : Performance comparison of bootstrap capacitance with different dielectrics. (a). Motor and driver working in normal condition. (b). Motor and driver working in overheated condition.

For the selection of the bootstrap capacitor, the equivalent series resistance also needs to be considered, because it is one of the leading causes of motor torque ripple. As expressed in

$$V_o = V_s - I_o * (R_{eq} + t_{on}/C_{res}), \tag{6.3}$$

where V_o and I_o are the output voltage and current respectively, V_s is the power source voltage, R_{eq} is the equivalent series resistance of the bootstrap capacitor, and t_{on} is the discharging time. Since $t_{on}/C_{res} \approx 0$, $I_o * R_{eq}$ is the approximated voltage ripple. Depending on the maximum allowed voltage ripple ΔV and the corresponding output current of the driver board, the selection of a reservoir capacitor must satisfy $R_{eq} < \Delta V/I_o$.

Note, torque ripple is not only derived from R_{eq}, but also from the parasitic inductance in the circuit, backlash of the gears, airframe vibrations, and unsteady aerodynamics. Placing small ceramic capacitors close to the power source and the ground pin can counter the impact of parasitic inductance. Other mechanical factors can only be attenuated by elaborated components layout and active control.

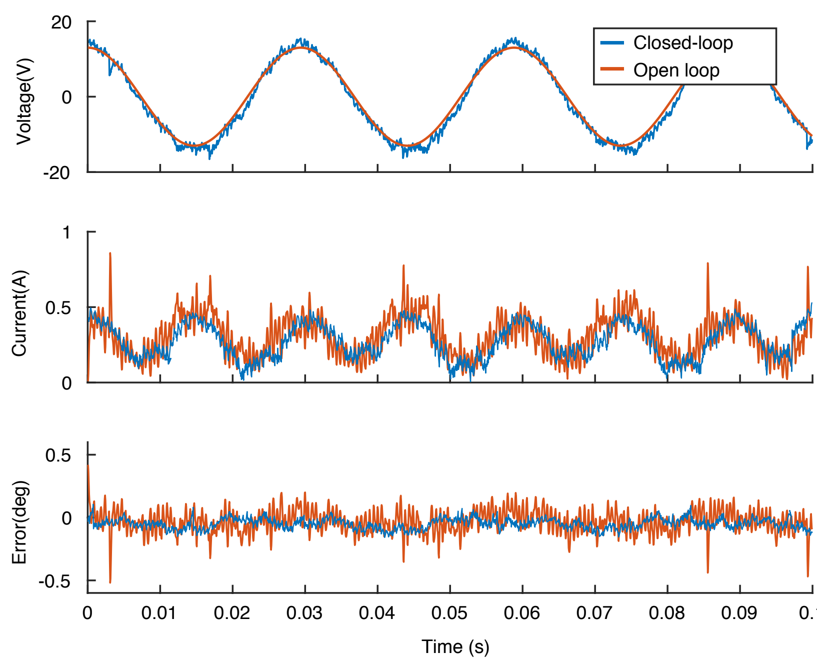

Figure 6.7. : Torque ripple suppression via motor current control.

For our direct-drive wings, the motor current feedback directly responds to the motor load changes, including aerodynamic changes, cogging force, and torque ripples. In the case of the pure open-loop control of the wing kinematics, the output torque expresses relative strong pulsations as shown in Figure 6.7. In order to acquire a smoother torque output, active current control is implemented on the test flapping-wing platform to reject the external disturbances. In particular, a proportional-integrated controller is used. Current feedback passes through a 200Hz filter to attenuate control input jerks. Compare to the open-loop control result, the torque ripple is reduced, which is reflected in the motor current feedback, i.e., fluctuation magnitude reduced from $\pm$ 0.5A to $\pm$ 0.15A.

6.3.2 Sensing and Control

For onboard sensing, two sensing resistors and a splitting IMU module are equipped on the robot for motor current feedback and attitude sensing, as introduced in previous chapters. The selected sensors are both with small sizes and lightweights. An STM32 microcontroller was chosen as our onboard Micro Control Unit (MCU), which combines a 32-bit ARM Cortex-M4 core (with FPU and DSP instructions), running at 72 MHz. Such a microcontroller allows analog input/output, such as current feedback, while handling other digital auxiliary sensors and peripheral devices. In normal flight, the embedded microcontroller should handle: 3 timers for wing kinematics control, sensor fusion and flight control, and communication; 1 I2C port to gather IMU measurements; 1 serial port to communicate with the ground station to get position feedback; 6 PWMs for motor control; 2 analog input port for current sensing. For the outdoor test, due to the lack of the miniaturized position sensor, our position control algorithm presented in Chapter 4 cannot be enabled on this tetherless platform. Attitude controller is always working behind for stabilization.

6.3.3 Power Regulation

Considering the payload limitations of the vehicle and the availability of commercial products, we use two 100mAh Li-po batteries (zon.cell LP601420P30) as the on-board power supply. The total weight of the onboard batteries is about 5∼6 grams. Such a weight cost has already been considered in system optimization.

The onboard system is assembled with logic and analog circuits. Their rated working conditions are completely different. We implement three power regulation circuits to enable their respective functions. Original battery output (≈ 7.4V) is converted to 3.3V and 5V to power the onboard microcontroller and sensors. Such regulators - TPS76033/50 are embedded in the control and driver board.

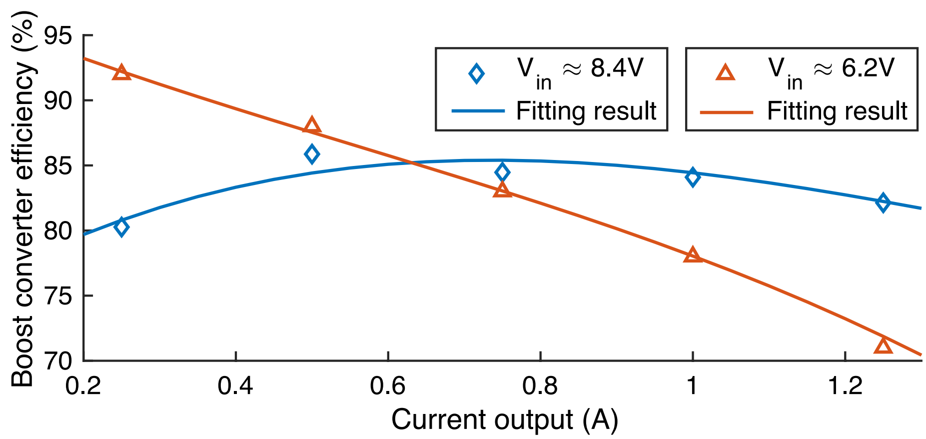

Figure 6.8. : Illustration of the step-up regulator performance. Regulation efficiency varies depending on battery status.

To power the H-bridge of the driver that requires 8-18V voltage input, we design a separate regulation board for voltage step-up. Particularly, high-frequency boost chopper technique is used. As shown in Figure 6.4, the high-frequency switching (1MHz) is enabled by TPS61040, which can be operated with constant peak current control to guarantee the actuation performance. The maximum load current output is tuned up to 2A by adjusting the peripheral capacitor and inductor. Typical efficiency of the prototyped regulator is greater than 70%, as shown in Figure 6.8. With fully charged battery (≈8.4V), the boost efficiency is above 85% and quite stable. However, it drops obviously when battery is low (≈6V). Based on Figure 6.8 the onboard batteries can support about $0.1/0.94 * 0.24 * 60 * 0.8 = 1.23$min flight, where 0.8 is the averaged power regulation efficiency.

6.3.4 Circuit Layout

For the control and driver board design, we use the common FR-4 substrates to construct a 4-layer stack up PCB. Each layer comes with 1 oz/ft^2 copper to accommodate the current requirements. Whole PCB size has been shrunk to match size, weight and power constraints while fitting the required chips and peripheral circuits and wiring. Similar design is applied to the splitting IMU module. The separate power regulation board is designed with only two layers to remove the unnecessary lamination and coppers, which uses 2 oz/ft^2 copper on both top and bottom layers. The details are shown in Figure 6.9.

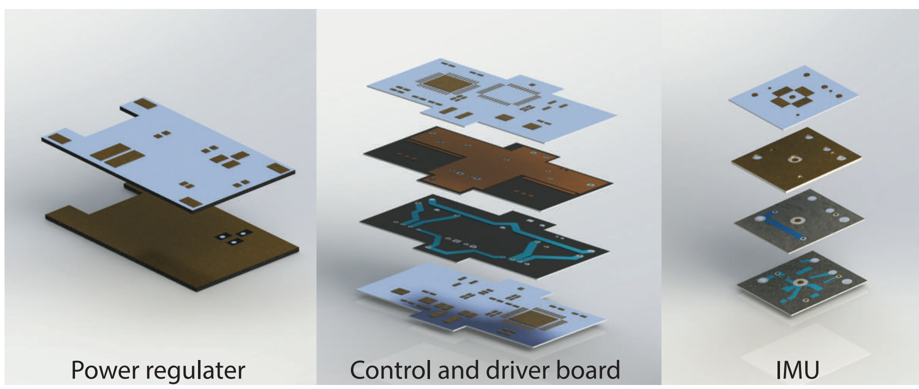

Figure 6.9. : Illustration of the layered design of onboard system.

Since PCB layout directly affects its performance, we use layered design to separate digital and analog nodes and paths to reduce the harmful effect from overlapping and cross-talk. To minimize parasitic inductance, all high current tracks are designed to connect to the specified analog ground in their shortest path, including motor driver output and current sensing paths. To avoid the impedance and noise of the signal on the ground path, we connect the digital and analog ground in a single point [106,107].

Note, in this scenario, magnetic beads or inductors are not working for digital-analog isolation since their high-frequency impedance can yield a large voltage spike between the digital and analog grounds that may damage the embedded chips consequently.

6.4 Experimental Result and Discussion

We conducted both indoor and outdoor untethered flight experiments of prototyped hummingbird robot. For the indoor test, a VICON motion capturing system with 6 cameras is used to record the vehicle attitude and position information. Attitude control reference was set to zero during the experiments. Since there is no onboard position sensing in the untethered flight, only attitude stability is under control yet vehicle position is drifting. From the result in Figure 6.10.(a) and (b), the attitude error of the test platform is within 10 degrees, demonstrating excellent flight stabilization.

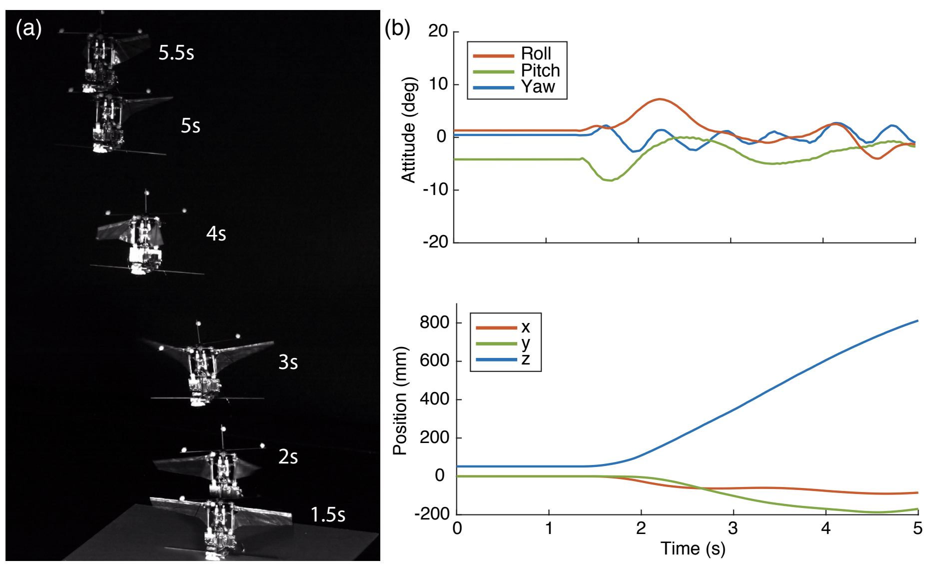

Figure 6.10. : (a) flight test without power and communication tether in VICON space for attitude and position recording, demonstrating the performance of onboard sensor fusion and control. (b) control result corresponds to (a).

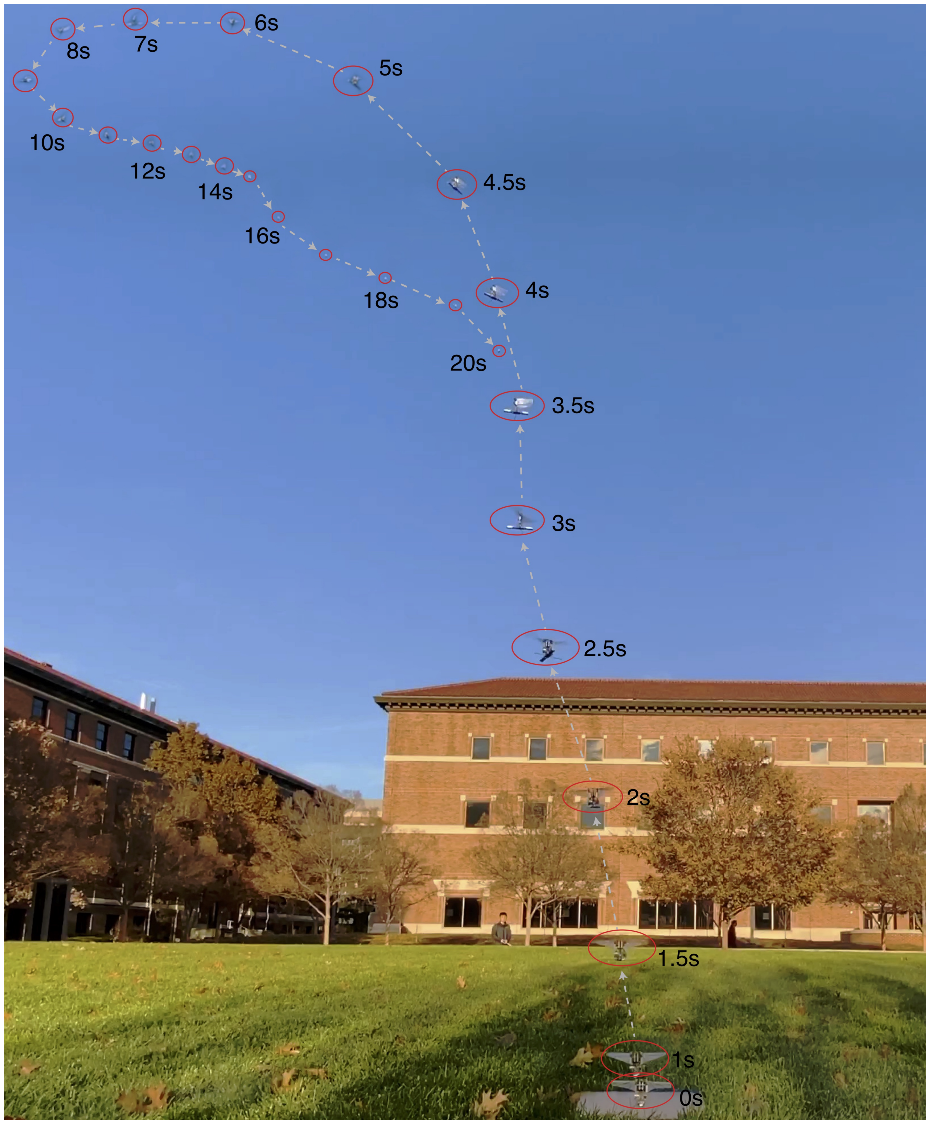

Figure 6.11. : Compound result of a typical outdoor untethered stable hovering under 15mph averaged wind gust.

A typical outdoor flight test is shown in Figure 6.11. Unlike indoor tests, outdoor experiments encounter more disturbances such as wind gust. Being a lightweight platform without onboard position feedback, such unpredicted external disturbances usually cause significant positional drift and hard to perform altitude control effectively, as exemplified in Figure 6.11. Since the depth of field of the image changes, it is difficult to certainly define constant scale information. For reference, the buildings around the experimental site are about 11-15m high. For safety concerns, we limited the allowable flight time ($\leq$20s) before the vehicle fly too high and drift far away. The test result demonstrates that the platform can also achieve sustained stable flight in outdoor environment. After adding position sensors in the future, wind gust caused position drift can be compensated through active position closed-loop control.

6.5 Conclusion

In this chapter, we present the untethered flight of an at-scale hummingbird robot whose sustained stable hovering was achieved by two actuators through their respective onboard motor drivers to alter the instantaneous wing trajectories, which are controlled by an STM32 microcontroller for desired aerodynamic thrust and flight control torques. Body attitude of the platform is sensed by onboard inertial sensors. A dc-dc power regulation module is attached to separate the power of logic devices and motor drivers. System power comes from two rechargeable onboard batteries. The proposed design is optimized to balance payload capacity and power efficiency. To the best of our knowledge, the result presents the first bio-inspired FWMAV equipped with only two actuators and capable of sustained stable flight in both indoor and outdoor environment. It is also the first untethered flight of FWMAV with independently controlled wings, a key inspiration from its natural counterparts. In the future, we will integrate additional navigation sensors such as cameras for flight navigation and control.

7. CONCLUSION AND FUTURE WORK

In this thesis, we proposed multidisciplinary research to address several common issues on flapping wing micro aerial vehicles, attempting to match the performance gap between engineered flying vehicles and their natural counterparts. The significance of the results presented in this thesis are: 1). For the flapping-wing robots, which are usually flying under large instantaneous oscillation, we proposed a model-based sensor fusion algorithm is for real-time onboard attitude feedback. Accurate and robust feedback is a significant prerequisite of control algorithm design. 2). With control authority analysis, we show that a DRC+PID control scheme can guarantee the stable flight of our hummingbird robot. Stationary hovering and rapid, accurate waypoint tracking flight were conducted to demonstrate the control performance. 3). In order to perform animal-like agile maneuvering, using model-free reinforcement learning to train a motion planner is a feasible way. We show that the proposed hummingbird robot is capable of performing the nearly drift-free flip maneuver with a learned maneuver policy. Such performance matches that of nature flyers. 4). To address the navigation issue in confined space, we propose the first flapping-wing robot by using its flapping wings in such dual functions - sensing and actuation coupled in one element for surrounding perception. It is significantly useful for those similar platforms under tight design constraints. 5). We address the payload challenge and system design with onboard power for the proposed hummingbird robot to achieve untethered stable flight, which is the world's first bio-inspired FWMAV powered by only two actuators and capable of sustained hovering in both indoor and outdoor environment. It is also the first untethered flight of an at-scale tailless hummingbird robot with independently controlled wings, a key inspiration from its natural counterparts.

Despite our pioneering work on the flapping-wing robots, numerous issues have to be addressed before such robots can fly like real hummingbird. Here We outlined several important directions to pursuit for future research as below:

Precisely fabricated wings are important for small-scale flapping wing robot. Refer to Harvard Robobee, their state-of-art high precision micro-machining facilities guarantee their insect-sized flapping wing vehicle's flight performance. Since we use manually fabricated wings, the amount of control effort puts on countering the minor differences of a pair of wings. From our simulated result, perfect aligned body and symmetrical wings will push the boundary of the flight envelope significantly, improving the flight performance.

Flight control and tracking performance can be further improved as well. Currently, the control performance is partially limited by onboard computational resources. We sacrifice some transient tracking performance to reduce the computing load. Advanced control algorithm design incorporated with a powerful onboard processor can certainly boost control performance. For learning-based control, besides the existing setup, a real 'end-to-end' training can be performed: directly generates motor voltage for robot control according to the state observation instead of following a certain sinusoidal wing trajectory. Such a design may generate unique control and motion plan solutions to address some certain scenarios effectively.

The demands on long-term autonomous flight necessitate the robot to provide more payload. The current 12 grams robot prototype was able to carry up to 16 grams payload. Unfortunately, it is unlikely to be sufficient for the extra components required to achieve long-term autonomous flight, such as more batteries and additional sensors. In fact, robot flying under full payload onboard will shorten the flight time and impact the control performance severely. We conduct preliminary calculations that show a bit larger scale vehicle design can generate reasonable payload capacity while needs further system-level optimization. Meanwhile, beyond current design optimization, multi-objective optimization using Genetic Algorithm can be a promising approach to address more trade-offs in robot design.

Autonomous navigation in a complex environment of such small aerial vehicles remains an open question due to computational and payload limitations. Wing load sensing can partially solve the navigation issue in confined, cluttered space. However, in a vast space, such as outdoors, it becomes infeasible. For autonomous navigation flight in a broad environment, the first step is localizing the vehicle without using VICON system. A possible solution is based on RSSI, which stands for Received Signal Strength Indicator, represents a value of the power of a received radio signal. The longer the distance is, the lower the RSSI signal is. Therefore, with an onboard wireless communication module (e.g., Bluetooth, Wifi), collaborating with a couple of wireless communication beacons, the vehicle can be localized with respect to those additional ground station devices. However, the working range will be limited by the available communication distance. Another possible solution is to add visual or other optic sensors for Simultaneous Localization and Mapping (SLAM). Yet, it is currently not feasible for such small systems due to the lack of such miniaturized sensors and the limited payload capacity of the robot. To address this issue, the specific sensing strategy research and robot design optimization is needed urgently.

REFERENCES

REFERENCES

[1] Stephen Dalton and John Kings. *Borne on the wind: the extraordinary world of insects in flight*. Number QL 496.7. D34. 1975.

[2] Michael H Dickinson. Directional sensitivity and mechanical coupling dynamics of campaniform sensilla during chordwise deformations of the fly wing. *Journal of experimental biology*, 169(1):221–233, 1992.

[3] Richard E Brown and M Roger Fedde. Airflow sensors in the avian wing. *Journal of experimental biology*, 179(1):13–30, 1993.

[4] Bo Cheng, Xinyan Deng, and Tyson L Hedrick. The mechanics and control of pitching manoeuvres in a freely flying hawkmoth (manduca sexta). *Journal of Experimental Biology*, 214(24):4092–4106, 2011.

[5] Bo Cheng, Bret W Tobalske, Donald R Powers, Tyson L Hedrick, Yi Wang, Susan M Wethington, George T-C Chiu, and Xinyan Deng. Flight mechanics and control of escape manoeuvres in hummingbirds ii. aerodynamic force production, flight control and performance limitations. *Journal of Experimental Biology*, pages jeb–137570, 2016.

[6] CP Ellington. The aerodynamics of insect flight. ii. morphological parameters. *Phil. Trans. R. Soc. Lond. B*, 305:17–40, 1984.

[7] Michael H Dickinson, Fritz-Olaf Lehmann, and Sanjay P Sane. Wing rotation and the aerodynamic basis of insect flight. *Science*, 284(5422):1954–1960, 1999.

[8] Mao Sun and Jian Tang. Unsteady aerodynamic force generation by a model fruit fly wing in flapping motion. *Journal of experimental biology*, 205(1):55–70, 2002.

[9] Sanjay P Sane. The aerodynamics of insect flight. *The journal of experimental biology*, 206(23):4191–4208, 2003.

[10] Wei Shyy, Yongsheng Lian, Jian Tang, Dragos Viieru, and Hao Liu. *Aerodynamics of low Reynolds number flyers*, volume 22. Cambridge University Press, 2007.

[11] John P Whitney and Robert J Wood. Aeromechanics of passive rotation in flapping flight. *Journal of fluid mechanics*, 660:197–220, 2010.

[12] JWS Pringle. The excitation and contraction of the flight muscles of insects. *The Journal of physiology*, 108(2):226–232, 1949.

[13] Susanne Sterbing-D'Angelo, Mohit Chadha, Chen Chiu, Ben Falk, Wei Xian, Janna Barcelo, John M Zook, and Cynthia F Moss. Bat wing sensors support flight control. *Proceedings of the National Academy of Sciences*, 108(27):11291–11296, 2011.

[14] Douglas L Altshuler, Joseph W Bahlman, Roslyn Dakin, Andrea H Gaede, Benjamin Goller, David Lentink, Paolo S Segre, and Dimitri A Skandalis. The biophysics of bird flight: functional relationships integrate aerodynamics, morphology, kinematics, muscles, and sensors. *Canadian Journal of Zoology*, 93(12):961–975, 2015.

[15] Jiang Hao Wu and Mao Sun. Unsteady aerodynamic forces of a flapping wing. *Journal of Experimental Biology*, 207(7):1137–1150, 2004.

[16] Wei Shyy, Hikaru Aono, Satish Kumar Chimakurthi, Pat Trizila, C-K Kang, Carlos ES Cesnik, and Hao Liu. Recent progress in flapping wing aerodynamics and aeroelasticity. *Progress in Aerospace Sciences*, 46(7):284–327, 2010.

[17] Xinyan Deng, Luca Schenato, Wei Chung Wu, and S Shankar Sastry. Flapping flight for biomimetic robotic insects: Part i-system modeling. *IEEE Transactions on Robotics*, 22(4):776–788, 2006.

[18] Xinyan Deng, Luca Schenato, and S Shankar Sastry. Flapping flight for biomimetic robotic insects: Part ii-flight control design. *IEEE Transactions on Robotics*, 22(4):789–803, 2006.

[19] Robert J Wood. The first takeoff of a biologically inspired at-scale robotic insect. *IEEE transactions on robotics*, 24(2):341–347, 2008.

[20] GCHE De Croon, KME De Clercq, Remes Ruijsink, B Remes, and Christophe de Wagter. Design, aerodynamics, and vision-based control of the delfly. *International Journal of Micro Air Vehicles*, 1(2):71–97, 2009.

[21] QV Nguyen, WL Chan, and M Debiasi. Performance tests of a hovering flapping wing micro air vehicle with double wing clap-and-fling mechanism. In *IMAV 2015: Proc. Int. Micro Air Vehicle Conf., Aachen, Germany, 15–18 September*, 2015.

[22] Jesse A Roll, Bo Cheng, and Xinyan Deng. An electromagnetic actuator for high-frequency flapping-wing microair vehicles. *IEEE Transactions on Robotics*, 31(2):400–414, 2015.

[23] Yang Zou, Weiping Zhang, and Zheng Zhang. Liftoff of an electromagnetically driven insect-inspired flapping-wing robot. *IEEE Transactions on Robotics*, 32(5):1285–1289, 2016.

[24] Jesse A Roll, Dane T Bardroff, and Xinyan Deng. Mechanics of a scalable high frequency flapping wing robotic platform capable of lift-off. In *Robotics and Automation (ICRA), 2016 IEEE International Conference on*, pages 4664–4671. IEEE, 2016.

[25] Takashi Ozaki and Kanae Hamaguchi. Bioinspired flapping-wing robot with direct-driven piezoelectric actuation and its takeoff demonstration. *IEEE Robotics and Automation Letters*, 3(4):4217–4224, 2018.

[26] Matthew Keennon, Karl Klingebiel, Henry Won, and Alexander Andriukov. Development of the nano hummingbird: A tailless flapping wing micro air vehicle. In *AIAA Aerospace Sciences Meeting*, 2012.

[27] Domenico Campolo, Muhammad Azhar, Gih-Keong Lau, and Metin Sitti. Can dc motors directly drive flapping wings at high frequency and large wing strokes? *IEEE/ASME Transactions on Mechatronics*, 19(1):109–120, 2012.

[28] Lindsey Hines, Domenico Campolo, and Metin Sitti. Liftoff of a motor-driven, flapping-wing microaerial vehicle capable of resonance. *IEEE Transactions on Robotics*, 30(1):220–232, 2013.

[29] Lindsey Hines, David Colmenares, and Metin Sitti. Platform design and tethered flight of a motor-driven flapping-wing system. In *Robotics and Automation (ICRA), 2015 IEEE International Conference on*, pages 5838–5845. IEEE, 2015.

[30] David Coleman, Moble Benedict, Vikram Hirishikeshaven, and Inderjit Chopra. Development of a robotic hummingbird capable of controlled hover. *Journal of the American Helicopter Society*, 62(3):1–9, 2017.

[31] A Roshanbin, H Altartouri, M Karásek, and André Preumont. Colibri: A hovering flapping twin-wing robot. *International Journal of Micro Air Vehicles*, 9(4):270–282, 2017.

[32] Hoang Vu Phan, Taesam Kang, and Hoon Cheol Park. Design and stable flight of a 21 g insect-like tailless flapping wing micro air vehicle with angular rates feedback control. *Bioinspiration & biomimetics*, 12(3):036006, 2017.

[33] Jian Zhang, Zhan Tu, Fan Fei, and Xinyan Deng. Geometric flight control of a hovering robotic hummingbird. In *Robotics and Automation (ICRA), 2017 IEEE International Conference on*, pages 5415–5421. IEEE, 2017.

[34] GCHE De Croon, M Perçin, BDW Remes, R Ruijsink, and C De Wagter. *The DelFly*. Springer, 2016.

[35] Matěj Karásek, Florian T Muijres, Christophe De Wagter, Bart DW Remes, and Guido CHE de Croon. A tailless aerial robotic flapper reveals that flies use torque coupling in rapid banked turns. *Science*, 361(6407):1089–1094, 2018.

[36] Jian Zhang, Fan Fei, Zhan Tu, and Xinyan Deng. Design optimization and system integration of robotic hummingbird. In *Robotics and Automation (ICRA), 2017 IEEE International Conference on*, pages 5422–5428. IEEE, 2017.

[37] Johannes James, Vikram Iyer, Yogesh Chukewad, Shyamnath Gollakota, and Sawyer B Fuller. Liftoff of a 190 mg laser-powered aerial vehicle: The lightest wireless robot to fly. In *2018 IEEE International Conference on Robotics and Automation (ICRA)*, pages 1–8. IEEE, 2018.

[38] Noah T Jafferis, E Farrell Helbling, Michael Karpelson, and Robert J Wood. Untethered flight of an insect-sized flapping-wing microscale aerial vehicle. *Nature*, 570(7762):491, 2019.

[39] L. Hines, D. Campolo, and M. Sitti. Liftoff of a motor-driven, flapping-wing microaerial vehicle capable of resonance. *IEEE Transactions on Robotics*, 30(1):220–232, Feb 2014.

[40] Christophe De Wagter, Sjoerd Tijmons, Bart DW Remes, and Guido CHE de Croon. Autonomous flight of a 20-gram flapping wing mav with a 4-gram onboard stereo vision system. In *2014 IEEE International Conference on Robotics and Automation (ICRA)*, pages 4982–4987. IEEE, 2014.

[41] Pakpong Chirarattananon, Kevin Y Ma, and Robert J Wood. Adaptive control for takeoff, hovering, and landing of a robotic fly. In *Intelligent Robots and Systems (IROS), 2013 IEEE/RSJ International Conference on*, pages 3808–3815. IEEE, 2013.

[42] Kevin Y Ma, Pakpong Chirarattananon, Sawyer B Fuller, and Robert J Wood. Controlled flight of a biologically inspired, insect-scale robot. *Science*, 340(6132):603–607, 2013.

[43] Fan Fei, Zhan Tu, Jian Zhang, and Xinyan Deng. Learning extreme hummingbird maneuvers on flapping wing robots. In *2019 IEEE International Conference on Robotics and Automation (ICRA)*, pages 109–115. IEEE, 2019.

[44] Zhan Tu, Fan Fei, Jian Zhang, and Xinyan Deng. Acting is seeing: Navigating tight space using flapping wings. In *2019 IEEE International Conference on Robotics and Automation (ICRA)*, pages 95–101. IEEE, 2019.

[45] Stanley S Baek, Kevin Y Ma, and Ronald S Fearing. Efficient resonant drive of flapping-wing robots. In *Intelligent Robots and Systems, 2009. IROS 2009. IEEE/RSJ International Conference on*, pages 2854–2860. IEEE, 2009.

[46] Lindsey Hines. *Design and Control of a Flapping Flight Micro Aerial Vehicle*. PhD thesis, Carnegie Mellon University, Pittsburgh, PA, August 2014.

[47] Pakpong Chirarattananon, Kevin Y Ma, and Robert J Wood. Perching with a robotic insect using adaptive tracking control and iterative learning control. *The International Journal of Robotics Research*, 35(10):1185–1206, 2016.

[48] Michael Karpelson, John P Whitney, Gu-Yeon Wei, and Robert J Wood. Design and fabrication of ultralight high-voltage power circuits for flapping-wing robotic insects. In *Applied Power Electronics Conference and Exposition (APEC), 2011 Twenty-Sixth Annual IEEE*, pages 2070–2077. IEEE, 2011.

[49] JL Verboom, Sjoerd Tijmons, C De Wagter, B Remes, Robert Babuska, and Guido CHE de Croon. Attitude and altitude estimation and control on board a flapping wing micro air vehicle. In *Robotics and Automation (ICRA), 2015 IEEE International Conference on*, pages 5846–5851. IEEE, 2015.

[50] Zhan Tu, Fan Fei, Yilun Yang, Jian Zhang, and Xinyan Deng. Realtime on-board attitude estimation of high-frequency flapping wing mavs under large instantaneous oscillation. In *2018 IEEE International Conference on Robotics and Automation (ICRA)*, pages 6806–6811. IEEE, 2018.

[51] Mark Euston, Paul Coote, Robert Mahony, Jonghyuk Kim, and Tarek Hamel. A complementary filter for attitude estimation of a fixed-wing uav. In *Intelligent Robots and Systems, 2008. IROS 2008. IEEE/RSJ International Conference on*, pages 340–345. IEEE, 2008.

[52] Sebastian OH Madgwick, Andrew JL Harrison, and Ravi Vaidyanathan. Estimation of imu and marg orientation using a gradient descent algorithm. In *Rehabilitation Robotics (ICORR), 2011 IEEE International Conference on*, pages 1–7. IEEE, 2011.

[53] Shaojie Shen, Yash Mulgaonkar, Nathan Michael, and Vijay Kumar. Multi-sensor fusion for robust autonomous flight in indoor and outdoor environments with a rotorcraft mav. In *Robotics and Automation (ICRA), 2014 IEEE International Conference on*, pages 4974–4981. IEEE, 2014.

[54] Tyson L Hedrick, Bo Cheng, and Xinyan Deng. Wingbeat time and the scaling of passive rotational damping in flapping flight. *Science*, 324(5924):252–255, 2009.

[55] Bo Cheng and Xinyan Deng. Translational and rotational damping of flapping flight and its dynamics and stability at hovering. *Robotics, IEEE Transactions on*, 27(5):849–864, 2011.

[56] Sawyer B Fuller, E Farrell Helbling, Pakpong Chirarattananon, and Robert J Wood. Using a mems gyroscope to stabilize the attitude of a fly-sized hovering robot. In *IMAV 2014: International Micro Air Vehicle Conference and Competition 2014, Delft, The Netherlands, August 12-15, 2014*. Delft University of Technology, 2014.

[57] Naser El-Sheimy, Haiying Hou, and Xiaoji Niu. Analysis and modeling of inertial sensors using allan variance. *IEEE Transactions on instrumentation and measurement*, 57(1):140–149, 2008.

[58] E Farrell Helbling, Sawyer B Fuller, and Robert J Wood. Pitch and yaw control of a robotic insect using an onboard magnetometer. In *Robotics and Automation (ICRA), 2014 IEEE International Conference on*, pages 5516–5522. IEEE, 2014.

[59] Tsung-Lin Chen. Design and analysis of a fault-tolerant coplanar gyro-free inertial measurement unit. *Journal of Microelectromechanical Systems*, 17(1):201–212, 2008.

[60] Markus W Achtelik, Michael Achtelik, Stephan Weiss, and Roland Siegwart. Onboard imu and monocular vision based control for mavs in unknown in- and outdoor environments. In *IEEE International Conference on Robotics and Automation (ICRA 2011)*. Eidgenössische Technische Hochschule Zürich, Autonomous Systems Lab, 2011.

[61] Matthias Faessler, Flavio Fontana, Christian Forster, and Davide Scaramuzza. Automatic re-initialization and failure recovery for aggressive flight with a monocular vision-based quadrotor. In *Robotics and Automation (ICRA), 2015 IEEE International Conference on*, pages 1722–1729. IEEE, 2015.

[62] Mahanth Gowda, Justin Manweiler, Ashutosh Dhekne, Romit Roy Choudhury, and Justin D Weisz. Tracking drone orientation with multiple gps receivers. In *Proceedings of the 22nd Annual International Conference on Mobile Computing and Networking*, pages 280–293. ACM, 2016.

[63] SF Armanini, M Karásek, GCHE De Croon, and CC De Visser. Onboard/offboard sensor fusion for high-fidelity flapping-wing robot flight data. *Journal of Guidance, Control, and Dynamics*, 40(8):2121–2132, 2017.

[64] Zhan Tu, Fan Fei, Matthew Eagon, Dongyan Xu, and Xinyan Deng. Flight recovery of mavs with compromised imu. In *Intelligent Robots and Systems (IROS), 2019 IEEE/RSJ International Conference on*. IEEE, 2019.

[65] Rabbath Camille Alain and Lechevin Nicolas. *Safety and reliability in cooperating unmanned aerial systems*. World Scientific, 2010.

[66] Hongjun Choi, Wen-Chuan Lee, Yousra Aafer, Fan Fei, Zhan Tu, Xiangyu Zhang, Dongyan Xu, and Xinyan Xinyan. Detecting attacks against robotic vehicles: A control invariant approach. In *Proceedings of the 2018 ACM SIGSAC Conference on Computer and Communications Security*, pages 801–816. ACM, 2018.

[67] Soon-Jo Chung and Michael Dorothy. Neurobiologically inspired control of engineered flapping flight. *Journal of guidance, control, and dynamics*, 33(2):440–453, 2010.

[68] Andrea Serrani. Robust nonlinear control design for a minimally-actuated flapping-wing mav in the longitudinal plane. In *Decision and Control and European Control Conference (CDC-ECC), 2011 50th IEEE Conference on*, pages 7464–7469. IEEE, 2011.

[69] Christopher T Orlowski and Anouck R Girard. Dynamics, stability, and control analyses of flapping wing micro-air vehicles. *Progress in Aerospace Sciences*, 51:18–30, 2012.

[70] Haithem E Taha, Muhammad R Hajj, and Ali H Nayfeh. Flight dynamics and control of flapping-wing mavs: a review. *Nonlinear Dynamics*, 70(2):907–939, 2012.

[71] Wei Shyy, Chang-kwon Kang, Pakpong Chirarattananon, Sridhar Ravi, and Hao Liu. Aerodynamics, sensing and control of insect-scale flapping-wing flight. *Proc. R. Soc. A*, 472(2186):20150712, 2016.

[72] Luca Schenato. *Analysis and Control of Flapping Flight: from Biological to Robotic Insects*. PhD thesis, University of California, 2003.

[73] Christopher T Orlowski and Anouck R Girard. Stability derivatives for a flapping wing mav in a hover condition using local averaging. In *American Control Conference (ACC), 2011*, pages 1604–1609. IEEE, 2011.

[74] Pakpong Chirarattananon, Kevin Y Ma, and Robert J Wood. Adaptive control of a millimeter-scale flapping-wing robot. *Bioinspiration & biomimetics*, 9(2):025004, 2014.

[75] Sergei Lupashin and Raffaello D'Andrea. Adaptive fast open-loop maneuvers for quadrocopters. *Autonomous Robots*, 33(1-2):89–102, 2012.

[76] Alecia Youngblood Jackson. An ontology of a backflip. *Cultural Studies? Critical Methodologies*, 16(2):183–192, 2016.

[77] Sawyer B Fuller, Michael Karpelson, Andrea Censi, Kevin Y Ma, and Robert J Wood. Controlling free flight of a robotic fly using an onboard vision sensor inspired by insect ocelli. *Journal of The Royal Society Interface*, 11(97):20140281, 2014.

[78] Kirk YW Scheper, Matěj Karásek, Christophe De Wagter, Bart DW Remes, and Guido CHE De Croon. First autonomous multi-room exploration with an insect-inspired flapping wing vehicle. In *2018 IEEE International Conference on Robotics and Automation (ICRA)*, pages 1–7. IEEE, 2018.

[79] William A Lewinger, Cynthia M Harley, Roy E Ritzmann, Michael S Branicky, and Roger D Quinn. Insect-like antennal sensing for climbing and tunneling behavior in a biologically-inspired mobile robot. In *Robotics and Automation, 2005. ICRA 2005. Proceedings of the 2005 IEEE International Conference on*, pages 4176–4181. IEEE, 2005.

[80] Jusuk Lee, Simon N Sponberg, Owen Y Loh, Andrew G Lamperski, Robert J Full, and Noah J Cowan. Templates and anchors for antenna-based wall following in cockroaches and robots. *IEEE Transactions on Robotics*, 24(1):130–143, 2008.

[81] Patrick Thevoz and Adrien Briod. Flyability wins the uae drones for good award [humanitarian technology]. *IEEE Robotics & Automation Magazine*, 22(2):108–110, 2015.

[82] Pooya Sareh, Pisak Chermprayong, Marc Emmanuelli, Haris Nadeem, and Mirko Kovac. Rotorigami: A rotary origami protective system for robotic rotorcraft. *Science Robotics*, 3(22):eaah5228, 2018.

[83] Crawford H Greenewalt. The wings of insects and birds as mechanical oscillators. *Proceedings of the American Philosophical Society*, pages 605–611, 1960.

[84] Attila J Bergou, Sheng Xu, and Z Jane Wang. Passive wing pitch reversal in insect flight. *Journal of Fluid Mechanics*, 591:321–337, 2007.

[85] David B Doman, Michael W Oppenheimer, and David O Sigthorsson. Wingbeat shape modulation for flapping-wing micro-air-vehicle control during hover. *Journal of guidance, control, and dynamics*, 33(3):724–739, 2010.

[86] David B Doman, Michael W Oppenheimer, and David O Sigthorsson. Dynamics and control of a biomimetic vehicle using biased wingbeat forcing functions: Part ii: Controller. *48th AIAA Aerospace Sciences Meeting Including the New Horizons Forum and Aerospace Exposition*, 1024, 2010.

[87] Alberto Cavallo, Andrea Cirillo, Pasquale Cirillo, Giuseppe De Maria, Pietro Falco, Ciro Natale, and Salvatore Pirozzi. Experimental comparison of sensor fusion algorithms for attitude estimation. *IFAC Proceedings Volumes*, 47(3):7585–7591, 2014.

[88] Giuseppe Loianno, Chris Brunner, Gary McGrath, and Vijay Kumar. Estimation, control, and planning for aggressive flight with a small quadrotor with a single camera and imu. *IEEE Robotics and Automation Letters*, 2(2):404–411, 2017.

[89] Jianwei Zheng, Minhui Qi, Kui Xiang, and Muye Pang. Imu performance analysis for a pedestrian tracker. In *International Conference on Intelligent Robotics and Applications*, pages 494–504. Springer, 2017.

[90] Ali H Nayfeh and Dean T Mook. *Nonlinear oscillations.* John Wiley & Sons, 2008.

[91] Bo Cheng, Jesse A Roll, and Xinyan Deng. Modeling and optimization of an electromagnetic actuator for flapping wing micro air vehicle. In *Robotics and Automation (ICRA), 2013 IEEE International Conference on*, pages 4035–4041. IEEE, 2013.

[92] Jian Zhang, Bo Cheng, and Xinyan Deng. Instantaneous wing kinematics tracking and force control of a high-frequency flapping wing insect mav. *Journal of Micro-Bio Robotics*, 11(1-4):67–84, 2016.

[93] Glenn Creamer. Spacecraft attitude determination using gyros and quaternion measurements. *Journal of the Astronautical Sciences*, 44(3):357–371, 1996.

[94] Malcolm David Shuster and S D_ Oh. Three-axis attitude determination from vector observations. *Journal of Guidance, Control, and Dynamics*, 2012.

[95] Shankar Sastry and Marc Bodson. *Adaptive control: stability, convergence and robustness*. Courier Corporation, 2011.

[96] Gildas Besançon. Remarks on nonlinear adaptive observer design. *Systems & control letters*, 41(4):271–280, 2000.

[97] Fan Fei, Zhan Tu, Yilun Yang, Jian Zhang, and Xinyan Deng. Flappy hummingbird: An open source dynamic simulation of flapping wing robots and animals. In *2019 IEEE International Conference on Robotics and Automation (ICRA)*, pages 9223–9229. IEEE, 2019.

[98] Timothy P Lillicrap, Jonathan J Hunt, Alexander Pritzel, Nicolas Heess, Tom Erez, Yuval Tassa, David Silver, and Daan Wierstra. Continuous control with deep reinforcement learning. *arXiv preprint arXiv:1509.02971*, 2015.

[99] Yan Duan, Xi Chen, Rein Houthooft, John Schulman, and Pieter Abbeel. Benchmarking deep reinforcement learning for continuous control. In *International Conference on Machine Learning*, pages 1329–1338, 2016.

[100] Xue Bin Peng, Marcin Andrychowicz, Wojciech Zaremba, and Pieter Abbeel. Sim-to-real transfer of robotic control with dynamics randomization. In *2018 IEEE International Conference on Robotics and Automation (ICRA)*, pages 1–8. IEEE, 2018.

[101] Erica J Kim, Marta Wolf, Victor Manuel Ortega-Jimenez, Stanley H Cheng, and Robert Dudley. Hovering performance of anna's hummingbirds (calypte anna) in ground effect. *Journal of The Royal Society Interface*, 11(98):20140505, 2014.

[102] H Lu, KB Lua, YJ Lee, TT Lim, and KS Yeo. Ground effect on the aerodynamics of three-dimensional hovering wings. *Bioinspiration & biomimetics*, 11(6):066003, 2016.

[103] Vladimir J Lumelsky and Tim Skewis. Incorporating range sensing in the robot navigation function. *IEEE Transactions on Systems, Man, and Cybernetics*, 20(5):1058–1069, 1990.

[104] James Ng and Thomas Bräunl. Performance comparison of bug navigation algorithms. *Journal of Intelligent and Robotic Systems*, 50(1):73–84, 2007.

[105] Sawyer B Fuller. Four wings: an insect-sized aerial robot with steering ability and payload capacity for autonomy. *IEEE Robotics and Automation Letters*, 4(2):570–577, 2019.

[106] W Marshall Leach. Fundamentals of low-noise analog circuit design. *Proceedings of the IEEE*, 82(10):1515–1538, 1994.

[107] Sanjay Pithadia and Shridhar More. Grounding in mixed-signal systems demystified, part 2. *Analog Applications*, 2013.